This is to certify that the
dissertation entitled

DESIGN OF MATERIALS WITH SPECIAL DYNAMIC
PROPERTIES USING NEGATIVE STIFFNESS
COMPONENTS

presented by

Jitendra Prasad

has been accepted towards fulfillment
of the requirements for the

Ph.D. degree in Mechanical Engineering

Major Professor's Signature

14 MAY, 2007

Date

DESIGN OF MATERIALS WITH SPECIAL DYNAMIC PROPERTIES USING NEGATIVE STIFFNESS COMPONENTS

By

Jitendra Prasad

A DISSERTATION

Submitted to
Michigan State University
in partial fulfillment of the requirements
for the degree of

DOCTOR OF PHILOSOPHY

Department of Mechanical Engineering

2007

ABSTRACT

DESIGN OF MATERIALS WITH SPECIAL DYNAMIC PROPERTIES USING NEGATIVE STIFFNESS COMPONENTS

By

Jitendra Prasad

This work presents design concepts to synthesize composite materials with special dynamic properties, namely, materials that soften at high frequencies. A typical rubber-like material hardens with frequency and a material which reverses this behavior will find application in product design for vibration absorption such as automobile engine mounts. Such dynamic properties are achieved through the use of a two-phase material that has inclusions of a viscoelastic material of negative elastic modulus in a typical matrix phase that has a positive elastic modulus. Possible realizations of the negative stiffness inclusion phase are presented. One way to realize the negative stiffness phase is by using a lattice containing bistable structures. A numerical homogenization technique is used to compute the average viscoelastic properties of such composites. A methodology is presented for the automatic design of such special materials using topology optimization techniques. The method and the vibration-isolation properties of a composite material designed with it are demonstrated through examples.

Neither the thief can steal it, nor can the king take it
Neither divided amongst brothers, nor too heavy to carry
The more you expend it, the more it increases
Knowledge is the prime wealth

- Subhashitani (The wise sayings in Sanskrit)

Dedicated to all the teachers in my life

ACKNOWLEDGMENTS

My foremost appreciation and gratitude are due to my advisor Professor Alejandro Diaz for his invaluable guidance, teaching, help and support throughout my doctoral studies. I will be ever grateful to him for the academic confidence and self-reliance that he inculcated in me through his seamless belief in my abilities and his encouragement to me to perform better than others.

Deepest appreciation and thanks are also extended to the other members of my PhD guidance committee – Professor Chang-Yi Wang, Professor Alan Haddow and Professor Brian Feeny – for the time off their busy schedule to examine this work and provide their invaluable suggestions. Special thanks to Professor Haddow for the discussions and brainstorming sessions during the initial phase of my research.

I thank the department staff and the fellow students who have extended their helping hands in coping with my day-to-day life as a graduate student – especially to the graduate secretary Aida Montalvo for taking care of various paperworks, my advisor's professorial assistant Sara Murawa for helping me with the development of demos and one of my lab-mates Amir Zamiri for the interesting discussions on the material science.

This work was sponsored by Toyota Motor Company. I gratefully acknowledge this support.

TABLE OF CONTENTS

CHAPTER 5

LIST OF FIGURES

CHAPTER 1

INTRODUCTION

1.1 Motivation and Background

Special dynamic properties such as a softening of the dynamic modulus of a viscoelastic material at high frequencies are desirable for some applications. For example, a material that softens at high frequencies may be used to make an ideal automobile engine mount, as an ideal engine mount should maintain high stiffness at a low frequency and low stiffness at higher frequencies (Yu et al (2000)). Such material may be called a smart material, as smart materials typically respond to environmental stimuli (e.g., forcing frequency) with particular changes in some variables (e.g., dynamic modulus). This work explores concepts for the design of materials with these unusual dynamic properties, with applications in design of engine mounts and similar vibration-isolation components.

The function of an engine mount is to support the weight of the engine while isolating unbalanced engine disturbance forces from the vehicle structure. The force transmitted to the vehicle structure increases with the dynamic stiffness of the mount and therefore, the mount should have low dynamic stiffness in order to isolate the vibration caused by the engine. However, large static and quasi-static engine displacements resulting from low dynamic stiffness and shock excitation (e.g., low-frequency excitation forces caused by an uneven road or by sudden acceleration, deceleration or braking) may cause damage to the engine and vehicle structure. The dynamic stiffness of an ideal engine mount, therefore, should be a function of frequency of excitation. In other words, the dynamic modulus of a material ideal for an engine mount should decrease with the forcing frequency. However, a typical single-phase material does not soften at high frequencies. In fact, a composite mixture of such typical materials does not soften either. For example, a Voigt composite (i.e. a two-phase layered composite material in which laminae are aligned in the direction of the force) will soften if and only if the elastic modulus of at least one of the constituent phases decreases with frequency. This is because the effective elastic modulus of this composite is a convex combination of the elastic moduli of the individual phases. Similarly, a Reuss composite (i.e. a two-phase layered composite material in which laminae are aligned perpendicular to the direction of the force) cannot display frequency-induced softening unless at least one of the constituent phases too displays such softening. However, it is possible to achieve frequency-induced softening in a two-phase composite if one of the constituent phases has a negative elastic modulus. For example, in Wang and Lakes (2004a and 2004b) an inclusion of a 'negative-stiffness' phase in a matrix of a typical material is shown to lead to a softening of the dynamic stiffness at high forcing frequencies. This behavior is the basis for the concepts explored here. The objective of this work is to generate design concepts that will lead to the synthesis of two-phase composite materials that soften monotonically with forcing frequency. The goal is to expose novel concepts and algorithms that could be used as guidelines by material scientists in future work, rather than to provide a specific recipe to synthesize the material. The work of Wang and Lakes (2004a and 2004b) serves as an inspiration to use negative stiffness inclusions.

A negative stiffness material has a negative elastic modulus. Such materials are not stable and therefore, do not permanently exist in the negative stiffness state. A block of negative stiffness material, however, can be made stable by constraining it from all sides by surrounding the block with a typical (i.e. stable) material, as shown in Lakes and Drugan (2002). Negative stiffness materials are realizable. For example, Lakes and Drugan (2002) and Wang and Lakes (2004b, 2005b) proposed lumped lattices to implement negative stiffness inclusions. In such lumped lattices, negative stiffness is basically achieved by a bistable structure. A bistable structure has two stable configurations under no external loads and is known to have 'negative stiffness' in the neighborhood of third, unstable configuration.

The effect of a negative stiffness inclusion in a composite material may be studied analytically or numerically by approximating the composite as a lumped system. For example, Wang and Lakes (2004a, 2004b) studied a one-dimensional spring-damper system as an approximation of a two-phase composite material. In that work, numerical analysis of the lumped system revealed atypical properties of a composite material having a negative stiffness inclusion (the negative stiffness inclusion was demonstrated also to lead to extremely high stiffness and damping). Analysis of the equivalent 1D lumped model helps in choosing properties of matrix and inclusion phases that can lead to the desired softening. This approach will be used here too.

With a negative stiffness material at hand and the knowledge that the inclusions of a negative stiffness phase in a matrix of a typical material phase can lead to frequency-induced softening, it is possible to tailor a composite material to desirable properties. The so-called 'inverse homogenization problem' in which the effective properties of a composite material is prescribed and the goal is to find topology that gives the prescribed material properties, is well-known, for example in Sigmund (1995) and Diaz and Benard (2003). The material design methodology has also been extended to design a viscoelastic material, for example in Yi et al. (2000). In this work, the existing knowledge in the material design problem has been extended to design the composite materials that exhibit frequency-induced softening.

The application of the present work is not limited to the frequency-induced softening or the vibration isolation only; this work may be easily extended to design extremal materials, where an extremal material refers to one having an elastic / viscoelasic property equal to the maximum or minimum value allowed by the rigorous theoretical bounds such as Hashin-Shtrikman bound (originated from Hashin and Shtrikman (1963)), Cherkaev-Gibiansky bound (detailed in Cherkaev and Gibiansky (1993)) and the corresponding viscoelastic bounds (given in Gibiansky and Milton (1993), Milton and Berryman (1997) and Gibiansky et al. (1999)). The inverse homogenization problem has already been used to design elastic materials with unusual or etxremal properties such as the materials with zero or negative Poisson's ratio as in Sigmund (1995) and the materials having extremal bulk modulus as in Sigmund (2000). Unususal or extremal materials in the context of viscoelasticty have also been made. For example, using materials with negative bulk modulus, Jaglinski et al (2007) have built composite materials that have viscoelastic stiffness greater than diamond. The negative stiffness phase and the topology optimization method used in this work may be extended to design materials that can exhibit such extreme viscoelastic behaviors.

1.2 Organization of the Dissertation

The rest of the dissertation is organized as follows. A methodology to conceptually design the desired material is described in chapter 2. It introduces a model of a two-phase composite material and discusses a negative stiffness material, which is used to build the inclusion phase. The stability and realization of the inclusion phase are discussed in this chapter. Chapter 3 describes the homogenization method used here to compute the effective properties of the composite material. The application of the design methodology and the performance of the designed material are demonstrated through a few examples in that chapter. The automatic design of the softening materials using topology optimization is described in chapter 4 and examples are presented to evaluate the performance of the design method. Chapter 5 gives details on designing tileable bistable structures which may be used to realize the negative stiffness material. Conclusions are drawn at the end and references are given.

CHAPTER 2

TWO PHASE COMPOSITE MATERIAL

With the ultimate goal of achieving a composite material that exhibits frequency-induced softening, this chapter simplifies a two-dimensional composite material into a one dimensional mechanical model that is made of springs and dampers. The mechanical model is analyzed for a stable frequency-induced softening. It is found that one of the springs is required to have a negative stiffness in order to get frequency-induced softening. It is therefore important to allow the spring stiffness to assume a negative value. A structure having a negative stiffness component, however, may be unstable and therefore conditions for the stability of the mechanical model are derived to make sure the model has a stable frequency-induced softening. Once the parameters (i.e. spring stiffness and damper coefficients) of the 1D model leading to a stable frequency-induced softening are determined, these parameters are extended back to construct the corresponding two-dimensional composite model. The 1D system studies imply that a composite material softens with frequency if the composite has inclusion of a negative stiffness material B in a matrix of a typical elastic material A. The stability of the negative stiffness inclusion is reviewed as the stability criterion of the 1D model may not be sufficient in two-dimensions. Material A, being a typical elastic material with positive Young's modulus, is easily available. In contrast, material B has negative Young's modulus and is not available. A negative stiffness material that can be used as material B is, therefore, built. Material B is proposed as a lumped lattice that has negative-stiffness springs. The negative stiffness springs realizes the negative Young's Modulus. The negative stiffness is in turn realized by bistable structures.

2.1 Mechanical Models of Viscoelastic Composites

The strategy to design a material exhibiting frequency induced softening relies on the study of non-homogenous materials with a periodic micro-structure designed to reverse the behavior of typical materials, which stiffen with frequency. In particular, this work studies a two-phase composite material composed of periodic inclusions of a viscoelastic phase B in matrix of an elastic/viscoelastic phase A. A schematic arrangement of such composites is shown in Fig. 2.1. The dashed square in Fig. 2.1 shows a fundamental cell of the periodic arrangement. The properties of the constituent phases and their shape and topology are the variables to be determined in order to obtain the desired results.

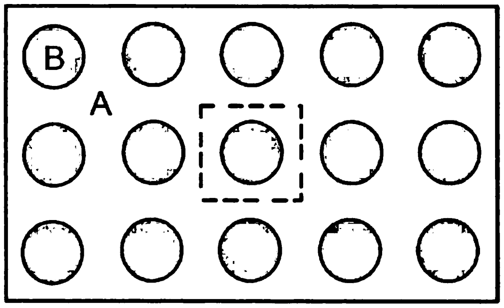

Figure 2.1. Two-phase composite material (dashed box shows the fundamental cell)

Following Fujino et al. (1964) and Marinov (1978), the two phase composite material can be approximated as two types of mechanical models combining the two phases as shown in Figures 2.2(b,c) and 2.2(d,e). The former mechanical model represents a simple additivity of contribution of partial stress of each element sliced vertically to the total stress, and the latter that of partial strain of each element sliced horizontally to the total strain. In these models, rigid adhesion between the two phases and no interference between the sliced elements are assumed, i.e., actual stress or strain distribution along the spherical surface of each phase is much simplified.

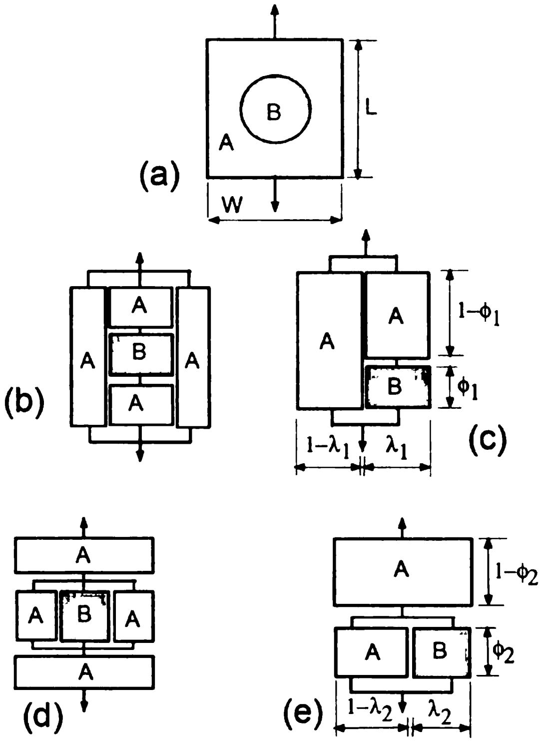

Figure 2.2. Two types of mechanical models corresponding to a simple mechanical mixture, B sphere in A unit cubic lattice – (a) Unit or fundamental cell, (b) & (c) equivalent parallel model, (d) & (e) equivalent series model

In the model in Fig. 2.2(c), λ_1 and ϕ_1 are the length fractions of phase B in horizontal and vertical directions, respectively. If both the two phases A and B are perfectly elastic materials, the average Young's modulus is obtained (as a function of the Young's moduli of the individual phases) by solving equations of equilibrium. This expression for the average Young's modulus can be extended to obtain the average *complex* modulus of the viscoelatic material by using the *correspondence principle*. In the present context, the correspondence principle states that the expression for the average complex modulus of a viscoelastic composite may be obtained by replacing the phase Young's moduli by phase complex moduli in that expression of the average Young's modulus.

Haddad (1995) presents a general definition of the correspondence principle as follows: For a large number of technical viscoelastic problems, it is possible to relate mathematically the solution of a linear, viscoelastic boundary value problem to an analogous problem of an elastic body of the same geometry and under the same initial and boundary conditions. This is carried out by transforming the governing equations of the viscoelastic problem to be mathematically equivalent to those governing a corresponding elastic problem. In this, both Laplace and Fourier transforms are often used. Accordingly, one would be able to employ the tools of the theory of elasticity to solve different boundary value problems in linear viscoelasticity. This analogy is referred to as the 'correspondence principle' and implies the elastic procedures may be utilized to derive transformed viscoelastic solutions.

Applying the correspondence principle, if E_A^* and E_B^* are complex moduli of phases A and B, respectively, then the average complex modulus of the two-phase material may be given by

$$E_{H1}^{*} = (1-\lambda_1)E_A^{*} + \lambda_1 \left[\frac{(1-\phi_1)}{E_A^{*}} + \frac{\phi_1}{E_B^{*}} \right]^{-1} \tag{2.1.1}$$

Similarly for the model in Fig. 2.2(e), λ_2 and ϕ_2 are the length fractions of phase B in horizontal and vertical directions, respectively. The average complex modulus based on the series model is given by

$$E_{H2}^{*} = \left[\frac{(1-\phi_2)}{E_A^{*}} + \frac{\phi_2}{(1-\lambda_2)E_A^{*} + \lambda_2 E_B^{*}} \right]^{-1} \tag{2.1.2}$$

Viscoelastic materials are often represented by mechanical models consisting of elastic springs and viscous dashpots, where the elastic springs describe for the elastic behavior and the dashpots describe viscous behavior. The mechanical model shown in Fig. 2.2(e) will be studied. In this example, Phase A is assumed perfectly elastic and, therefore, will be represented by an elastic spring. The inclusion phase B is modeled as a standard linear solid. A standard linear solid model of viscoelasticity is sketched in Fig. 2.3, where E_1, E_2 and η are the three parameters of the standard linear solid.

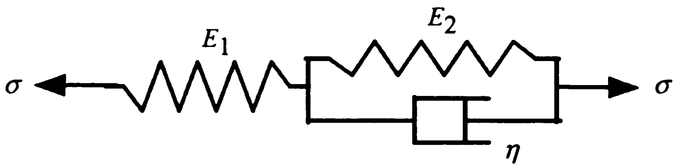

Figure 2.3. Standard linear solid model of viscoelasticity

The complex modulus corresponding to the viscoelastic model shown in Fig. 2.3 is given by

$$E_B^*(\omega) = \frac{E_1(E_2 + i\eta\omega)}{(E_1 + E_2 + i\eta\omega)} \tag{2.1.3}$$

The mechanical model corresponding to Fig. 2.2(e) is shown in Fig. 2.4. This mechanical model is same as that studied in Wang and Lakes (2004a, 2004b, 2005a).

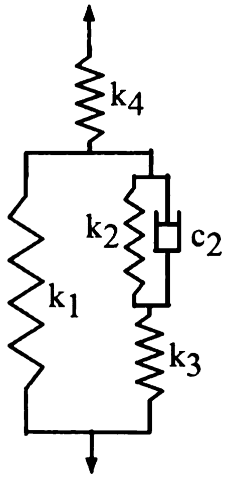

Figure 2.4. Spring-dashpot system corresponding to the series system in Fig. 2.2(e)

The parameters in Figs. 2.2(e) and 2.3 are related as follows:

$$E_A = \frac{k_1\phi_2}{(1-\lambda_2)d} = \frac{k_4(1-\phi_2)}{d} \tag{2.1.4}$$

and

$$E_B^* = \frac{E_1(E_2 + i\eta\omega)}{(E_1 + E_2 + i\eta\omega)} = \frac{k_3(k_2 + ic_2\omega)}{(k_3 + k_2 + ic_2\omega)}\frac{\phi_2}{\lambda_2 d} \tag{2.1.5}$$

since the viscoelastic material parameters are

$$E_1 = k_3 \frac{\phi_2}{\lambda_2 d} \qquad (2.1.6)$$

$$E_2 = k_2 \frac{\phi_2}{\lambda_2 d} \qquad (2.1.7)$$

$$\eta = c_2 \frac{\phi_2}{\lambda_2 d} \qquad (2.1.8)$$

where

$$d = \frac{WD}{L} \qquad (2.1.9)$$

W is the width of the fundamental cell (Fig. 2.2(a)).

H is the height of the fundamental cell (Fig. 2.2(a)).

D is the thickness of the fundamental cell.

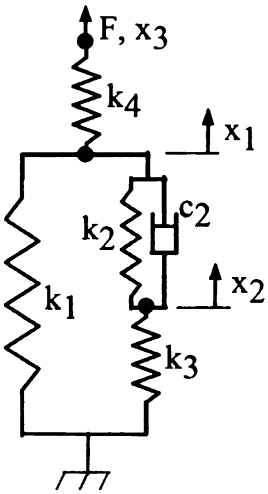

Figure 2.5. Spring-dashpot system with boundary conditions

The lower end of the system will be fixed as shown in Fig. 2.5 and a force will be applied at the upper end. The equation of motion of the system in Fig. 2.5 is given by

$$\begin{bmatrix} c_2 & -c_2 & 0 \\ -c_2 & c_2 & 0 \\ 0 & 0 & 0 \end{bmatrix}\begin{pmatrix} \dot{x}_1 \\ \dot{x}_2 \\ \dot{x}_3 \end{pmatrix}+\begin{bmatrix} k_1+k_2+k_4 & -k_2 & -k_4 \\ -k_2 & k_2+k_3 & 0 \\ -k_4 & 0 & k_4 \end{bmatrix}\begin{pmatrix} x_1 \\ x_2 \\ x_3 \end{pmatrix}=\begin{pmatrix} 0 \\ 0 \\ F \end{pmatrix} \tag{2.1.10}$$

The applied force F is periodic. F is given by

$$F = F_o e^{i\omega t} \tag{2.1.11}$$

The steady-state solution to the equations of motion is given by

$$\begin{pmatrix} x_1 \\ x_2 \\ x_3 \end{pmatrix}=\begin{pmatrix} x_{10} \\ x_{20} \\ x_{30} \end{pmatrix}e^{i\omega t} \tag{2.1.12}$$

Substituting (2.1.12) in the equation of motion (2.1.10), we get

$$\begin{bmatrix} k_1+k_2+k_4+i\omega c_2 & -k_2-i\omega c_2 & -k_4 \\ -k_2-i\omega c_2 & k_2+k_3+i\omega c_2 & 0 \\ -k_4 & 0 & k_4 \end{bmatrix}\begin{pmatrix} x_{10} \\ x_{20} \\ x_{30} \end{pmatrix}=\begin{pmatrix} 0 \\ 0 \\ F_o \end{pmatrix} \tag{2.1.13}$$

Solving the new equation of motion (2.1.13), we get

$$\frac{F_o}{x_{30}}=\frac{k_4[k_3(k_2+ic_2\omega)+k_1(k_2+k_3+ic_2\omega)]}{k_3(k_2+ic_2\omega)+(k_1+k_4)(k_2+k_3+ic_2\omega)} \tag{2.1.14}$$

Eliminating k_1, k_2 , k_3, k_4 and c_2 in (2.1.14) by using (2.1.3)-(2.1.6), we get

$$\frac{F_o}{x_{30}}=\left[\frac{(1-\phi_2)}{E_A^*}+\frac{\phi_2}{(1-\lambda_2)E_A^*+\lambda_2 E_B^*}\right]^{-1} d = E_{H2}^* d \tag{2.1.15}$$

where E_{H2}^* is the average complex modulus for the two-phase material (equation 2.1.2). The quantity E_{H2}^*d is actually the average complex stiffness (k_H^*) of the fundamental cell in Fig. 2.2(a). So, we define

$$k_H^* = \frac{F_o}{x_{30}} = E_{H2}^* d \qquad (2.1.16)$$

or,

$$\left\| k_H^* \right\| = \frac{F_o}{\left\| x_{30} \right\|} = \left\| E_{H2}^* \right\| d \qquad (2.1.17)$$

$\left\| k_H^* \right\|$ and $\left\| E_{H2}^* \right\|$ will be referred to as the dynamic stiffness and dynamic modulus, respectively.

It should be noted that the parameters k_1, k_2 , k_4 and c_2 in the example system (Fig. 2.5) will be treated as positive numbers, while k_3 could assume a negative value, when desired. Bistable structures are known to have negative stiffness (e.g. in Wang and Lakes (2004a, 2004b, 2005b)). A negative k_3 can be implemented via a bistable structure. The reason to allow k_3 to be negative is to achieve a dynamic stiffness/modulus that softens with frequency.

2.2. Conditions for Stable Softening of Dynamic Modulus

2.2.1 Conditions for softening

From (2.1.17), it can be seen that dynamic stiffness and dynamic modulus are proportional to each other. For convenience, softening of dynamic stiffness of the example system in Section 2.1.1 will be investigated. We have (from equations 2.1.14 and 2.1.16),

$$\left\|k_H^*\right\| = \left\|\frac{k_4[k_3(k_2+ic_2\omega)+k_1(k_2+k_3+ic_2\omega)]}{k_3(k_2+ic_2\omega)+(k_1+k_4)(k_2+k_3+ic_2\omega)}\right\| \tag{2.2.1}$$

By analyzing (2.2.1), we find that $\frac{\partial\left\|k_H^*\right\|}{\partial\omega} < 0$ if and only if

$$k_4[2k_1^2(k_2+k_3)+k_3\{k_3k_4+2k_2(k_3+k_4)\}+2k_1\{k_3(k_3+k_4)+k_2(2k_3+k_4)\}] < 0 .$$

Since $k_2 > 0$, $\frac{\partial\left\|k_H^*\right\|}{\partial\omega}$ is negative provided that

$$K_4[2K_1^2(1+K_3)+K_3\{K_3K_4+2(K_3+K_4)\}+2K_1\{K_3(K_3+K_4)+(2K_3+K_4)\}] < 0 ,$$

where we define

$$K_1 = \frac{k_1}{k_2} \tag{2.2.2}$$

$$K_3 = \frac{k_3}{k_2} \tag{2.2.3}$$

$$K_4 = \frac{k_4}{k_2} \tag{2.2.4}$$

Since $K_4 > 0$, we get that a necessary condition for $\frac{\partial \left\| k_H^* \right\|}{\partial \omega} < 0$ is

$$2K_1^2(1+K_3)+K_3[K_3K_4+2(K_3+K_4)]+2K_1[K_3(K_3+K_4)+2K_3+K_4]<0$$

We now define the function ψ as

$$\psi(K_1,K_3,K_4)=2K_1^2(1+K_3)+K_3[K_3K_4+2(K_3+K_4)]+2K_1[K_3(K_3+K_4)+2K_3+K_4] \tag{2.2.5}$$

It follows that $\frac{\partial \left\| k_H^* \right\|}{\partial \omega}$ is negative if and only if $\psi(K_1,K_3,K_4)<0$.

Since k_1 and k_4 are made from same material, $K_4 > 0$ also implies $K_1 > 0$. Since both K_1 and K_4 are positive, the requirement $\frac{\partial \left\| k_H^* \right\|}{\partial \omega} < 0$ is satisfied whenever $K_{3\min} < K_3 < K_{3\max}$, where

$$K_{3\min} = \frac{-2K_1 - K_1^2 - K_4 - K_1K_4 - \sqrt{K_1^4 + 2K_1^3K_4 + K_4^2 + K_1^2K_4^2}}{2+2K_1+K_4} \tag{2.2.6}$$

$$K_{3\max} = \frac{-2K_1 - K_1^2 - K_4 - K_1K_4 + \sqrt{K_1^4 + 2K_1^3K_4 + K_4^2 + K_1^2K_4^2}}{2+2K_1+K_4} \tag{2.2.7}$$

$K_{3\max}$ may be written as

$$K_{3\max} = \frac{-2K_1 - K_1^2 - K_4 - K_1K_4 + \sqrt{(K_1^2 + K_1K_4)^2 + K_4^2}}{2 + 2K_1 + K_4} \tag{2.2.8}$$

Since both K_1 and K_4 are positive, $K_{3\min}$ is negative and since $\sqrt{(K_1^2 + K_1K_4)^2 + K_4^2} < (K_1^2 + K_1K_4) + K_4$ for any positive K_1 and K_4, $K_{3\max}$ is also negative. Thus, the condition for the frequency-induced softening (i.e., $\frac{\partial \left\| k_H^* \right\|}{\partial \omega} < 0$) is $K_{3\min} < K_3 < K_{3\max} < 0$.

Thus a negative stiffness spring is needed to achieve frequency softening.

2.2.2 Conditions for stability

In this section, the stability of the system in Fig.2.5 will be examined for a static force F.

Equation (2.1.10) can be rewritten as the following three equations

$$c_2\dot{x}_1 - c_2\dot{x}_2 + (k_1 + k_2 + k_4)x_1 - k_2x_2 - k_4x_3 = 0 \tag{2.2.9}$$

$$-c_2\dot{x}_1 + c_2\dot{x}_2 - k_2x_1 + (k_2 + k_3)x_2 = 0 \tag{2.2.10}$$

$$-k_4x_1 + k_4x_3 = F \tag{2.2.11}$$

Adding (2.2.9) and (2.2.10), we get

$$(k_1 + k_4)x_1 + k_3x_2 - k_4x_3 = 0 \tag{2.2.12}$$

From (2.2.11) and (2.2.12) for $k_3 \neq 0$ and $k_4 \neq 0$,

$$x_1 = \frac{k_4 x_3 - F}{k_4} \tag{2.2.13}$$

$$x_2 = \frac{F(k_1 + k_4) - k_1 k_4 x_3}{k_3 k_4} \tag{2.2.14}$$

Differentiating (2.2.13) and (2.2.14),

$$\dot{x}_1 = \dot{x}_3 \tag{2.2.15}$$

$$\dot{x}_2 = -\frac{k_1}{k_3}\dot{x}_3 \tag{2.2.16}$$

Substituting (2.2.15) and (2.2.16) in (2.2.10), we get

$$\frac{c_2(k_1 + k_3)k_4\dot{x}_3 + [k_2k_3 + k_1(k_2 + k_3)]k_4x_3 - F[k_1(k_2 + k_3) + k_3k_4 + k_2(k_3 + k_4)]}{k_3k_4} = 0$$

(2.2.17)

or,

$$c_2(k_1 + k_3)k_4\dot{x}_3 + [k_2k_3 + k_1(k_2 + k_3)]k_4x_3 - F[k_1(k_2 + k_3) + k_3k_4 + k_2(k_3 + k_4)] = 0$$

(2.2.18)

Solving the differential equation (2.2.18) we get

$$x_3 = \left(1 - e^{\Lambda t}\right)\frac{F[k_1(k_2 + k_3) + k_3k_4 + k_2(k_3 + k_4)]}{[k_2k_3 + k_1(k_2 + k_3)]k_4} \tag{2.2.19}$$

where

$$\Lambda = -\frac{k_2k_3 + k_1(k_2 + k_3)}{c_2(k_1 + k_3)} \tag{2.2.20}$$

We define

$$k_{eff} = \frac{[k_2 k_3 + k_1(k_2 + k_3)]k_4}{[k_1(k_2 + k_3) + k_3 k_4 + k_2(k_3 + k_4)]} \qquad (2.2.21)$$

k_{eff} is actually the static stiffness of the system. From (2.2.19) and (2.2.20), we find that x_3 is bounded if $\Lambda < 0$. Furthermore the effective stiffness of the system (i.e. k_{eff}) must be positive so that the external force will do positive work. A negative work done by the external work is an indication of instability. In other words, the system is stable if

$$\Lambda < 0 \text{ and } k_{eff} > 0 \qquad (2.2.22)$$

Since c_2 is positive (and real), the conditions for the stability of the system is $\frac{K_3 + K_1(1+K_3)}{K_1 + K_3} > 0$ and $k_{eff} > 0$. The first condition (i.e. $\Lambda < 0$) is satisfied if any one of the following two conditions is satisfied:

(i) $K_3 + K_1(1+K_3) > 0$ and $K_1 + K_3 > 0$, (2.2.23)

(ii) $K_3 + K_1(1+K_3) < 0$ and $K_1 + K_3 < 0$ (2.2.24)

Since $K_1 > 0$ and $K_3 < 0$, the system is stable (i.e. x_3 is bounded) if and only if $k_{eff} > 0$ and any of the following two conditions is satisfied:

(i) $K_3 + K_1(1+K_3) > 0$, (2.2.25)

(ii) $K_1 + K_3 < 0$ (2.2.26)

2.2.3 Combined conditions for softening and stability

From section 2.2.1 we know that the dynamic stiffness of the example system decreases with increase in the forcing frequency if and only if $\psi < 0$, whereas in section 2.2.2 we learned that the example system is stable if and only if $\Lambda < 0$ and $k_{eff} > 0$. The goal of this section is to investigate whether both the softening and stability conditions can be satisfied simultaneously. Although there are two stability conditions to be satisfied simultaneously (viz. $\Lambda < 0$ and $k_{eff} > 0$), only the first stability condition (i.e. $\Lambda < 0$) will be applied to test whether the example system in Fig. 2.5 is stable in the frequency-induced softening regime. The second stability condition (i.e. $k_{eff} > 0$) can be numerically checked later, once the two conditions $\psi < 0$ and $\Lambda < 0$ are simultaneously satisfied.

As given in section 2.2.2, $\Lambda < 0$ if and only if any of the following two conditions is satisfied:

(i) $K_3 + K_1(1+K_3) > 0$,

(ii) $K_1 + K_3 < 0$

We will check whether one of these two conditions ((i) and (ii)) and $\psi < 0$ can be satisfied simultaneously.

(i) Satisfying $K_3 + K_1(1+K_3) > 0$ ***and*** $\psi < 0$

We define Y as

$$Y = K_3 + \frac{K_1}{(1+K_1)} \qquad (2.2.27)$$

or

$$K_3 = -\frac{K_1}{(1+K_1)} + Y \qquad (2.2.28)$$

Inequality (2.2.25), i.e., $K_3 + K_1(1+K_3) > 0$ is true if and only if $Y > 0$.

Substituting (2.2.28) in (2.2.5), we get

$$\psi = \Big[2K_1^4 Y + 2K_1^3 Y(2+K_4+Y) + Y\big(2Y + K_4(2+Y)\big) + 2K_1 Y\big(3Y + K_4(2+Y)\big) + K_1^2\big(2Y(1+3Y) + K_4(1+4Y+Y^2)\big)\Big] \Big/ (1+K_1)^2 \qquad (2.2.29)$$

We find from (2.2.29) that $Y > 0$ implies $\psi > 0$ and (from Section 2.2.1) we know that $\psi > 0$ implies $\frac{\partial \left\| k_H^* \right\|}{\partial \omega} > 0$. It follows that the condition $K_3 + K_1(1+K_3) > 0$ results in hardening of the dynamic stiffness with the increase in the forcing frequency. Thus stability condition $K_3 + K_1(1+K_3) > 0$ and the softening condition $\psi < 0$ cannot be satisfied simultaneously.

(ii) Satisfying $K_1 + K_3 < 0$ ***and*** $\psi < 0$

We will now check whether $K_1 + K_3 < 0$ and $\psi < 0$ can be simultaneously satisfied.

We define Z as

$$Z = -K_1 - K_3 \tag{2.2.30}$$

or

$$K_3 = -K_1 - Z \tag{2.2.31}$$

The inequality $K_1 + K_3 < 0$ is equivalent to $Z > 0$. Substituting (2.2.31) in (2.2.5), we get

$$\psi = -K_1^2(K_4 - 2Z) + 2K_1 Z^2 + Z[K_4(-2+Z) + 2Z] \tag{2.2.32}$$

$\psi < 0$ implies

$$\frac{-K_1^2 + K_4 - \sqrt{(K_1^2 + K_1 K_4)^2 + K_4^2}}{2 + 2K_1 + K_4} < Z < \frac{-K_1^2 + K_4 + \sqrt{(K_1^2 + K_1 K_4)^2 + K_4^2}}{2 + 2K_1 + K_4}$$

The conditions $\psi < 0$ and $Z > 0$ are satisfied if and only if

$$0 < Z < \frac{-K_1^2 + K_4 + \sqrt{(K_1^2 + K_1 K_4)^2 + K_4^2}}{2 + 2K_1 + K_4}$$

or

$$0 > K_1 + K_3 > \frac{K_1^2 - K_4 - \sqrt{(K_1^2 + K_1 K_4)^2 + K_4^2}}{2 + 2K_1 + K_4}$$

or

$$\frac{K_1^2 - K_4 - \sqrt{(K_1^2 + K_1 K_4)^2 + K_4^2}}{2 + 2K_1 + K_4} - K_1 < K_3 < -K_1$$

In summary, we have found that the example system in Fig. 2.5 exhibit a stable frequency-induced softening if and only if the following two conditions are simultaneously satisfied:

(a) $k_{eff} > 0$ and

(b) $\dfrac{K_1^2 - K_4 - \sqrt{(K_1^2 + K_1 K_4)^2 + K_4^2}}{2 + 2K_1 + K_4} - K_1 < K_3 < -K_1$.

2.2.4 Numerical example

Here, the example system (shown in Fig. 2.5 and again in Fig. 2.6) will be studied with $K_1 = \dfrac{k_1}{k_2} = 0.3$ and $K_4 = \dfrac{k_4}{k_2} = 0.1$. With these values, $\Lambda < 0$ requires $-0.3616 < K_3 < -0.3$. We choose $K_3 = \dfrac{k_3}{k_2} = -0.304$ and also $\dfrac{c_2}{k_2} = 0.0002$. The system is loaded with a periodic force, $F = F_o \sin(\omega t)$.

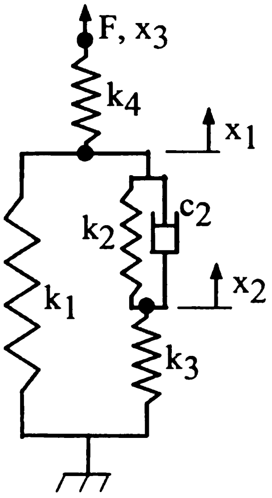

Figure 2.6. Spring-dashpot system with boundary conditions

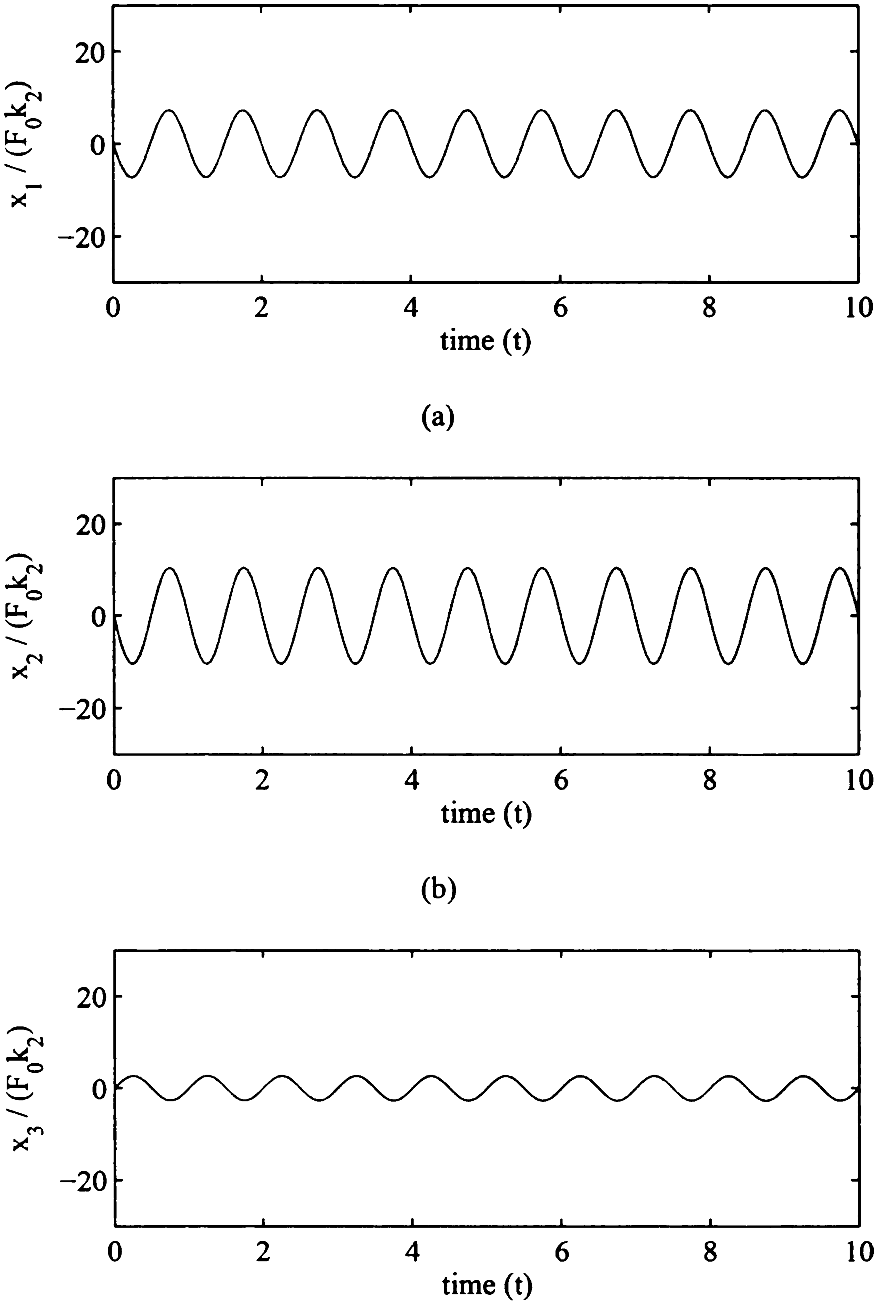

(a)

(b)

(c)

Figure 2.7. $x_1(t)$, $x_2(t)$ and $x_3(t)$ at the reference parameters and forcing frequency 1 Hz

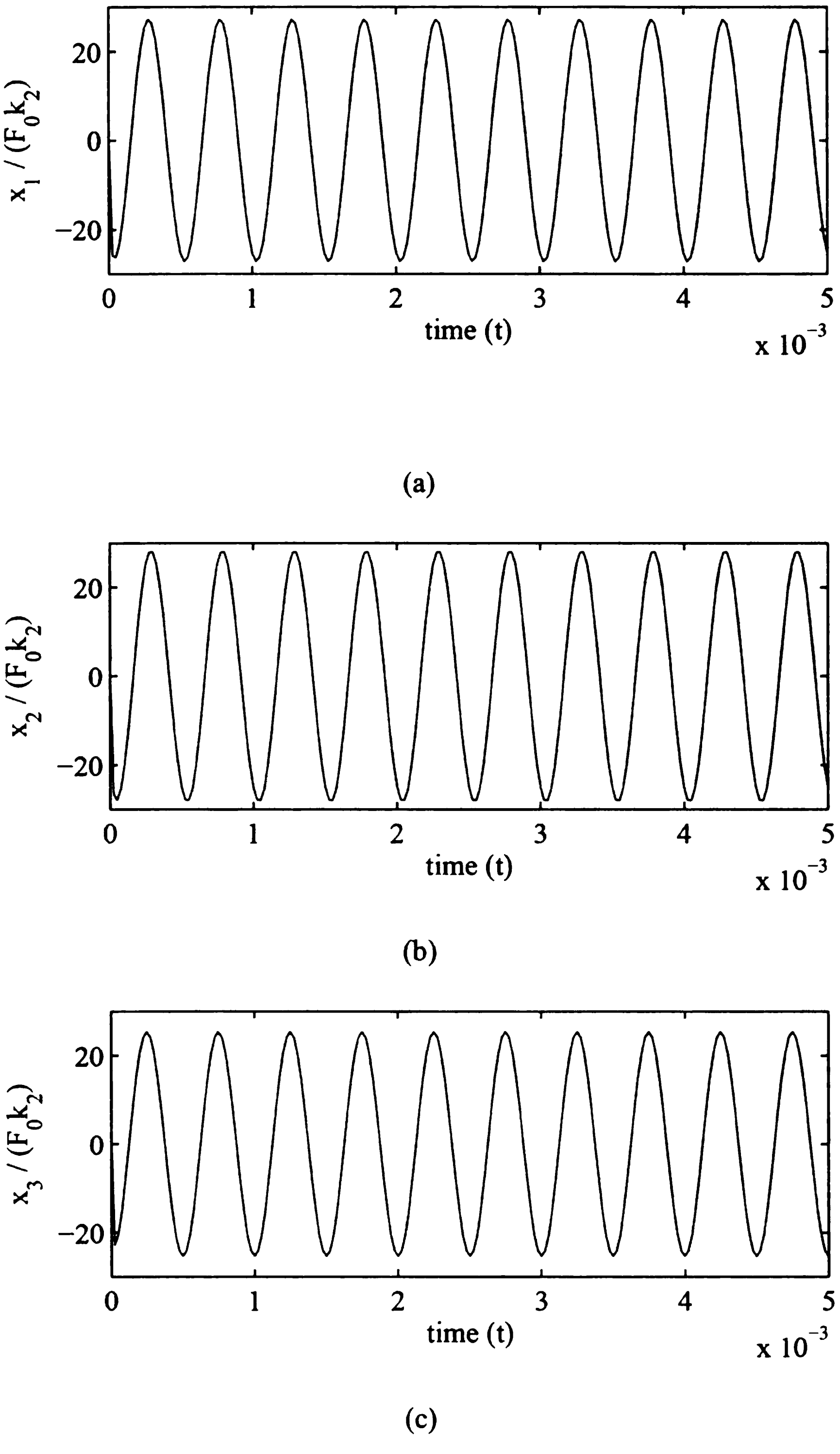

Figure 2.8. $x_1(t)$, $x_2(t)$ and $x_3(t)$ at the reference parameters and forcing frequency 2000Hz

Figure 2.7 shows plots of (non-dimensionalized) $x_1(t)$, $x_2(t)$ and $x_3(t)$, when the forcing frequency is 1 Hz. Figure 2.8 shows the plot of $x_1(t)$, $x_2(t)$ and $x_3(t)$, when the forcing frequency is 2000 Hz. As can be seen in the figures, the x_i 's are bounded, showing stability of the system.

When the condition $-0.3616 < K_3 < -0.3$ is violated, the system is not simultaneously stable and in the dynamic-stiffness softening regime. For example, when K_3 in the reference parameters is changed to -0.24, the system is not stable about the initial conditions (i.e. $x_i(0) = 0$). Figure 2.9 shows the plot of $x_3(t)$ with $K_3 = -0.24$ and $f = \omega/(2\pi) =$ 2000 Hz. As can be seen in Fig. 2.9, $x_3(t)$ is departs from the initial condition $x_3(0) = 0$, signifying local instability of the system.

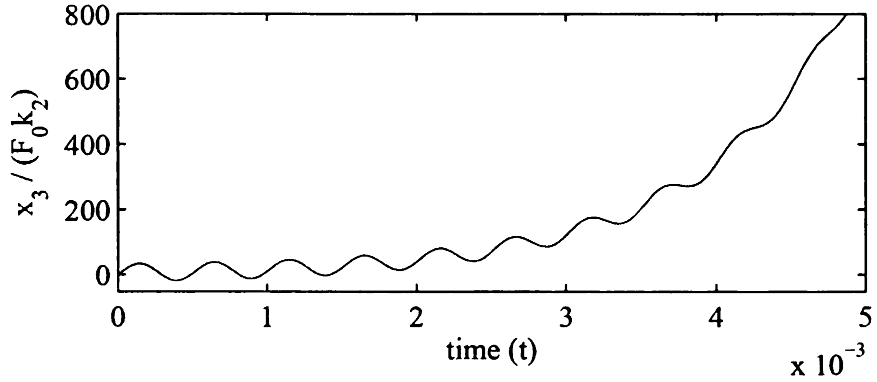

Figure 2.9. $x_3(t)$ with $K_3 = -0.24$ and frequency = 2000 Hz

When K_3 in the reference parameters is changed to -0.39, the dynamic stiffness increases with the increase in the forcing frequency. Figures 2.10 and 2.11 show the plot of $x_3(t)$ when the forcing frequency is 1 Hz and 2000 Hz, respectively. As can be seen, the amplitude of $x_3(t)$ is smaller when the forcing frequency is higher, indicating hardening.

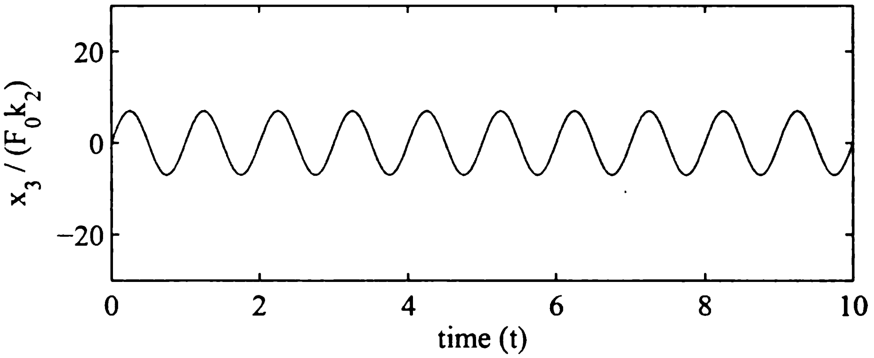

Figure 2.10. $x_3(t)$ with $K_3 = -0.39$ and forcing frequency 1Hz

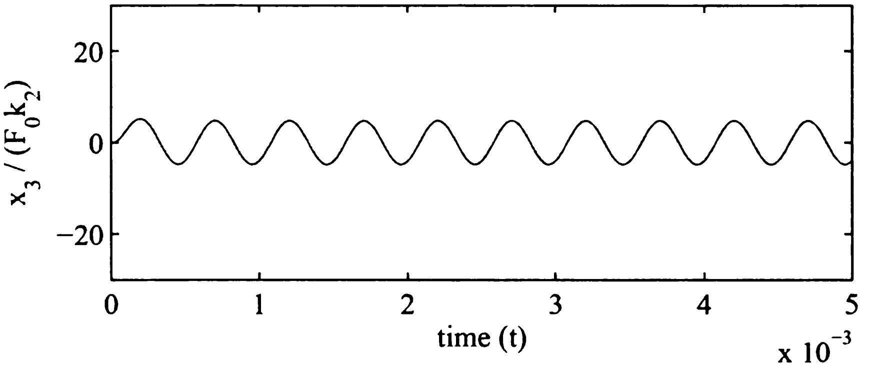

Figure 2.11. $x_3(t)$ with $K_3 = -0.39$ and forcing frequency 2000Hz

At the reference parameters (viz., $K_1 = \frac{k_1}{k_2} = 0.3$, $K_3 = \frac{k_o}{k_2} = \frac{k_3}{k_2} = -0.304$, $K_4 = \frac{k_4}{k_2} = 0.1$ and $\frac{c_2}{k_2} = 0.0002$), the corresponding plots of the absolute value of the effective stiffness (i.e. $\left\| k_H^* \right\|$), the real part of the effective stiffness (i.e. $\mathrm{Re}(k_H^*)$) and the imaginary part of the effective stiffness as functions of the forcing frequency are shown in Figs. 2.12 (a), (b) and (c) respectively. In the stiffness plots, the stiffness will be scaled (and made non-dimensional) by dividing it by k_2. As can be seen in Fig. 2.12(a), the static scaled dynamic stiffness is approximately 0.38. With increase in the forcing frequency, the stiffness monotonically decreases. The stiffness value is approximately 0.05 at the frequency 2000 Hz. It can also be seen in Fig. 2.12 (b) that the real part of the effective stiffness is positive for the whole frequency range shown, i.e. in the range 0-2000 Hz.

Now, the effect of changing $\frac{c_2}{k_2}$ will be studied. When $\frac{c_2}{k_2}$ is changed to 0.02, we observe increase in the curvature of the dynamic stiffness vs. frequency curve, as in Fig. 2.13. $\frac{c_2}{k_2}$ thus seems to be an important parameter for tuning or achieving a desired dynamic stiffness vs. frequency curve.

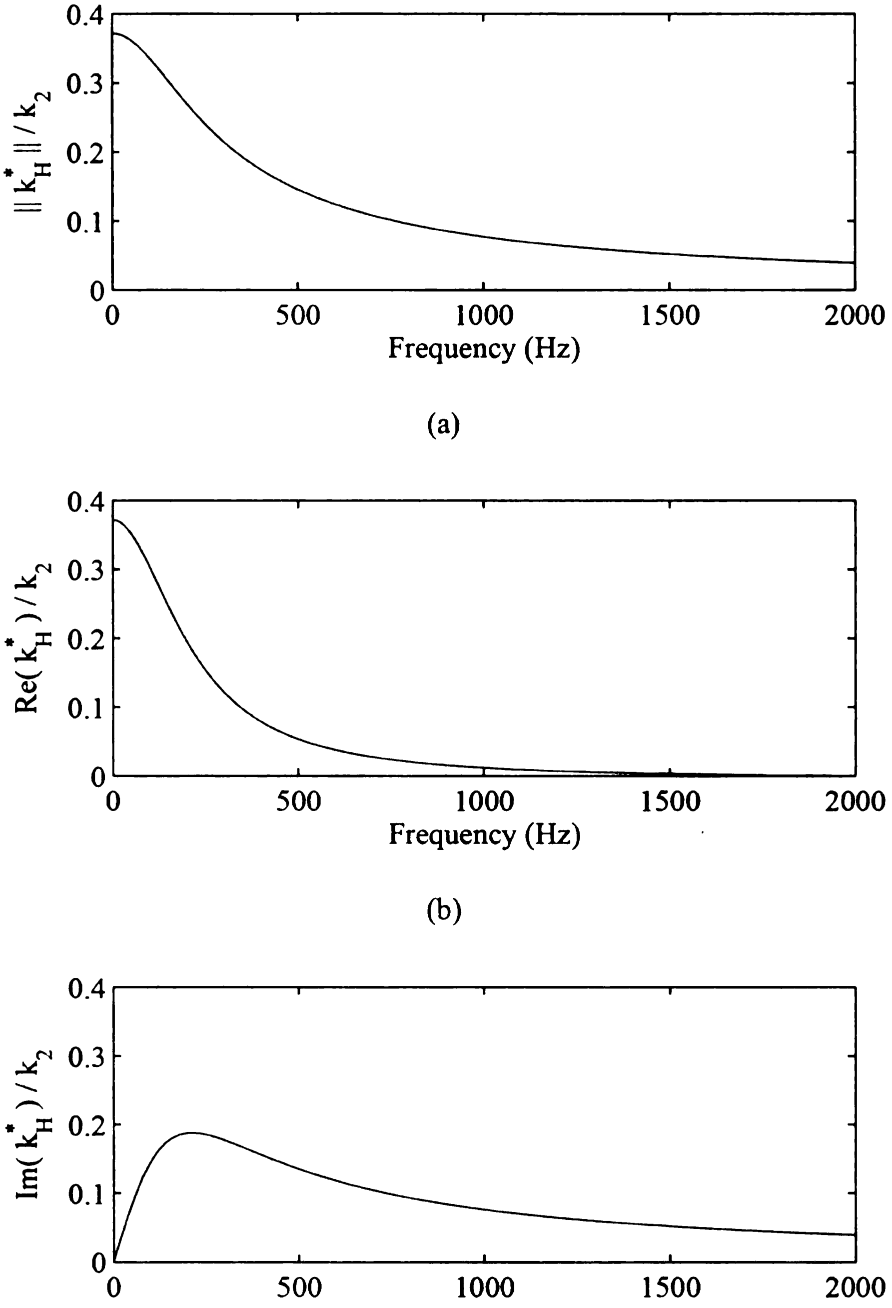

Figure 2.12. Absolute value (a), real part (b) and imaginary part (c) of the effective stiffness (k_H^*).

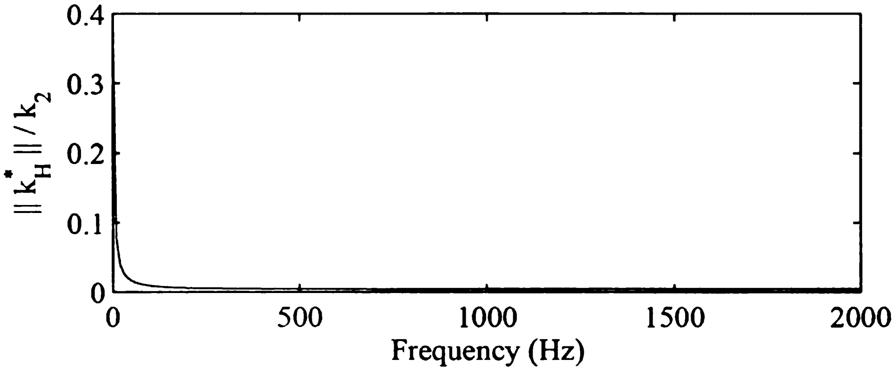

Figure 2.13. Dynamic stiffness vs. the forcing frequency with $c_2 / k_2 = 0.02$

2.3. Estimation of Composite Material Parameters

The two-dimensional composite material in Fig. 2.1 was simplified into the one dimensional model in Fig. 2.5 to analyze the material for frequency-induced softening and stability. The parameters of the one-dimensional model (i.e. k_1, k_2, k_3, k_4 and c_2) will now be used to construct a two-dimensional composite model. The parameters for the two-dimensional composite model are the complex moduli ($E_A^* = E_A$; and E_B^*) of the two phases A and B, the length fractions of phase B in horizontal and vertical directions (i.e. λ_2 and ϕ_2 in Fig. 2.2) and $d = \dfrac{WD}{L}$ (equation (2.1.9)). There are 5 unknown parameters (E_A, E_B^*, λ_2 , ϕ_2 and d) for the two-dimensional composite model and 3 equations, namely (2.1.4) (2 equations) and (2.1.5). Thus there are two free choices to be made to satisfy the three equations relating the parameters of the 1-D model to the parameters of the composite material.

From (2.1.4),

$$E_A d = \frac{k_1 \phi_2}{(1-\lambda_2)} = k_4(1-\phi_2) \tag{2.3.1}$$

or

$$\frac{(1-\phi_2)(1-\lambda_2)}{\phi_2} = \frac{k_1}{k_4} \tag{2.3.2}$$

where

$$0 < \lambda_2 < 1 \tag{2.3.3}$$

and

$$0 < \phi_2 < 1 \tag{2.3.4}$$

In equation (2.3.2), k_1 and k_4 are given data. λ_2 and ϕ_2 are chosen such that they satisfy (2.3.2)-(2.3.4).

From (2.1.4) and (2.1.5),

$$\frac{E_B^*}{E_A} = \frac{k_3(k_2 + ic_2\omega)}{(k_3 + k_2 + ic_2\omega)} \frac{(1-\lambda_2)}{\lambda_2 k_1} \tag{2.3.5}$$

If d is prescribed, E_A is computed using (2.3.1) and E_B^* is computed using (2.3.5). Alternatively, E_A may be prescribed and the corresponding d is computed using

$$d = \frac{k_4(1-\phi_2)}{E_A} \tag{2.3.6}$$

2.3.1 Example phase properties

A one-dimensional example which shows frequency-induced softening as well as stability has the following parameters: $K_1 = \frac{k_1}{k_2} = 0.3$, $K_4 = \frac{k_4}{k_2} = 0.1$, $K_3 = \frac{k_3}{k_2} = -0.304$ and $\frac{c_2}{k_2} = 0.0002$. Using equations in this section, the corresponding parameters for the two-dimensional composite model (viz., E_A, E_B^*, λ_2, ϕ_2 and d) are found.

A square fundamental cell is assumed and thus $\lambda_2 = \phi_2$. From (2.3.2)-(2.3.4),

$$\frac{(1-\phi_2)(1-\phi_2)}{\phi_2} = \frac{k_1}{k_4} = \frac{0.3}{0.1} = 3$$

or

$$\lambda_2 = \phi_2 = 0.2087 \approx 0.2$$

$$\frac{E_B^*}{E_A} = \frac{k_3(k_2 + ic_2\omega)}{(k_3 + k_2 + ic_2\omega)} \frac{(1-\lambda_2)}{\lambda_2 k_1} = -\frac{4.053 + i0.0008\omega}{0.696 + i0.0002\omega} \tag{2.3.7}$$

At $\omega = 0$,

$$\left.\frac{E_B^*}{E_A}\right|_{\omega=0} = -5.824$$

and thus the Young's modulus for material B is negative.

The elastic tensor for material A is given by

$$C_A = \frac{E_A}{1-\nu_A^2}\begin{bmatrix} 1 & \nu_A & 0 \\ \nu_A & 1 & 0 \\ 0 & 0 & (1-\nu_A)/2 \end{bmatrix} \tag{2.3.8}$$

where ν_A is the prescribed Poisson's ratio for phase A.

The elastic tensor for material B is given by

$$C_B = \frac{E_B^*}{1-\nu_B^2}\begin{bmatrix} 1 & \nu_B & 0 \\ \nu_B & 1 & 0 \\ 0 & 0 & (1-\nu_B)/2 \end{bmatrix} \tag{2.3.9}$$

where ν_B is the prescribed Poisson's ratio for phase B.

The complex shear modulus of Material B is given by

$$G_B^* = \frac{E_B^*}{2(1+\nu_B)} \tag{2.3.10}$$

Note that the shear modulus of material B is negative as the material is isotropic and the Young's modulus is negative. A negative shear modulus indicates the elastic moduli are not strongly elliptic (Lakes and Drugan (2002)). If strong ellipticity is violated, the material may exhibit an instability associated with the formation of bands of heterogeneous deformation. However, the violation of strong ellipticity does not guarantee the loss of stability of the inclusions: experiments show that the energy penalty of band formation suppresses banding when particles of the material are sufficiently small. Thus an instability criterion based purely on elasticity theory may not contain enough of the physics of the actual material behavior, and hence may predict instabilities in regimes where such do not occur in reality (Lakes and Drugan (2002)).

In essence, small-size inclusions of Material B may have potential to achieve the frequency-induced softening; however, elasticity theories predict instability of the composite material. While the physics suitable for the small-size inclusions of material B in the matrix of material A needs to be studied further, inclusions of lumped lattices of material B (made of springs and dampers) are used in the matrix of material A to achieve frequency-induced softening in this work. Note that negative shear modulus can also occur in the lumped elements; however the lumped elements cannot form bands and the continuum conditions of ellipticity do not apply to the lumped elements (Lakes and Drugan (2002)).

2.4 Stability of Negative Stiffness Phase B

The inclusions of phase B with negative shear modulus will be unstable and therefore cannot be used directly. Instead, an anisotropic phase B is needed that has a negative Young's modulus, but also a positive shear modulus enough to maintain stability under prescribed displacement at the phase boundary.

In order to avoid loss of stability, a model for an anisotropic phase B is proposed, whereby B is itself a mixture of two isotropic constituents, B_1 and B_2. In this model, a constituent with negative stiffness (B_1) is always surrounded by a second phase of stable material (B_2). One such arrangement is shown in Fig. 2.14. The resulting effective properties of phase B correspond to a "rank 1" layering of B_1 and B_2 along the horizontal direction (direction 1). The effective elastic tensor for phase B is computed using the following standard layering formulas (given e.g. in Hassani and Hinton (1999)):

$$b_{11}(\omega) = \frac{q_{11} r_{11}}{(1-g) r_{11} + g q_{11}} \tag{2.4.1}$$

$$b_{12}(\omega) = \left(g \frac{r_{12}}{r_{11}} + (1-g) \frac{q_{12}}{q_{11}} \right) b_{11}(\omega) \tag{2.4.2}$$

$$b_{22}(\omega) = \left(g r_{22} + (1-g) q_{22} \right) - \left(g \frac{r_{12}^2}{r_{11}} + (1-g) \frac{q_{12}^2}{q_{11}} \right) + \frac{(b_{12}(\omega))^2}{b_{11}(\omega)} \tag{2.4.3}$$

$$b_{33}(\omega) = \frac{q_{33} r_{33}}{(1-g) r_{33} + g q_{33}} \tag{2.4.4}$$

where q_{ij} and r_{ij} are the ij-components of the elastic tensors (C_{B1} and C_{B2}) for phases B_1 and B_2, respectively. g is the volume fraction of B_2 in B. The effective elastic tensor is given by

$$C_B = \begin{bmatrix} b_{11}(\omega) & b_{12}(\omega) & 0 \\ b_{12}(\omega) & b_{22}(\omega) & 0 \\ 0 & 0 & b_{33}(\omega) \end{bmatrix} \tag{2.4.5}$$

With suitable values for the free parameters g, C_{B1} and C_{B2}, the rank-1 set up can result in an elastic tensor for B where the 2-2 entry (C_{2222}) is negative while 3-3 entry (C_{1212}) is positive, i.e., B has positive shear modulus. The choice of B_2 is somewhat arbitrary (as long as it is a standard material). Both A and B_2 are chosen to be made of the same material. An idealization of B_1 using a lumped parameter model is discussed next.

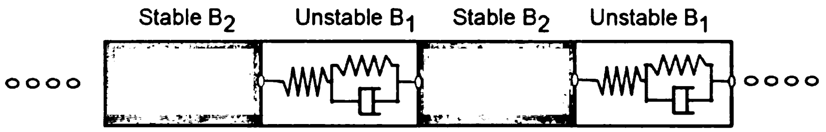

Figure 2.14. A potential arrangement of constituents B_1 and B_2 to form material B

2.5. Implementation of Negative Stiffness

As discussed in Section 2.2, negative stiffness is important for the frequency-induced softening of the dynamic stiffness of the system in Fig. 2.5. Negative stiffness can be implemented using a bistable structure. Figure 2.15 shows a simple example of a bistable structure. The hollow circles in the figure denote the hinges in the structure. There are two linear springs in the structure, each hinged at both ends. The Y-shaped support structure is assumed to be rigid. The springs are connected such that they form an arch-shape as shown in the figure. *h* is the vertical distance between the two ends of either spring. Similarly, *L* is the horizontal distance between the two ends of either spring.

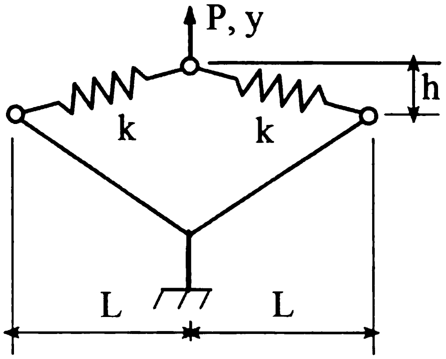

Figure 2.15. A simple bistable structure

A vertical force P is applied at the common joint of the two springs, as shown in the figure. y is the corresponding vertical displacement. The strain energy of the bistable structure in Fig. 2.15 is given by,

$$\Psi(y) = 2\left(\frac{1}{2}k\Delta^2\right) \tag{2.5.1}$$

where

$$\Delta = \sqrt{(h+y)^2 + L^2} - \sqrt{h^2 + L^2} \tag{2.5.2}$$

The (equilibrium) force corresponding to displacement y is given by

$$P = \frac{d\Psi}{dy} = 2k\Delta\ \frac{d\Delta}{dy} \tag{2.5.3}$$

The stiffness of the structure is given by

$$k_n = \frac{dP}{dy} = \frac{d^2\Psi}{dy^2} \tag{2.5.4}$$

Figure 2.16 shows the typical plot of the applied force (P) versus the resulting displacement (y). Figure 2.17 shows the corresponding plot of the stiffness (k_n) versus the displacement (y). As can be seen in Fig. 2.17, the bistable structure has negative stiffness for some displacement values. The negative stiffness corresponds to the negative slope of the force-displacement diagram (Fig. 2.16).

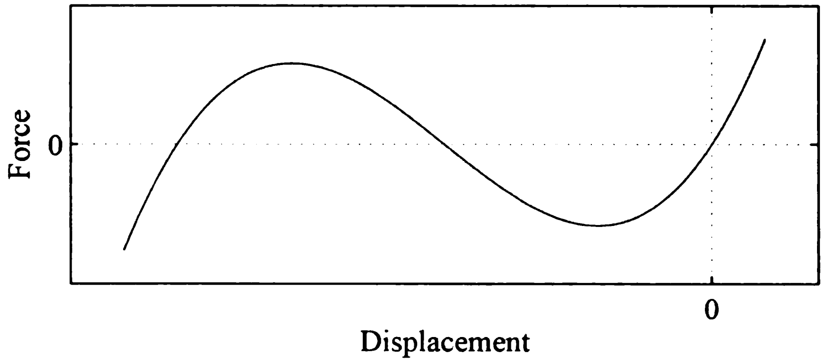

Figure 2.16. A typical force-displacement diagram for a bistable structure

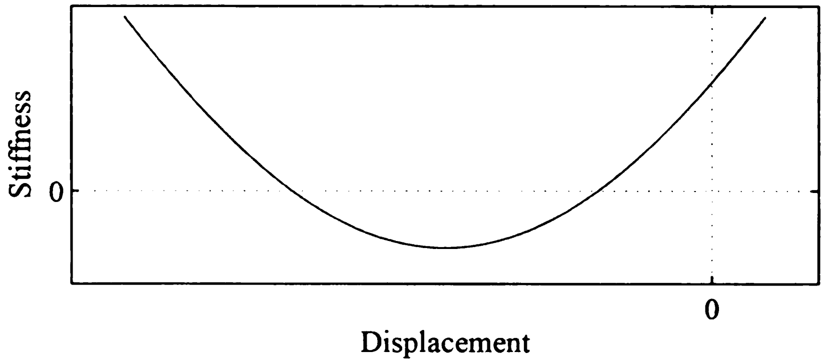

Figure 2.17. A typical stiffness-displacement diagram for a bistable structure

In the present example, the stiffness is negative for

$$y \in (y_l, y_h) \tag{2.5.5}$$

where

$$y_l = -h - L\sqrt{\left(\frac{h^2}{L^2}+1\right)^{1/3} - 1} \tag{2.5.6}$$

$$y_h = -h + L\sqrt{\left(\frac{h^2}{L^2}+1\right)^{1/3} - 1} \tag{2.5.7}$$

The stiffness is most negative at $y=-h$ and the corresponding value of the stiffness at that point is

$$k_o = 2k\left(1-\sqrt{\frac{h^2}{L^2}+1}\right) \tag{2.5.8}$$

Note that $y=-h$ corresponds to the two springs aligned, as shown in Fig. 2.18. The structure shown is the figure can be used to achieve negative stiffness. However, the stiffness is not constant and also the displacement (y) is to be strictly in the range (y_l, y_h) in order to attain negative stiffness. In contrast, in the examples in section 2.2, k_3 is a negative constant and thus it does not depend on displacements. The desired negative stiffness will be approximately achieved by appropriately constraining y.

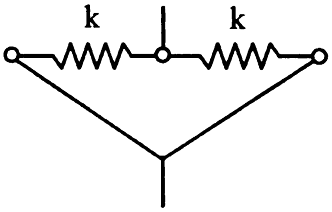

Figure 2.18. Configuration with the maximum negative stiffness

Replacing the negative-stiffness spring (k_3) in the original system (Fig. 2.5) with the configuration in Fig. 2.18, we get a new system that can be represented schematically as shown in Fig. 2.19.

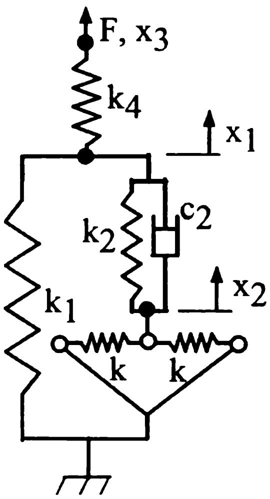

Figure 2.19. Negative stiffness implementation

In Fig. 2.19, $x_2 = 0$ corresponds to $y = -h$. Thus, x_2 and y are related as

$$x_2 = y + h \qquad (2.5.9)$$

For very small oscillations around $x_2 = 0$ (equivalently $y = -h$), i.e. for $|x_2| << |y_h - y_l|$ (or $\left|\frac{x_2}{L}\right| << 2\sqrt{\left(\frac{h^2}{L^2}+1\right)^{1/3} - 1}$), the stiffness k_n (in (2.5.4)) will be approximately constant at k_o (given in (2.5.8)) and the system in Fig. 2.19 will behave approximately same as the linear system in Fig. 2.5.

2.6 A Lumped System Realization of Phase B₁

One way to visualize the behavior and inner-workings of phase B₁ is to use a lumped lattice of springs and dampers where some of the springs have negative stiffness.

Negative stiffness may be realized using e.g., bistable structures as shown in the previous section. Figure 2.20 shows a potential lumped lattice configuration. As shown in the figure, the lattice is a four-noded square, with two degrees of freedom at each node. The nonlinear springs in the figure (shown as springs with an arrow across) correspond to bistable structures that can be used to provide the desired negative stiffness. Material phase B_1 is obtained by tiling a plane with the two dimensional lattice shown in Fig. 2.20.

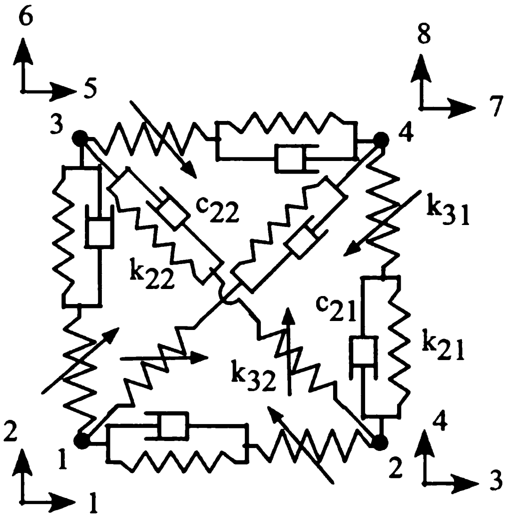

Figure 2.20. Two-dimensional lattice of phase B_1

The 2D lumped lattice in Fig. 2.20 is basically made up of 6 standard linear solid (SLS) elements interconnecting the 4 nodes. k_{ij} and c_{ij} in the figure denote spring stiffness and damper coefficient, respectively. The complex stiffness of each of the four identical SLS elements forming the four sides of the lattice is given by

$$s_1 = \frac{k_{31}(k_{21} + i\omega c_{21})}{k_{31} + k_{21} + i\omega c_{21}} \qquad (2.6.1)$$

Similarly, the complex stiffness of either of the two identical SLS elements forming the two diagonals of the lattice is given by

$$s_2 = \frac{k_{32}(k_{22} + i\omega c_{22})}{k_{32} + k_{22} + i\omega c_{22}} \tag{2.6.2}$$

The complex stiffness matrix (K_Q^*) for the 2D element in Fig. 2.20 is given by

$$K_Q^* = \begin{bmatrix} s_1 + \frac{s_2}{2} & \frac{s_2}{2} & -s_1 & 0 & 0 & 0 & -\frac{s_2}{2} & -\frac{s_2}{2} \\ \frac{s_2}{2} & s_1 + \frac{s_2}{2} & 0 & 0 & 0 & -s_1 & -\frac{s_2}{2} & -\frac{s_2}{2} \\ -s_1 & 0 & s_1 + \frac{s_2}{2} & -\frac{s_2}{2} & -\frac{s_2}{2} & \frac{s_2}{2} & 0 & 0 \\ 0 & 0 & -\frac{s_2}{2} & s_1 + \frac{s_2}{2} & \frac{s_2}{2} & -\frac{s_2}{2} & 0 & -s_1 \\ 0 & 0 & -\frac{s_2}{2} & \frac{s_2}{2} & s_1 + \frac{s_2}{2} & -\frac{s_2}{2} & -s_1 & 0 \\ 0 & -s_1 & \frac{s_2}{2} & -\frac{s_2}{2} & -\frac{s_2}{2} & s_1 + \frac{s_2}{2} & 0 & 0 \\ -\frac{s_2}{2} & -\frac{s_2}{2} & 0 & 0 & -s_1 & 0 & s_1 + \frac{s_2}{2} & \frac{s_2}{2} \\ -\frac{s_2}{2} & -\frac{s_2}{2} & 0 & -s_1 & 0 & 0 & \frac{s_2}{2} & s_1 + \frac{s_2}{2} \end{bmatrix} \tag{2.6.3}$$

The complex modulus tensor (C_Q) corresponding to the lumped lattice in Fig. 2.20 is of the form:

$$C_Q = \begin{bmatrix} f_{11} & f_{12} & 0 \\ f_{12} & f_{11} & 0 \\ 0 & 0 & f_{33} \end{bmatrix} \qquad (2.6.4)$$

Three numerical tests are conducted to find C_Q:

(i) Tensile test 1: Degrees of freedom 1, 2, 3, 4, 5 and 7 are constrained (zero prescribed displacement) and degrees of freedom 6 and 8 are given unit displacements. f_{11} is the total reaction force along the degrees of freedom 6 and 8. f_{11} is given by

$$f_{11} = 2s_1 + s_2 \qquad (2.6.5)$$

(ii) Tensile test 2: Degree of freedoms 1, 2, 3, 4, 5 and 7 are constrained (zero prescribed displacement) and degrees of freedom 6 and 8 are given unit displacements. f_{12} is the total reaction force along the degrees of freedom 1 and 5. f_{12} is given by

$$f_{12} = s_2 \qquad (2.6.6)$$

(iii) Shear test: Degree of freedoms 1, 2, 3, 4, 6 and 8 are constrained (zero prescribed displacement) and degrees of freedom 5 and 7 are given unit displacements. f_{33} is the total reaction force along the degrees of freedom 5 and 7. f_{33} is given by

$$f_{33} = s_2 \tag{2.6.7}$$

The aim is to construct an isotropic material using the lumped lattice in Fig. 2.20. In other words, we want to express C_Q in the form of (2.3.9), i.e.

$$C_{B1} = \frac{E_{B1}^*}{1-\nu_{B1}^2}\begin{bmatrix} 1 & \nu_{B1} & 0 \\ \nu_{B1} & 1 & 0 \\ 0 & 0 & (1-\nu_{B1})/2 \end{bmatrix} \tag{2.6.8}$$

This is possible if

$$s_1 = s_2 \tag{2.6.9}$$

$$E_{B1}^* = \frac{8s_1}{3} = \frac{8s_2}{3} \tag{2.6.10}$$

and

$$\nu_{B1} = \frac{1}{3} \tag{2.6.11}$$

As an example (to be used in section 4), the following parameters of the lumped lattice in Fig. 2.20 are chosen:

$k_{21} = 8.45E_A$

$k_{31} = -0.304k_{21}$

$c_{21} / k_{21} = 0.0002$

$k_{22} = k_{21}$

$k_{32} = k_{31}$

$c_{22} = c_{21}$

Note that $k_{31}/k_{21} = -0.304$ and $c_{21}/k_{21} = 0.0002$ here are kept the same as k_3/k_2 and c_2/k_2, respectively, in the example in section 2.3.1. The corresponding elastic tensor is C_{Bl} in equation (2.6.8) with

$$E_{B1}^{*} = -\frac{6.8501(1+i0.0002\omega)}{0.696+i0.0002\omega} E_A$$

and $\nu_{B1} = 1/3$.

The lumped system of the negative stiffness material B_1 designed here may be mixed with a typical positive stiffness elastic material B_2 to build rank-1 layered material B (as described in section 2.4). For example, a purely elastic material may be used as phase B_2. The elastic tensor for phase B_2 that will be used here is

$$C_{B2} = \frac{E_A}{1-\nu_{B2}^2} \begin{bmatrix} 1 & \nu_{B2} & 0 \\ \nu_{B2} & 1 & 0 \\ 0 & 0 & (1-\nu_{B2})/2 \end{bmatrix} \qquad (2.6.12)$$

where $\nu_{B2} = 0.3$ is the prescribed Poisson's ratio for phase B_2 and E_{B2} is the Young's Modulus of phase B_2.

If the volume fraction of B_2 in B is 0.8, the elastic tensor for the rank-1 layered material B may be given by

$$C_B = \begin{bmatrix} b_{11}(\omega) & b_{12}(\omega) & 0 \\ b_{12}(\omega) & b_{22}(\omega) & 0 \\ 0 & 0 & b_{33}(\omega) \end{bmatrix}$$

The absolute value, real and imaginary parts of the resulting $b_{11}(\omega)$, $b_{12}(\omega)$, $b_{22}(\omega)$, and $b_{33}(\omega)$ are plotted in Fig. 2.21. $b_{ij}(\omega)$ values in the plots are normalized by E_A. From Fig. 2.21 we find that only one component (b_{22}) is negative and the shear modulus of material B is positive, viz. $0.4954\,E_A$. Material B thus can be made stable when constrained. we also notice that in Fig. 2.21, $\|b_{22}(\omega)\|$ decreases with forcing frequency, while $\|b_{11}(\omega)\|$, $\|b_{12}(\omega)\|$ and $\|b_{33}(\omega)\|$ are approximately constant. Based on this information, it may be possible to synthesize a lumped lattice for material B directly, bypassing the construction of B_1 followed by layering. In the next section, we will use this information and construct such a lumped lattice.

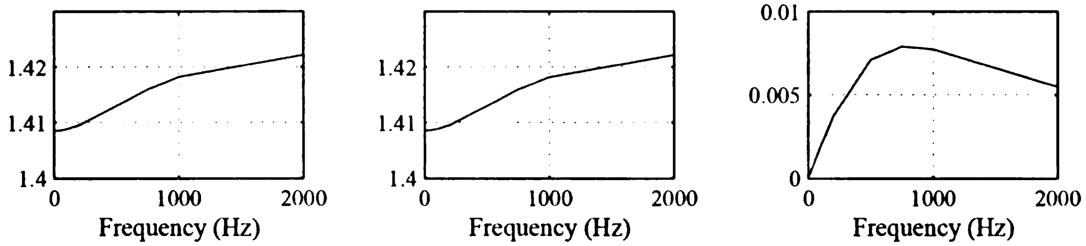

(a) $||b_{11}/E_A||$ (b) $\mathrm{Re}(b_{11}/E_A)$ (c) $\mathrm{Im}(b_{11}/E_A)$

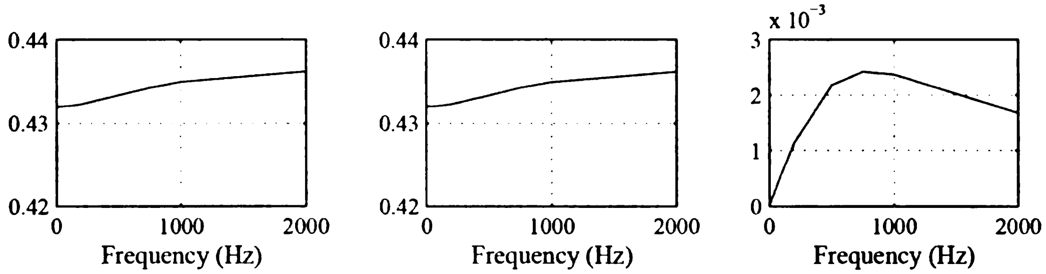

(d) $||b_{12}/E_A||$ (e) $\mathrm{Re}(b_{12}/E_A)$ (f) $\mathrm{Im}(b_{12}/E_A)$

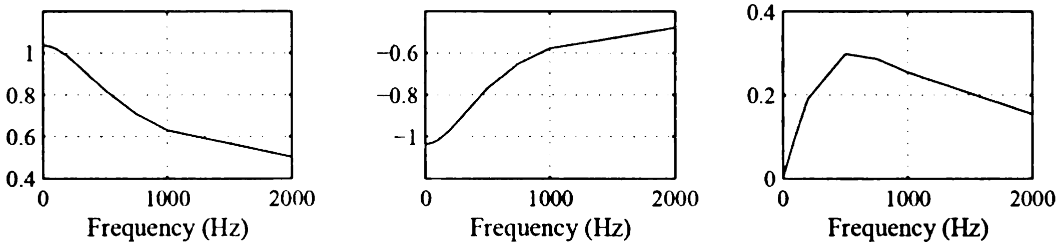

(g) $||b_{22}/E_A||$ (h) $\mathrm{Re}(b_{22}/E_A)$ (i) $\mathrm{Im}(b_{22}/E_A)$

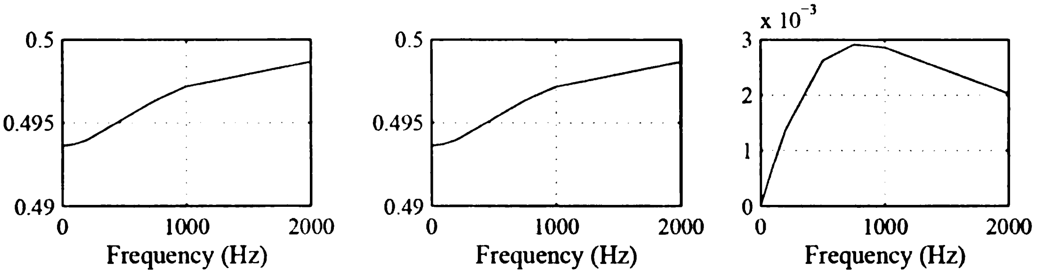

(j) $||b_{33}/E_A||$ (k) $\mathrm{Re}(b_{33}/E_A)$ (l) $\mathrm{Im}(b_{33}/E_A)$

Figure 2.21. Components of the effective elastic tensor of material B

2.7 Phase B as a Lumped System

This section illustrates that it is possible to synthesize a lumped lattice model for phase B directly (bypassing the construction of B_l followed by layering). The aim is to find a phase B material which is approximately the same as that in section 2.6. Phase B in that section is a rank-1 layered material, whereas phase B here is a lumped system and is stable enough to be used as an inclusion. Figure 2.22 shows a potential lumped lattice configuration for phase B. As shown in the figure, the lattice is a four-noded square, with two degrees of freedom at each node. *k*s and *c*s in the figure represent spring stiffnesses and damper coefficients, respectively. The concentric circles at the four corners represent rotational springs at the four corners. The nonlinear springs in the figure (shown as springs with an arrow across) correspond to bistable structures that can be used to provide the desired negative stiffness. Material phase B is obtained by tiling a plane with this two dimensional lattice.

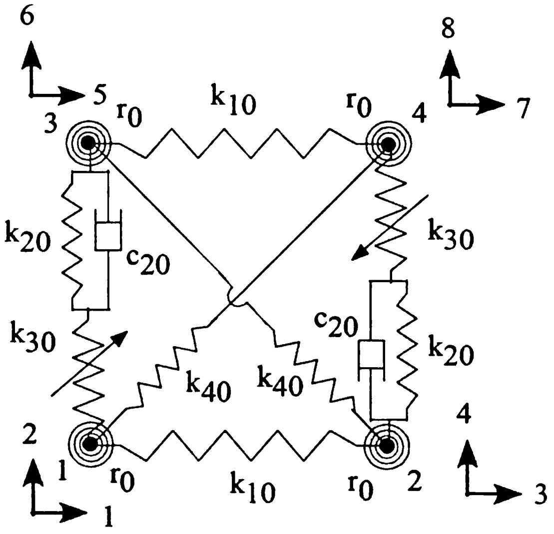

Figure 2.22. Two-dimensional lattice of phase B

The complex stiffness of each of the two identical standard linear solid elements forming the left and right sides of the lattice is given by

$$s_1(\omega) = \frac{k_{30}(k_{20} + i\omega c_{20})}{k_{30} + k_{20} + i\omega c_{20}} \tag{2.7.1}$$

The complex stiffness matrix (K_B^*) for the 2D element in Fig. 2.22 is given by

$$K_B^* = \begin{bmatrix} k_{10}+\frac{k_{40}}{2}+R & \frac{k_{40}}{2} & -k_{10} & 0 & -R & 0 & -\frac{k_{40}}{2} & -\frac{k_{40}}{2} \\ \frac{k_{40}}{2} & s_1+\frac{k_{40}}{2}+R & 0 & -R & 0 & -s_1 & -\frac{k_{40}}{2} & -\frac{k_{40}}{2} \\ -k_{10} & 0 & k_{10}+\frac{k_{40}}{2}+R & -\frac{k_{40}}{2} & -\frac{k_{40}}{2} & \frac{k_{40}}{2} & -R & 0 \\ 0 & -R & -\frac{k_{40}}{2} & s_1+\frac{k_{40}}{2}+R & \frac{k_{40}}{2} & -\frac{k_{40}}{2} & 0 & -s_1 \\ -R & 0 & -\frac{k_{40}}{2} & \frac{k_{40}}{2} & k_{10}+\frac{k_{40}}{2}+R & -\frac{k_{40}}{2} & -k_{10} & 0 \\ 0 & -s_1 & \frac{k_{40}}{2} & -\frac{k_{40}}{2} & -\frac{k_{40}}{2} & s_1+\frac{k_{40}}{2}+R & 0 & -R \\ -\frac{k_{40}}{2} & -\frac{k_{40}}{2} & -R & 0 & -k_{10} & 0 & k_{10}+\frac{k_{40}}{2}+R & \frac{k_{40}}{2} \\ -\frac{k_{40}}{2} & -\frac{k_{40}}{2} & 0 & -s_1 & 0 & -R & \frac{k_{40}}{2} & s_1+\frac{k_{40}}{2}+R \end{bmatrix} \tag{2.7.2}$$

where

$$R = \frac{2r_0}{L^2}$$

L is length of the side of the square lattice and r_0 is the angular stiffness of the rotational springs at the four corners (as shown in Fig. 2.22).

The complex modulus tensor (C_B) corresponding to the lumped lattice in Fig. 4.2 is of the form:

$$C_B = \begin{bmatrix} f_{11} & f_{12} & 0 \\ f_{12} & f_{22} & 0 \\ 0 & 0 & f_{33} \end{bmatrix} \tag{2.7.3}$$

Four numerical tests are conducted to find C_B:

(i) Tensile test 1: Degrees of freedom 1, 2, 4, 5, 6 and 8 are constrained (zero prescribed displacement) and degrees of freedom 3 and 7 are given unit displacements. f_{11} is the total reaction force along the degrees of freedom 3 and 7. f_{11} is given by

$$f_{11} = 2k_{10} + k_{40} \tag{2.7.4}$$

(ii) Tensile test 2: Degrees of freedom 1, 2, 3, 4, 5 and 7 are constrained (zero prescribed displacement) and degrees of freedom 6 and 8 are given unit displacements. f_{22} is the total reaction force along the degrees of freedom 6 and 8. f_{22} is given by

$$f_{22} = 2s_1 + k_{40} \tag{2.7.5}$$

(iii) Tensile test 3: Degree of freedoms 1, 2, 3, 4, 5 and 7 are constrained (zero prescribed displacement) and degrees of freedom 6 and 8 are given unit displacements. f_{12} is the total reaction force along the degrees of freedom 1 and 4. f_{12} is given by

$$f_{12} = k_{40} \tag{2.7.6}$$

(iv) Shear test: Degree of freedoms 1, 2, 3, 4, 6 and 8 are constrained (zero prescribed displacement) and degrees of freedom 5 and 7 are given unit displacements. f_{33} is the total reaction force along the degrees of freedom 5 and 7. f_{33} is given by

$$f_{33} = k_{40} + 2R \tag{2.7.7}$$

2.7.1 Stability of the lumped system

The stability of the inclusions of material B is tested here. Let us consider a 5x5 tiled arrangement of the lumped lattice of Fig. 4.2 as an inclusion in the matrix of material A, as shown in Fig. 2.23. The nodes are shown in the figure as small circles and a few of them are numbered. The nodes of the lumped system at the phase interface (e.g. nodes 1, 2, 3, 4, 5, 6, 7, 12, etc.) are fixed to material A. We will test whether the lumped system is stable as an inclusion. In particular we will determine whether displacements of the interior nodes of the lumped system are bounded if motion of the nodes at the phase interface is bounded.

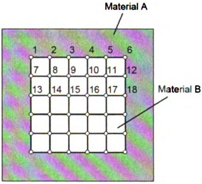

Figure 2.23 Inclusion of material B in matrix of material A

Let us consider the top left lattice in the lumped system separately. The four nodes corresponding to this lattice are numbered 7, 8, 1 and 2. As indicated in Fig. 2.24, the corresponding degrees of freedom are 1 and 2; 3 and 4; 5 and 6; and 7 and 8, respectively. Nodes 1, 2 and 7 are fixed, i.e., degrees of freedom 1, 2, 5, 6, 7 and 8 (Fig. 2.24) are fixed.

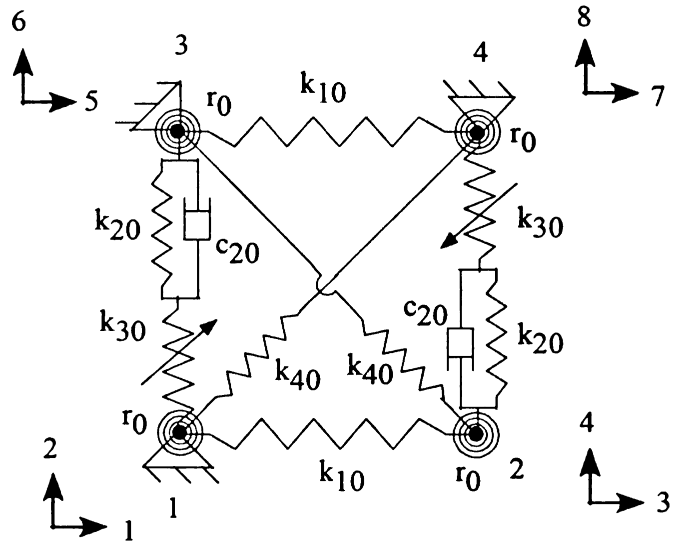

Figure 2.24. A lattice of material B with three nodes fixed

While the other three nodes fixed, node 8 is free to move along degrees of freedom 3 and 4. Assume that a small disturbance force acts on node 8. If x_3 and x_4 are the resulting static displacements along degrees of freedom 3 and 4, respectively, then the corresponding strain energy is

$$\Phi = \frac{1}{2}\mathbf{X}^T\mathbf{K}\mathbf{X} \tag{2.7.8}$$

where

$$\mathbf{K} = \begin{bmatrix} k_{10} + \frac{k_{40}}{2} + R & \frac{k_{40}}{2} \\ \frac{k_{40}}{2} & \frac{k_{20}k_{30}}{k_{20} + k_{30}} + \frac{k_{40}}{2} + R \end{bmatrix} \qquad (2.7.9)$$

$$\mathbf{X} = \begin{Bmatrix} x_3 \\ x_4 \end{Bmatrix} \qquad (2.7.10)$$

Under the given boundary conditions, displacements x_3 and x_4 (at node 8) are bounded if stiffness matrix K is positive definite. The positive definiteness of K insures that displacements at the other interior nodes (such as 9, 10, 11, 14, 15 etc.) are also bounded. With K positive definite, the lumped system is stable as an inclusion because under infinitesimal displacements at the phase interface, displacements at the interior nodes are unique and bounded.

2.7.2 Example of phase B

The following parameters may be used to obtain phase B approximately the same as that used in section 2.6:

$$k_{20} = 1.672 E_A$$

$$k_{30} = -0.304 k_{20}$$

$$c_{20} / k_{20} = 0.0002$$

$$k_{10} = k_{40} = 0.57 E_A$$

These values of k_{20}, k_{30} and c_{20} correspond to

$$s_1(\omega) = -\frac{0.5083(1+i0.0002\omega)}{0.696+i0.0002\omega}E_A$$

and therefore,

$$s_1(0) = -0.73E_A$$

These parameters suggest that, for stability,

$$R > 0.505E_A$$

We select $R = k_{10} = 0.57E_A$ to maintain stability.

The corresponding elastic tensor is given by

$$C_B = \begin{bmatrix} 2k_{10}+k_{40} & k_{40} & 0 \\ k_{40} & 2s_1+k_{40} & 0 \\ 0 & 0 & k_{40}+2R \end{bmatrix}$$

or

$$C_B = \begin{bmatrix} 1.71 & 0.57 & 0 \\ 0.57 & -\frac{1.0166(1+i0.0002\omega)}{0.696+i0.0002\omega}+0.57 & 0 \\ 0 & 0 & 1.71 \end{bmatrix} E_A \tag{2.7.11}$$

2.8 Realization of Phase B Using Tileable Bistable Structure

One way to realize the lumped systems for phase B_1 (given in section 2.6) or B is to use tileable bistable structure (described in chapter 5). Recall that material B_1 is the negative stiffness material and is one of the two component phases of the rank-1 layered material

B. As an example, Fig. 2.25 shows geometric realization of material B_1 as a periodic structure. The rectangular solid structures shown in the figure are made of a Kelvin-Voigt viscoelastic material. These structures connect 2D bistable structures with each other. The fundamental cell of the periodic arrangement shown in the figure is the dashed square region in the figure. This fundamental cell is equivalent to the 2D lattice shown in Fig. 2.22. Chapter 5 will describe the tileable bistable structures that can be used as building blocks of material B_1 or B.

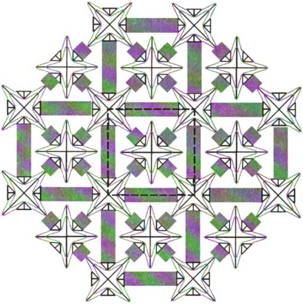

Figure 2.25. Material B as a periodic structure

CHAPTER 3

EXAMPLES ILLUSTRATING MATERIAL SOFTENING AND IMPROVED VIBRATION ISOLATION

The aim of the present chapter is to illustrate frequency-induced softening of a two-phase composite and the corresponding improvement in the vibration isolation properties. Four examples are presented to illustrate frequency-induced softening. The composite material designed in the first example is illustrated to improve vibration isolation properties as compared to the typical matrix material A. In particular, the transmissibility of an engine mount made of the designed composite material is shown to be less than that of an engine mount made of material A only. Before the examples are presented, the chapter introduces to the method used to compute the average (or homogenized) viscoelastic properties of a composite material. In the first three examples, the inclusion material B is a rank 1 layered material (as introduced in the previous chapter) composed of alternating layer of the example lumped material B_1 in section 2.6 and the matrix phase A used in that example. The three examples differ only in the matrix phase A used. A typical rubber material (having a constant complex modulus) is used as a matrix material A in the first example, whereas material A is purely elastic in example 2. In example 3, material A is a Kelvin-Voigt viscoelastic material (i.e. imaginary part of the complex modulus increases proportional to the forcing frequency). In example 4, the lumped system developed in section 2.7 is used as phase B. In all the examples, the designed composite material exhibits softening. While in the third example the material first softens and then hardens with the frequency, in the other examples the softening is monotonous with respect to the forcing frequency.

3.1 Homogenization of Viscoelastic Properties

With phases A and B in hand, the final step is to compute the effective properties of the mixture of A and B, e.g., characterized by a simple arrangement such as that in Fig. 3.1. This can be accomplished by numerical homogenization (notice that this suggests that the mixture of constituents B_1 and B_2 takes place at a smaller scale than the mixture of A and B). The representative cell is discretized using standard, 2D quadrilateral finite elements and the effective properties of the mixture are obtained by exposing the cell to three states of (unit) pre-strain, as is standard in numerical homogenization methods (details can be found in Yi et. al. (1998)). The computed homogenized elastic tensor of the composite material has the information of whether the composite material softens with frequency. In particular, a monotonic decrease in the absolute value of the second diagonal entry of the effective tensor indicates softening of the composite material in direction 2.

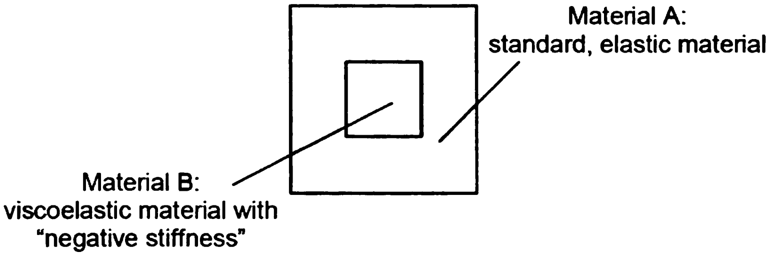

Figure 3.1. Representative cell characterizing the (periodic) mixture of materials A and B

3.2 Example 1

Here the material softening and the improved vibration isolation properties are illustrated with a numerical example. A typical rubber-like viscoelastic material is selected first for phases A and B_2. The (complex) elastic tensor of phase A is

$$C_A = C_A^0(1+i\delta_A) \quad \text{with } C_A^0 = \frac{E_A}{1-\nu_A^2}\begin{bmatrix} 1 & \nu_A & 0 \\ \nu_A & 1 & 0 \\ 0 & 0 & (1-\nu_A)/2 \end{bmatrix}$$

where Young's modulus E_A is arbitrary but real and positive and Poisson's ratio $\nu_A = 0.45$. The structural damping coefficient δ_A is 0.07. As indicated before, this material is used also in phase B_2 of B, i.e., $C_{B2} = C_A$.

Phase B is a rank-1 layered material. Here phase B is constructed by alternating layers of phase B_2 and a negative-stiffness phase B_1. The volume fraction of B_2 in B is 0.8.

Phase B_1 is made of a material such as the lumped lattice (Fig. 2.20). Its elastic tensor is as in (2.6.8), i.e.

$$C_{B1} = \frac{E_{B1}^*}{1-\nu_{B1}^2}\begin{bmatrix} 1 & \nu_{B1} & 0 \\ \nu_{B1} & 1 & 0 \\ 0 & 0 & (1-\nu_{B1})/2 \end{bmatrix}$$

with $\nu_{B1} = 1/3$ and

$$E_{B1}^{*} = -\frac{6.8501(1+i0.0002\omega)}{0.696+i0.0002\omega} E_A$$

The values of E_{B1}^{*} and ν_{B1} used here correspond to the example material B_1 computed in section 2.6.

The final mixture corresponds to the periodic mixture of phases A and B characterized by the periodic repetition of the cell in Fig. 3.1. The volume fraction of phase B is 16%. The unit cell is discretized into 50x50 square plane stress elements for numerical analysis. The resulting homogenized complex modulus tensor of the two-dimensional composite is given by

$$C_H^{*} = \begin{bmatrix} c_{11}(\omega) & c_{12}(\omega) & 0 \\ c_{12}(\omega) & c_{22}(\omega) & 0 \\ 0 & 0 & c_{33}(\omega) \end{bmatrix}$$

The absolute values, real and imaginary parts of $c_{ij}(\omega)$ are plotted versus the forcing frequency in Fig. 3.2. $c_{ij}(\omega)$ values are normalized by E_A.

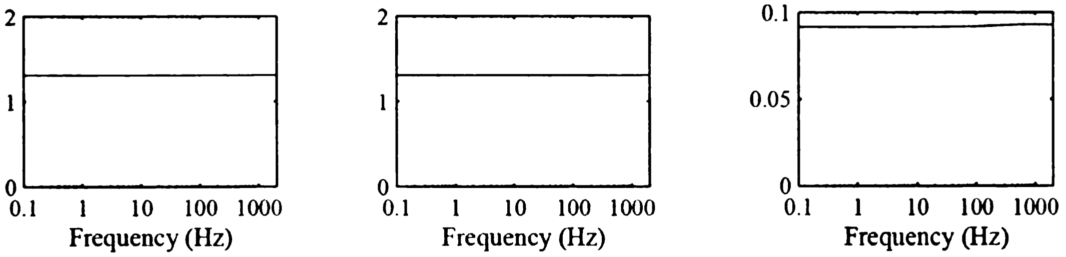

$\|c_{11}/E_A\|$ Re(c_{11}/E_A) Im(c_{11}/E_A)

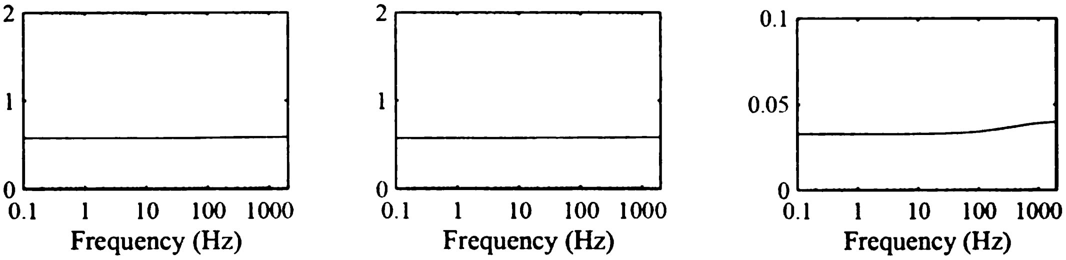

$\|c_{12}/E_A\|$ Re(c_{12}/E_A) Im(c_{12}/E_A)

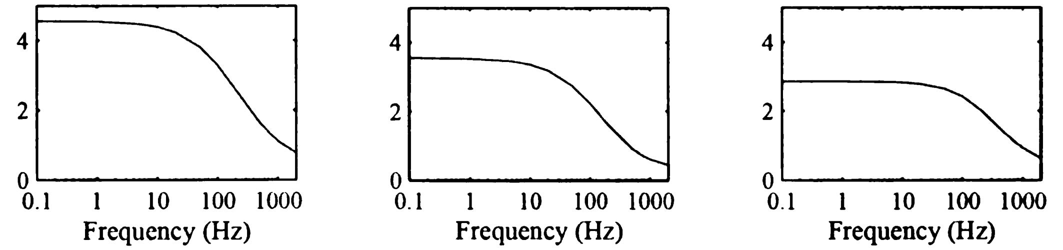

$\|c_{22}/E_A\|$ Re(c_{22}/E_A) Im(c_{22}/E_A)

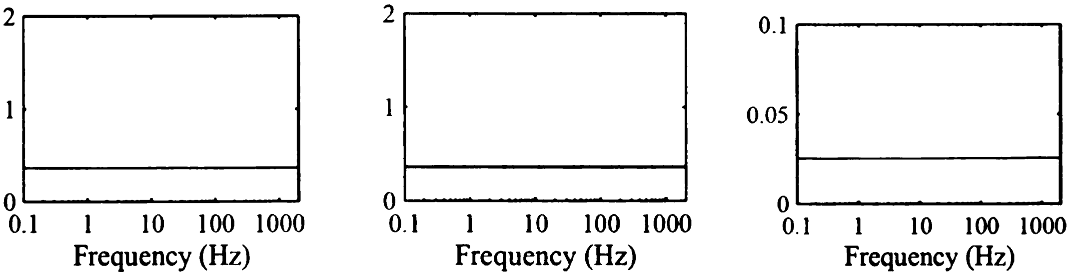

$\|c_{33}/E_A\|$ Re(c_{33}/E_A) Im(c_{33}/E_A)

Figure 3.2. Components of the effective elastic tensor after mixing A and B

As can be seen in Fig. 3.2, $\|c_{22}(\omega)\|$ decreases with forcing frequency, while $\|c_{11}(\omega)\|$, $\|c_{12}(\omega)\|$ and $\|c_{33}(\omega)\|$ are almost constant. This implies that frequency-induced softening is achieved if the composite material is loaded in direction 2 while the material is constrained in direction 1. Direction 1 is along the thickness of the layers (of phase B_1 or B_2) inside phase B, as shown in Fig. 3.3. Frequency-induced softening of the dynamic modulus is achieved under unidirectional loading – when the composite material is loaded in direction 2.

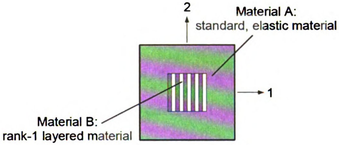

Figure 3.3. Phase B as layered material

3.2.1 Transmissibility analysis

Now the vibration isolation performance of the material designed in this example will be demonstrated. A cylindrical block of the composite material synthesized is used here as an engine mount and a transmissibility analysis is carried out. Figure 3.4 shows the engine mount system, where l is the length of the engine mount. The area of cross-section of the cylindrical engine mount is a (i.e. the radius of the cylinder is $\sqrt{a/\pi}$). The engine mount supports an engine of mass m and the unbalanced disturbance force acting on the mass is F. F_s is the force transmitted to the automobile structure. The transmissibility of the system is $T = \|F_s\| / \|F\|$. An effective vibration isolation performance corresponds to a low transmissibility.

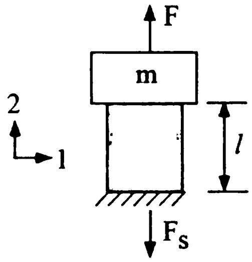

Figure 3.4. Engine mount system

The components of the elastic tensor of the composite material used to build the mount are those plotted in Fig. 3.2. In Fig. 3.4, the engine mount is unidirectionally loaded in direction 2 and not constrained in the direction 1. As indicated earlier in this section, direction 2 is perpendicular to the layering direction, as shown in Fig. 3.3. Under the given boundary condition the strain (ε_{22}) and the stress (σ_{22}) in direction 2 are related as:

$$\sigma_{22} = E_C(\omega)\varepsilon_{22}$$

where

$$E_C(\omega) = c_{22}(\omega) - \nu(\omega)c_{12}(\omega)$$

and

$$\nu(\omega) = \frac{c_{12}(\omega)}{c_{11}(\omega)}$$

$E_C(\omega)$ and the effective stiffness of the engine mount $k_C(\omega)$ are related by

$$k_C(\omega) = \frac{E_C(\omega)a}{l}$$

The absolute value, real and imaginary parts of $E_C(\omega)$ are plotted in Fig. 3.5, where values are normalized by E_A (i.e., the Young's modulus of phase A). It can be seen in the figure that $\mathrm{Re}\left(E_C(0)\right)$ is approximately $3E_A$. In other words, the effective Young's modulus of the composite material is $3E_A$. Typically, the static stiffness (i.e., $k_C(0)$) of the engine mount is prescribed. In this case, suppose $k_C(0)$ is set to 170 N/mm. This stiffness is achieved with, for example, $E_A = 4$ N/mm^2, $l = 30$ mm and $a = 425$ mm^2.

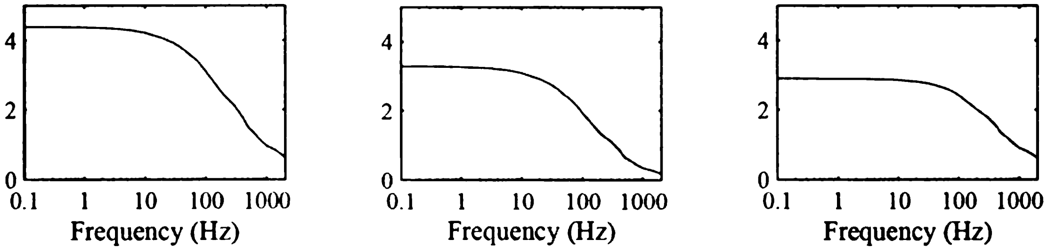

$\left\| E_C(\omega)/E_A \right\|$ $\mathrm{Re}(E_C(\omega)/E_A)$ $\mathrm{Im}(E_C(\omega)/E_A)$

Figure 3.5. The effective complex modulus $E_C(\omega)$

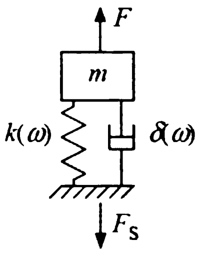

Figure 3.6. Engine mount as spring-damper system

The engine mount in Fig. 3.4 may be represented as a system of a spring and a damper connected in parallel, as shown in Fig. 3.6. The corresponding spring stiffness ($k(\omega)$) and the structural damping coefficient ($\delta(\omega)$) are

$$k(\omega) = \mathrm{Re}(k_C(\omega))$$

$$\delta(\omega) = \frac{\mathrm{Im}(k_C(\omega))}{\mathrm{Re}(k_C(\omega))}$$

$k(\omega)$ and $\delta(\omega)$ are plotted in Fig. 3.7.

Note that the complex stiffness of the engine mount is $k_C(\omega)$, which is directly proportional to the complex modulus $E_C(\omega)$. As can be seen in Fig. 3.5, the absolute value, real and imaginary parts of $E_C(\omega)$ decrease monotonically with frequency. This implies that the dynamic stiffness of the engine mount $\|k_C(\omega)\|$, the real and imaginary parts of the complex stiffness (i.e. $k(\omega)$ and $\delta(\omega)k(\omega)$, respectively) also decrease monotonically with frequency. However, the effective structural damping coefficient $\delta(\omega)$ increases with frequency as shown in Fig. 3.7. The dashed lines in Fig. 3.7 correspond to $k(\omega)$ and $\delta(\omega)$ of the engine mount if the mount were made of phase A alone.

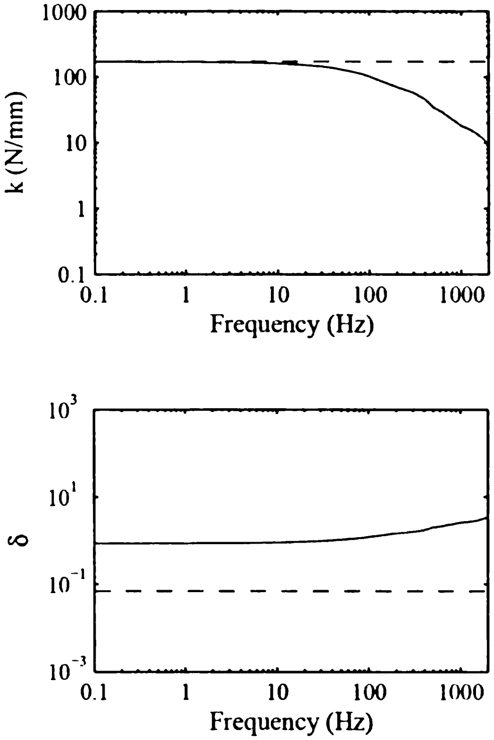

Figure 3.7. Spring stiffness ($k(\omega)$) and damping coefficient ($\delta(\omega)$) of the engine mount

With $k(\omega)$ and $\delta(\omega)$ in hand, the next step is to compute the transmissibility of the engine mount, defined here as

$$T(\omega) = \left\| \frac{F_S}{F} \right\| = \left\| \frac{1 + i\delta(\omega)}{1 - m\omega^2 / k(\omega) + i\delta(\omega)} \right\|$$

Note that the above expression for $T(\omega)$ may not be ideal for a nonlinear system where $k(\omega)$ and $\delta(\omega)$ are functions of frequency; however, this expression is used for simplicity as is standard in engineering practice.

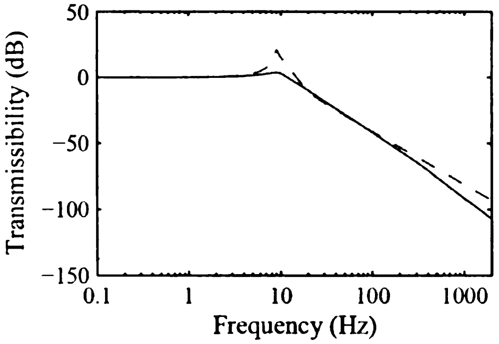

Figure 3.8. Transmissibility as a function of frequency

The transmissibility $T(\omega)$ is plotted in Fig. 3.8 (measured in decibels). The solid line corresponds to the composite material, while the dashed line corresponds to phase A alone. As can be seen in the figure, at high frequencies the transmissibility of the composite material is significantly less than that of phase A alone. Thus the composite material synthesized in this example performs better than a typical rubber material (phase A).

3.3. Example 2

In this example, material A is purely elastic. The elastic tensor for material A is given by

$$C_A = \frac{E_A}{1-\nu_A^2}\begin{bmatrix} 1 & \nu_A & 0 \\ \nu_A & 1 & 0 \\ 0 & 0 & (1-\nu_A)/2 \end{bmatrix} \tag{3.3.1}$$

where $\nu_A = 0.3$ is the prescribed Poisson's ratio for phase A and E_A is the Young's Modulus of material A.

As in example 1, material B here is rank-1 layered material, whose constituent materials are an elastic material A and a negative-stiffness material B_1. Material B_1 used here is the same as that used in Example 1. The elastic tensor for the rank-1 layered material B is same as that in section 2.6.

We consider the periodic mixture of materials A and B characterized by the periodic repetition of the cell shown in Fig. 3.1. The volume fraction of the phase B is 16%. The discretization of the unit cell is the same as in Example 1. The non-zero terms of the resulting effective complex modulus are plotted in Fig. 3.9. As before, $c_{ij}(\omega)$ values are normalized by E_A. As can be seen in Fig. 3.9, $\|c_{22}(\omega)\|$ decreases with forcing frequency, while $\|c_{12}(\omega)\|$ increases with frequency. $\|c_{11}(\omega)\|$ and $\|c_{33}(\omega)\|$ are approximately constant.

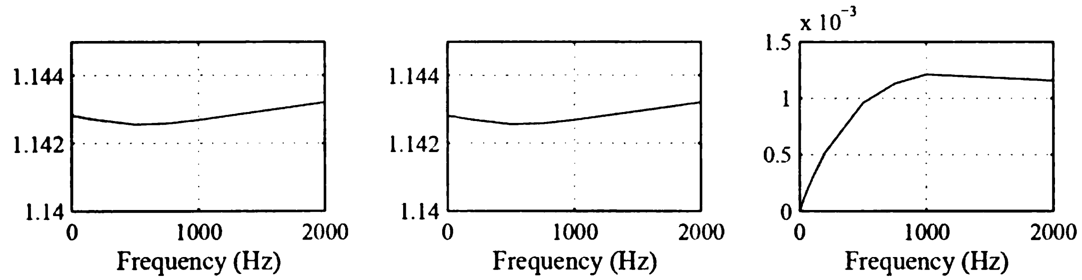

(a) $\|c_{11}/E_A\|$ (b) $\mathrm{Re}(c_{11}/E_A)$ (c) $\mathrm{Im}(c_{11}/E_A)$

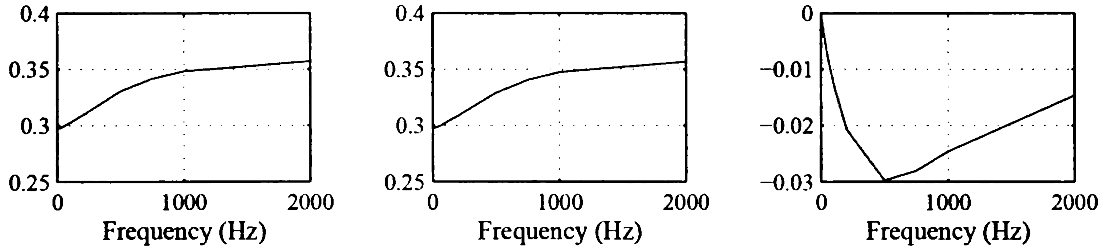

(d) $\|c_{12}/E_A\|$ (e) $\mathrm{Re}(c_{12}/E_A)$ (f) $\mathrm{Im}(c_{12}/E_A)$

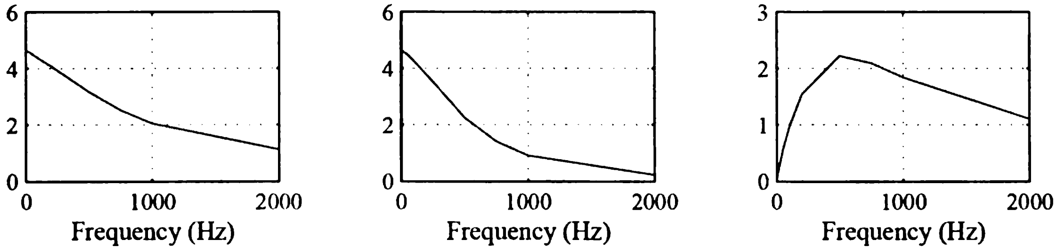

(g) $\|c_{22}/E_A\|$ (h) $\mathrm{Re}(c_{22}/E_A)$ (i) $\mathrm{Im}(c_{22}/E_A)$

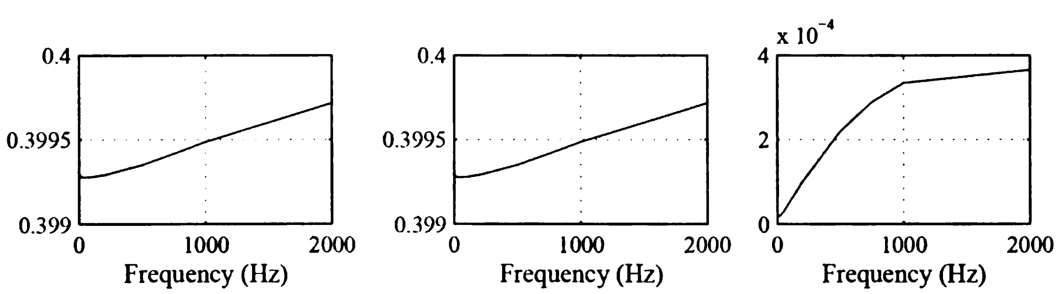

(j) $\|c_{33}/E_A\|$ (k) $\mathrm{Re}(c_{33}/E_A)$ (l) $\mathrm{Im}(c_{33}/E_A)$

Figure 3.9. Components of the effective elastic tensor mixing materials A and B in Example 2

3.4. Example 3

The purpose of this example is to study the effects of introducing damping in material A. Here the unit cell and its discretization are kept as that in Example 2. However material A here is a Kelvin-Voigt viscoelastic material with damping coefficient 0.0002. The elastic tensor of material A is

$$C_A = \frac{E_A^*}{1-\nu_A^2}\begin{bmatrix} 1 & \nu_A & 0 \\ \nu_A & 1 & 0 \\ 0 & 0 & (1-\nu_A)/2 \end{bmatrix} \tag{3.4.1}$$

where $E_A^* = E_A(1+i0.0002\omega)$ and $\nu_A = 0.3$. E_A is the Young's Modulus of material A.

As in Example 2, material B is a rank-1 layered material whose constituent materials are materials A and B_1. Material B_1 here is same as that in Example 1. Unlike Example 2, material B has Kelvin-Voigt viscoelastic material A as a constituent and therefore material B here is different from that in Examples 1 and 2. The volume fraction of material A in the rank-1 layered material B is again 0.8, the same value in Examples 1 and 2. Entries in elasticity tensor of material B are plotted in Fig. 3.10.

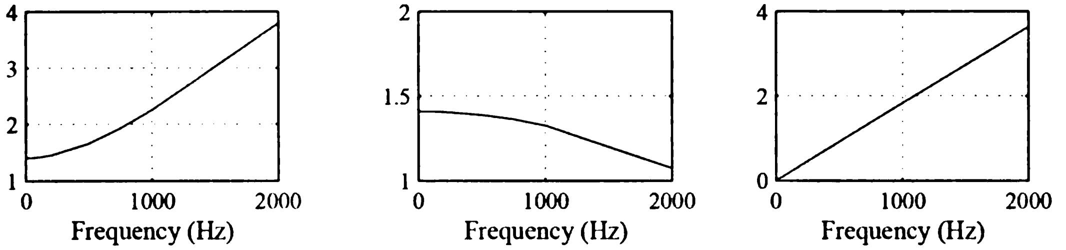

(a) $||b_{11}/E_A||$ (b) $\mathrm{Re}(b_{11}/E_A)$ (c) $\mathrm{Im}(b_{11}/E_A)$

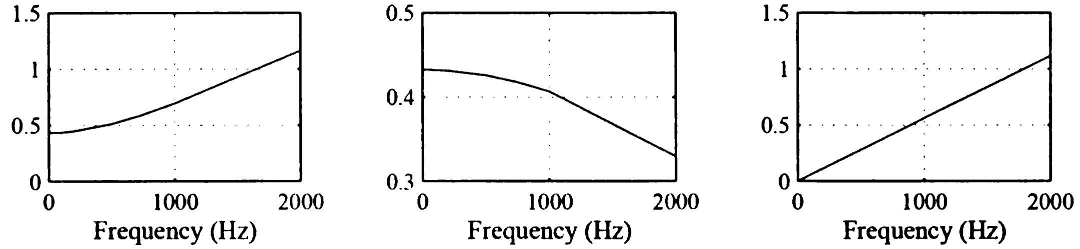

(d) $||b_{12}/E_A||$ (e) $\mathrm{Re}(b_{12}/E_A)$ (f) $\mathrm{Im}(b_{12}/E_A)$

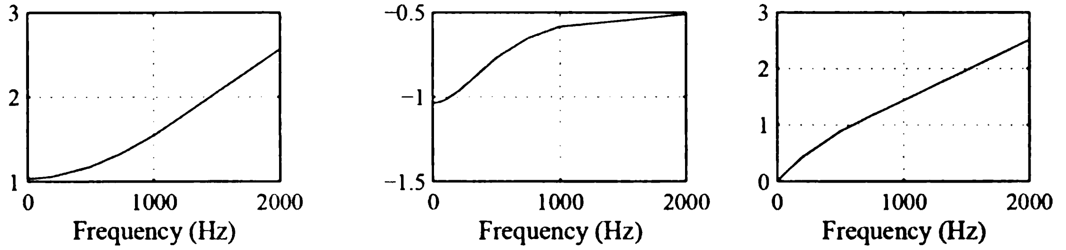

(g) $||b_{22}/E_A||$ (h) $\mathrm{Re}(b_{22}/E_A)$ (i) $\mathrm{Im}(b_{22}/E_A)$

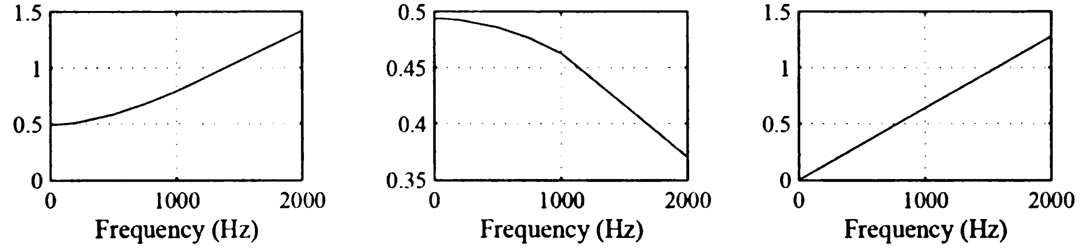

(j) $||b_{33}/E_A||$ (k) $\mathrm{Re}(b_{33}/E_A)$ (l) $\mathrm{Im}(b_{33}/E_A)$

Figure 3.10. Components of the effective elastic tensor of material B in Example 3

In Fig. 3.10, we observe that while the real parts of $b_{ij}(\omega)$ are of the same order of those in section 2.6 (also used in example 2), the imaginary parts of $b_{ij}(\omega)$ are considerably larger (since A is now a Kelvin-Voigt viscoelastic material).

Entries in the effective complex modulus tensor of the resulting composite material (mixing A and B) are plotted versus the forcing frequency in Fig. 3.11. In Fig. 3.11, we notice that $c_{ij}(\omega)$ here are, in general, considerably different from that in examples 1 and 2. As expected, the imaginary parts of $c_{ij}(\omega)$ are significantly higher than that in example 1 and 2 as a result of frequency proportional damping in material A.

We also notice that $\|c_{11}(\omega)\|$, $\|c_{12}(\omega)\|$ and $\|c_{33}(\omega)\|$ are monotonically increasing, while $\|c_{22}(\omega)\|$ first decreases with the increase of the forcing frequency until about 500 Hz, after which it increases. This composite material may still be used as an engine mount showing frequency-induced softening, since the frequency of vibration in automobile is typically less than 500 Hz. Moreover, by reducing the structural damping coefficient of material A, the maximum frequency showing the softening can be increased.

Also notice that $\|c_{22}(\omega)\|$ at 2000Hz is less than that at 0Hz. The drop in $\|c_{22}(\omega)\|$ in the frequency range 0-500 Hz is significantly more than the increase in $\|c_{22}(\omega)\|$ in the 500-2000Hz frequency range. Thus the average dynamic modulus over the given frequency range 0-2000Hz is still considerably less than the static modulus.

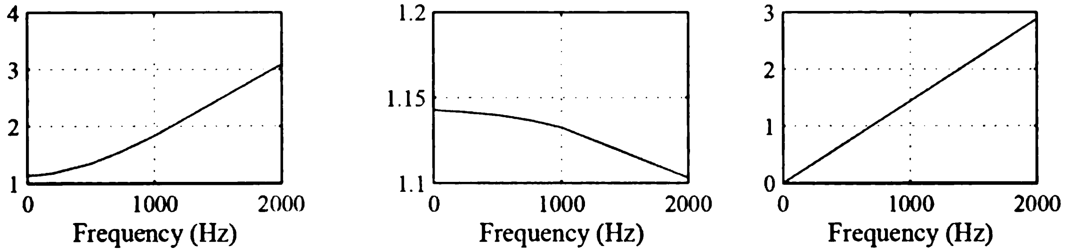

(a) $\|c_{11}/E_A\|$ (b) $\mathrm{Re}(c_{11}/E_A)$ (c) $\mathrm{Im}(c_{11}/E_A)$

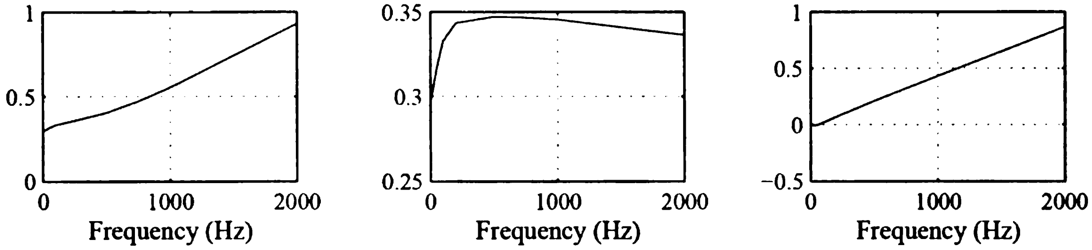

(d) $\|c_{12}/E_A\|$ (e) $\mathrm{Re}(c_{12}/E_A)$ (f) $\mathrm{Im}(c_{12}/E_A)$

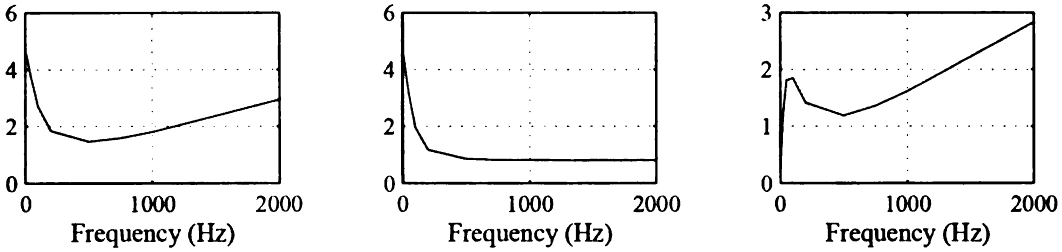

(g) $\|c_{22}/E_A\|$ (h) $\mathrm{Re}(c_{22}/E_A)$ (i) $\mathrm{Im}(c_{22}/E_A)$

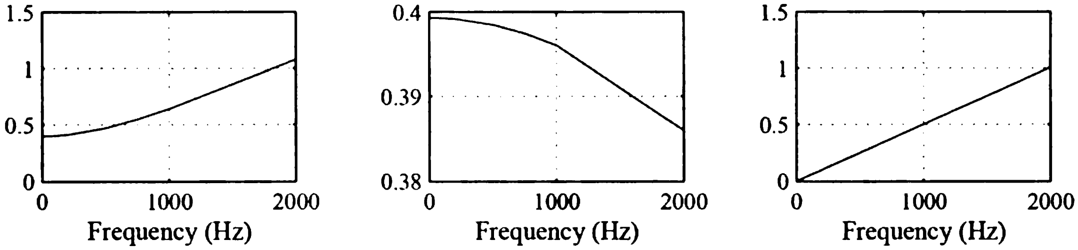

(j) $\|c_{33}/E_A\|$ (k) $\mathrm{Re}(c_{33}/E_A)$ (l) $\mathrm{Im}(c_{33}/E_A)$

Figure 3.11. Components of the effective elastic tensor mixing materials A and B in Example 3

3.5. Example 4

In this example we will test whether the lumped system for phase B given in section 2.7 leads to frequency-induced softening. We will use the simple topology of the fundamental cell used in the previous three examples and shown again in Fig. 3.12. The volume fraction of phase B in the fundamental cell is now 10.24%.

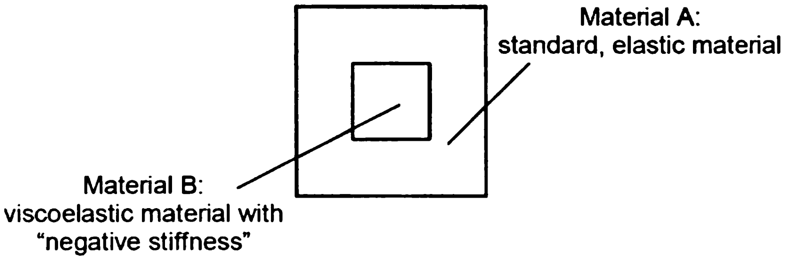

Figure 3.12. A simple square fundamental cell having square inclusion of phase B in the matrix of phase A

Phase A is same as that used in example 1, i.e. the elastic tensor of phase A is

$$C_A = C_A^0(1+i\delta_A) \quad \text{with} \quad C_A^0 = \frac{E_A}{1-\nu_A^2}\begin{bmatrix} 1 & \nu_A & 0 \\ \nu_A & 1 & 0 \\ 0 & 0 & (1-\nu_A)/2 \end{bmatrix}$$

where Young's modulus E_A is arbitrary but real and positive and Poisson's ratio $\nu_A = 0.45$. The structural damping coefficient δ_A is 0.07.

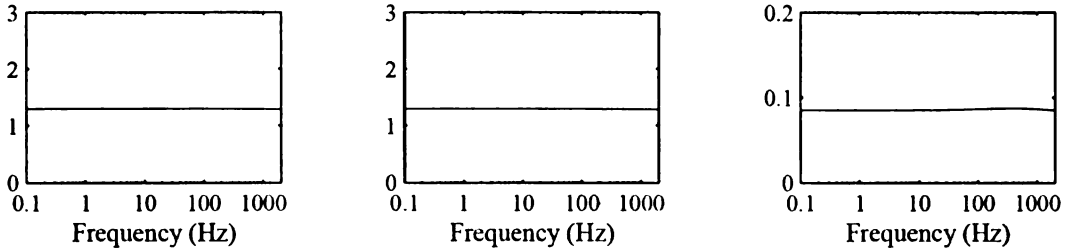

(a) $\|c_{11}/E_A\|$ (b) $\mathrm{Re}(c_{11}/E_A)$ (c) $\mathrm{Im}(c_{11}/E_A)$

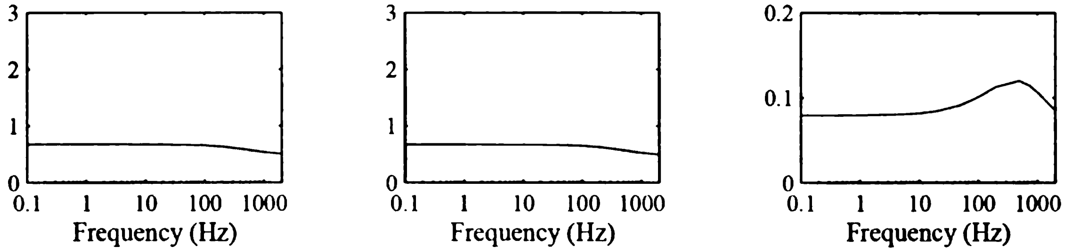

(d) $\|c_{12}/E_A\|$ (e) $\mathrm{Re}(c_{12}/E_A)$ (f) $\mathrm{Im}(c_{12}/E_A)$

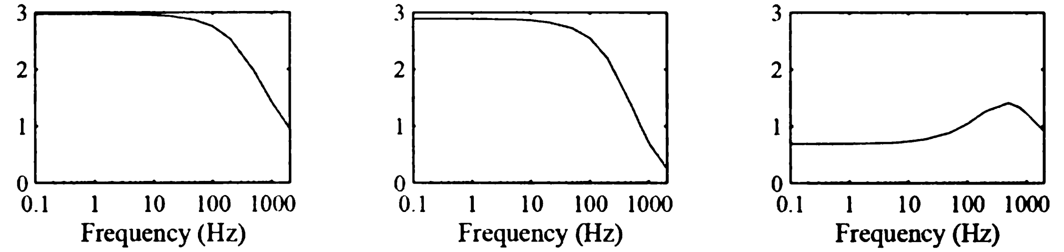

(g) $\|c_{22}/E_A\|$ (h) $\mathrm{Re}(c_{22}/E_A)$ (i) $\mathrm{Im}(c_{22}/E_A)$

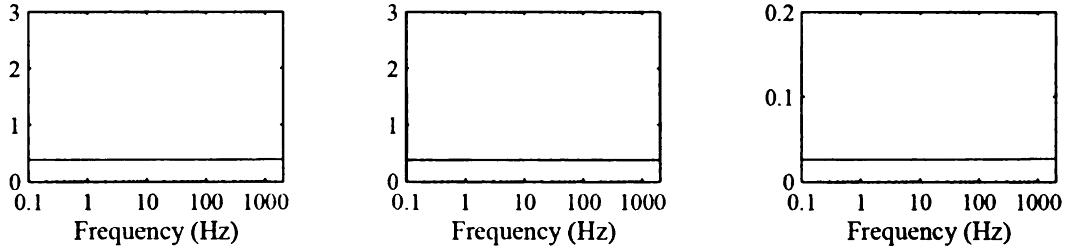

(j) $\|c_{33}/E_A\|$ (k) $\mathrm{Re}(c_{33}/E_A)$ (l) $\mathrm{Im}(c_{33}/E_A)$

Figure 3.13. Plot of the entries of C_H^* for example 4

The average elastic tensor (C_H^*) is computed using the numerical homogenization method after discretizing the fundamental cell into 50x50 elements. C_H^* is given by

$$C_H^* = \begin{bmatrix} c_{11}(\omega) & c_{12}(\omega) & 0 \\ c_{12}(\omega) & c_{22}(\omega) & 0 \\ 0 & 0 & c_{33}(\omega) \end{bmatrix}$$

The absolute values, real parts and imaginary parts of the entries of C_H^* are plotted in Fig. 3.13. As shown in Fig. 3.13(g), $\|c_{22}\|$ decreases with frequency and thus we see that the composite material softens in direction 2.

Transmissibility analysis is carried out for the material designed here using the procedure followed in section 3.2.1. The corresponding transmissibility plot is given in Fig. 3.14. The dashed line in the figure corresponds to material A, while the solid line corresponds to the composite material. As can be seen in the figure, transmissibility for the composite material is better than that for the typical rubber-like material A.

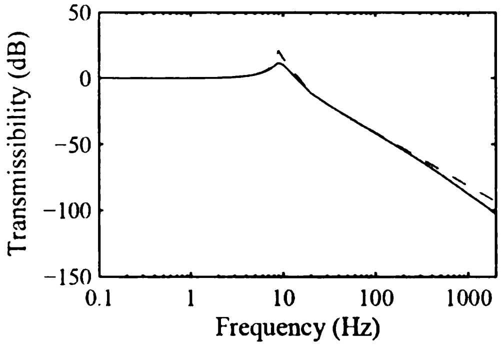

Figure 3.14. Transmissibility of the composite (solid line) as compared to phase A (dashed line) for example 4

CHAPTER 4

TOPOLOGY OPTIMIZATION OF THE COMPOSITE

As seen in chapter 3, inclusions of the negative stiffness phase in the matrix of a typical elastic/viscoelastic material phase lead to a composite material exhibiting frequency-induced softening. The fundamental cell used in that section has very simple topology, where the inclusion is square-shaped. This simple topology shows softening in only one direction. When softening in the other entries of the elastic tensor is required, then it may be difficult to easily find the corresponding topology. To achieve softening in any prescribed direction, one option is to use topology optimization to design the composite. In this chapter, the material distribution in the fundamental cell is optimized to obtain a prescribed elastic tensor that exhibits softening. The objective function to be minimized is the least-square error between the actual elastic tensor of the designed composite and a prescribed elastic tensor. The stability of the composite is ensured by a constraint that maintains positive definiteness. The design methodology starts with discretization of a two-dimensional design domain into a number of finite elements. An element is made of a mixture of a typical rubber material A and a negative stiffness material B; however, in the final topology (i.e., the result of the optimization) it is desirable that all elements are made purely of either material A or B. Material B used here is the lumped system built in section 2.7 (and used in example 4 of chapter 3, i.e., section 3.5). The volume fraction of material A in every element is treated as a design variable. Material B is anisotropic and has negative stiffness in only one entry of its elastic tensor. So that the negative stiffness of material B can be made available in any desired direction within an element, the angle of orientation of material B in every element is also treated as a design variable. There are upper and lower bounds on the total volume fraction of A in the unit cell. A gradient-based optimization method (viz. the method of moving asymptotes) is used to solve the problem. There are three problems solved and the resulting geometries of the base cell are shown in sections 4.5.1-4.5.3.

4.1 Background

The problem of material design by topology optimization, which is also referred to as 'inverse homogenization problem', was introduced by Sigmund (1994 and 1995). The aim is to design the microstructure of a two-phase composite material that has prescribed effective elastic properties. The materials designed by the author are periodic, i.e., the materials are made by end-to-end periodic repetition (tiling) of a base or fundamental cell. Homogenization methods to find effective properties of a periodic material are well-known, e.g., in Bensoussan et al (1978) and Guedes and Kikuchi (1990), where the effective properties are determined solely by analyzing the fundamental cell. Sigmund extends the periodic homogenization to an inverse problem where the homogenized properties are given and the goal is to find the material distribution. The inverse homogenization problem has been used to design materials with unusual or etxremal properties such as materials with zero or negative Poisson's ratio as in Sigmund (1995) and materials having extremal bulk modulus as in Sigmund (2000), where an extremal elastic property refers to the maximum or minimum value allowed by the theoretical bounds (such as Hashin-Shtrikman and Cherkaev-Gibiansky bounds) on a composite's elastic properties.

Diaz and Benard (2003) extend Sigmund's work by using a polygonal fundamental cell and produced a material distribution that may not be obtained using a simple square or rectangular fundamental cell. The objective function to be minimized is the least square error between the prescribed elastic modulus and the achieved elastic modulus. The total weight of the fundamental cell is constrained to be equal to a prescribed value. This formulation is slightly better in computational performance than that in Sigmund (1995) where the objective is to minimize the weight of the composite material and the effective elastic tensor is constrained to be equal to a prescribed value. Diaz and Benard (2003) also introduce thickness of the fundamental cell as a design variable which makes it possible to scale all entries of the elastic tensor without changing the topology.

The methodology to design an elastic material can be extended to design a viscoelastic material as in Yi et al. (2000), where the homogenization and inverse homogenization in frequency domain are formulated applying the correspondence principle. According to the correspondence principle, the viscoelastic homogenization (or inverse homogenization) process becomes identical to that of the elastic case except that the variables are complex in the viscoelastic case.

In this work, Diaz and Benard (2003) will be extended to design a viscoelastic composite that has the prescribed viscoelastic properties.

4.2 The Optimization Problem

As in Diaz and Benard (2003), the objective function to be minimized is the least square error between the prescribed elastic modulus and the achieved elastic modulus. Since the composite material being designed here is viscoelastic, the elastic tensor has real and imaginary parts that are functions of the forcing frequency. The objective function is given in (4.2.1)

$$\phi=\sum_{i=1}^{3}\sum_{j=1}^{N_\omega}\left[\frac{1}{2}\left(t\,{}_j^i\mathbf{E}-{}_j^i\mathbf{E}^*\right)^T {}_j^i\mathbf{W}\left(t\,{}_j^i\mathbf{E}-{}_j^i\mathbf{E}^*\right)\right] \tag{4.2.1}$$

where t is a scaling parameter, which physically may be interpreted as the thickness of the cell. ${}_j^i\mathbf{E}^*$ and ${}_j^i\mathbf{E}$, respectively, are the prescribed and the actual elastic tensors in a 6x1 vector form. ${}_j^i\mathbf{E}$ and ${}_j^i\mathbf{E}^*$ are in the form of $\{c_{1111}, c_{2222}, c_{1212}, c_{1122}, c_{1112}, c_{2212}\}^T$. In ${}_j^i\mathbf{E}^*$ and ${}_j^i\mathbf{E}$, the superscript i = 1, 2 and 3, represent real part, imaginary part and absolute value of the elastic tensor. The absolute value of the elastic tensor is also included in the objective function as for some applications the absolute value may also be of interest. The subscript j denotes the jth forcing frequency. The elastic tensors are prescribed at a prescribed number (N_ω) of forcing frequencies (ω_1, ω_2 , ..., ω_{N_ω}). The objective function is a sum of $18N_\omega$ individual least square error terms and has provisions to prescribe relative importance or 'weight' to these terms. The diagonal weight matrix

${}^{i}_{j}\mathbf{W}$ sets such relative importance to the entries of the elastic tensor. ${}^{1}_{j}\mathbf{W}$, ${}^{2}_{j}\mathbf{W}$ and ${}^{3}_{j}\mathbf{W}$, respectively, are the prescribed weight matrices for the real part, imaginary part and absolute values of the elastic tensor. For example, if only the absolute value of c_{1111} is of interest, then ${}^{1}_{j}\mathbf{W}$ and ${}^{2}_{j}\mathbf{W}$ are zero matrix. All entries of ${}^{3}_{j}\mathbf{W}$ are zero except the first diagonal entry.

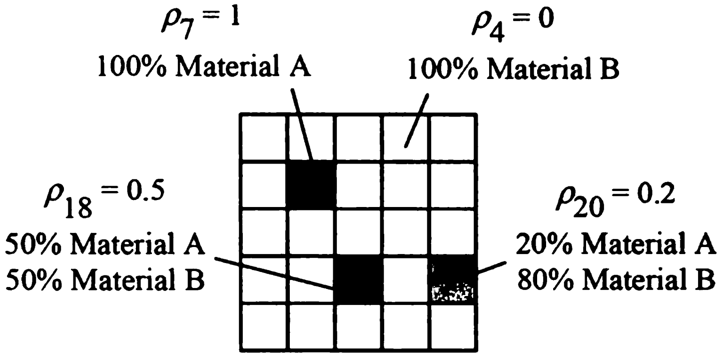

Figure 4.1 Element densities as design variables

The design domain for a fundamental cell is discretized into a number of finite elements, as shown in Fig. 4.1. The 'density' (ρ_e) of each element of the fundamental cell is the design variable. ρ_e is the volume fraction of phase A in element e and (1-ρ_e) is the volume fraction of phase B in that element, as shown in the figure. ρ_e thus can take any value between 0 and 1, i.e.,

$$0 \le \rho_e \le 1 \qquad \text{for } e = 1, 2, \ldots, N$$

where N is the total number of elements in the discretized fundamental cell.

The phase B used in this chapter is the same as that built in section 2.7 and used in the example in section 3.5. This phase is anisotropic and its elastic tensor, as in (2.7.11), is

$$C_B = \begin{bmatrix} 1.71 & 0.57 & 0 \\ 0.57 & -\dfrac{1.0166(1+i0.0002\omega)}{0.696+i0.0002\omega}+0.57 & 0 \\ 0 & 0 & 1.71 \end{bmatrix} E_A \tag{4.2.2}$$

As can be seen in (4.2.2), only the c_{2222} term in the elastic tensor of material B has negative stiffness, which is crucial for the frequency-induced softening. To achieve softening in the terms other than c_{2222}, material B needs to be rotated and suitably oriented. To achieve softening in more than one term simultaneously, the base cell may need to have material B oriented in more than one direction. Material B will, therefore, be allowed to be rotated from the prescribed original orientation. If θ_e is the angle of rotation of material B in element *e*, then the rotated elastic tensor is given by

$$c'_{ijkl} = a_{ip} a_{jq} a_{kr} a_{ls} c_{pqrs} \tag{4.2.3}$$

where a_{ij} are the entries of the transformation matrix given by

$$\mathbf{a} = \begin{bmatrix} \cos\theta_e & -\sin\theta_e \\ \sin\theta_e & \cos\theta_e \end{bmatrix} \tag{4.2.4}$$

where θ_e in this work is bounded as follows:

$-\pi/2 \le \theta_e \le \pi/2 \qquad \text{for } e = 1, 2, \ldots, N$

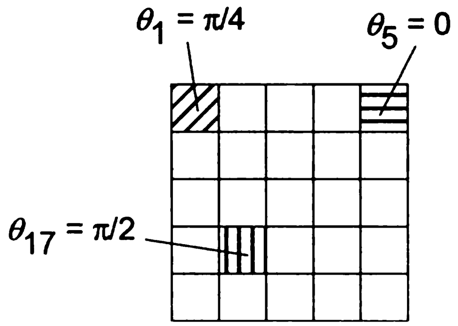

Figure 4.2 Angle of orientation of material B in an element as a design variable

There is a constraint used on the volume fraction of phase A in the fundamental cell. The constraint on the volume fraction is given by

$$v^l \leq \frac{1}{A_\Sigma} \sum_{e=1}^{N} A_e \rho_e \leq v^u$$

where $\mathbf{A} = \{A_1, A_2, \ldots, A_N\}^T$ is a vector containing element areas, v^u is a prescribed upper bound on the volume fraction of phase A in the composite, v^l is the corresponding prescribed lower bound and

$$A_\Sigma = \sum_{e=1}^{N} A_e$$

is the total area of the cell.

Stability of the composite material is ensured by implementing a constraint that basically requires the real part of the elastic tensor to be positive definite. In particular, eigenvalues of the real part of the effective elastic tensor (in 3x3 matrix form) are computed and are desired to have positive real part. The stability constraint may be written as

$$-\mathrm{Re}\,\lambda \leq \beta < 0$$

where β is a prescribed negative real number, which is the lower bound for the real part of λ. Here λ is an eigenvalue of the real part of ${}_j\mathbf{E}^H$ and has the real part the lowest among all the eigenvalues. λ is obtained by solving

$$\det\left[\mathrm{Re}\;{}_j\mathbf{E}^H - \lambda \mathbf{I}_{3\mathrm{x}3}\right] = 0 \qquad (4.2.5)$$

${}_j\mathbf{E}^H$ is the average elastic tensor for the composite in a 3x3 matrix form:

$${}_j\mathbf{E}^H = \begin{bmatrix} c_{1111} & c_{1122} & c_{1112} \\ c_{1122} & c_{2222} & c_{2212} \\ c_{1112} & c_{2212} & c_{1212} \end{bmatrix}$$

and is given by

$${}_jE_{qr}^H = \frac{1}{|Y|}\int_Y \frac{1}{2}\left(\varepsilon_0^q - \varepsilon^q\right)^T \mathbf{E}(\boldsymbol{\rho}, \boldsymbol{\theta}, \omega_j)\left(\varepsilon_0^r - \varepsilon^r\right) dY \qquad (4.2.6)$$

In (4.2.6), Y represents the fundamental cell i.e. the periodic domain over which the inverse homogenization problem is defined. $|Y| = A_{\Sigma}$ is the total area of the fundamental cell. $\mathbf{E}(\boldsymbol{\rho},\boldsymbol{\theta},\omega)$ is the element elastic tensor given by

$$\mathbf{E}^e(\rho_e,\theta_e,\omega) = \rho_e \mathbf{E}^A(\omega) + (1-\rho_e)\mathbf{E}^B(\theta_e,\omega) \tag{4.2.7}$$

$\mathbf{E}^A(\omega)$ and $\mathbf{E}^B(\theta_e,\omega)$ are the elastic tensors for material phases A and B respectively. The element elastic tensor $\mathbf{E}^e$ as a function of the phase elastic tensors ($\mathbf{E}^A$ and $\mathbf{E}^B$) and element density (ρ_e) such as in (4.2.7) is typical in a material distribution problem (as can be seen in Bendsøe and Sigmund (2003)). $\mathbf{E}^e$ is typically constructed such that ρ_e is discouraged to take an intermediate value between 0 and 1 while improving the objective function or satisfying the constraints. Here $\mathbf{E}^e(\rho_e,\theta_e,\omega)$ may be physically interpreted as the average elastic tensor of a Voigt composite made of phases A and B having volume fractions ρ_e and $(1-\rho_e)$ respectively.

In (4.2.6),

$\varepsilon_0^1 = \{1,0,0\}^T$

$\varepsilon_0^2 = \{0,1,0\}^T$

and

$\varepsilon_0^3 = \{0,0,1\}^T$

are the unit test strains applied for the purpose of determining the average elastic tensor of the composite material. ε^q in (4.2.6) is the strain induced by the test strain ε_0^q and is solution of this problem (which is solved by finite element approximation)

$$\int_Y \varepsilon(v)^T \mathbf{E}\varepsilon(u^q)dY = \int_Y \varepsilon(v)^T \mathbf{E}\varepsilon_0^q dY, \text{ for all } Y\text{-periodic functions } v \qquad (4.2.8)$$

where u^q is a Y-periodic solution. If Y is a unit square, then a function $\varphi(y_1, y_2)$ is Y-periodic if $\varphi(y_1+m, y_2+n) = \varphi(y_1, y_2)$ for any $(y_1, y_2) \in Y$ and integers m and n.

In summary, the optimization problem may be written as follows:

Find $\boldsymbol{\rho} = \{\rho_1, \rho_2, \ldots, \rho_N\}^T$, $\boldsymbol{\theta} = \{\theta_1, \theta_2, \ldots, \theta_N\}^T$ and t that

$$\text{minimize} \qquad \phi(\boldsymbol{\rho}, \boldsymbol{\theta}, t) = \sum_{i=1}^{3}\sum_{j=1}^{N_\omega}\left[\frac{1}{2}\left(t\,{}^i_j\mathbf{E} - {}^i_j\mathbf{E}^*\right)^T {}^i_j\mathbf{W}\left(t\,{}^i_j\mathbf{E} - {}^i_j\mathbf{E}^*\right)\right]$$

$$\text{subject to} \qquad 0 \le \rho_e \le 1 \qquad \text{for } e = 1, 2, \ldots, N \qquad (4.2.9)$$

$$-\pi/2 \le \theta_e \le \pi/2 \qquad \text{for } e = 1, 2, \ldots, N$$

$$-\mathrm{Re}\,\lambda \le \beta < 0$$

$$v^l \le \frac{1}{A_\Sigma}\sum_{e=1}^{N} A_e \rho_e \le v^u$$

Since ϕ is an unconstrained, convex function of t for fixed $\boldsymbol{\rho}$ and $\boldsymbol{\theta}$, following Diaz and Benard (2003), it is possible to express the optimal value of t as the solution of $\partial\phi/\partial t = 0$ which is

$$t^{*} = \frac{c_1}{c_2} \tag{4.2.10}$$

where

$$c_1 = \sum_{i=1}^{3} \sum_{j=1}^{N_\omega} \left({}^{i}_{j}\mathbf{E}^{*} \right)^{T} {}^{i}_{j}\mathbf{W}\, {}^{i}_{j}\mathbf{E} \tag{4.2.11}$$

$$c_2 = \sum_{i=1}^{3} \sum_{j=1}^{N_\omega} \left({}^{i}_{j}\mathbf{E} \right)^{T} {}^{i}_{j}\mathbf{W}\, {}^{i}_{j}\mathbf{E} \tag{4.2.12}$$

Incorporating t^{*} in the original objective function, the objective function to be minimized may be rewritten as

$$\phi(\boldsymbol{\rho}, \boldsymbol{\theta}) = \sum_{i=1}^{3} \sum_{j=1}^{N_\omega} \left[\frac{1}{2} \left(t^{*}\, {}^{i}_{j}\mathbf{E} - {}^{i}_{j}\mathbf{E}^{*} \right)^{T} {}^{i}_{j}\mathbf{W} \left(t^{*}\, {}^{i}_{j}\mathbf{E} - {}^{i}_{j}\mathbf{E}^{*} \right) \right] \tag{4.2.13}$$

The optimization problem may now be written as

Find $\boldsymbol{\rho} = \{\rho_1, \rho_2, \ldots, \rho_N\}^T$ and $\boldsymbol{\theta} = \{\theta_1, \theta_2, \ldots, \theta_N\}^T$ that

$$\begin{aligned}
&\text{minimize} && \phi(\boldsymbol{\rho}, \boldsymbol{\theta}) = \sum_{i=1}^{3} \sum_{j=1}^{N_\omega} \left[\frac{1}{2} \left(t^{*}\, {}^{i}_{j}\mathbf{E} - {}^{i}_{j}\mathbf{E}^{*} \right)^{T} {}^{i}_{j}\mathbf{W} \left(t^{*}\, {}^{i}_{j}\mathbf{E} - {}^{i}_{j}\mathbf{E}^{*} \right) \right] \\
&\text{subject to} && 0 \le \rho_e \le 1 \qquad \text{for } e = 1, 2, \ldots, N \\
& && -\pi/2 \le \theta_e \le \pi/2 \qquad \text{for } e = 1, 2, \ldots, N \\
& && -\operatorname{Re}\lambda \le \beta < 0 \qquad \text{(stability constraint)} \\
& && v^{l} \le \frac{1}{A_\Sigma} \sum_{e=1}^{N} A_e \rho_e \le v^{u} \qquad \text{(volume constraint)}
\end{aligned} \tag{4.2.14}$$

4.3 Sensitivity Analysis

The optimization problem (4.2.14) is solved using a gradient-based optimization method, viz. the method of moving asymptotes (Svanberg (1987)). The gradients of the objective function and the constraints with respect to the design variables (required for the numerical solution of the optimization problem) are derived in this section.

(i) Objective Function

The gradient of the objective function with respect to a design variable x_e (for example, ρ_e or θ_e) is given by

$$\frac{d\phi}{dx_e}=\sum_{i=1}^{3}\sum_{j=1}^{N\omega}\left[\left(t^{*}\,{}^{i}_{j}\mathbf{E}-{}^{i}_{j}\mathbf{E}^{*}\right)^{T}\,{}^{i}_{j}\mathbf{W}\left(\frac{dt^{*}}{dx_e}\,{}^{i}_{j}\mathbf{E}+t^{*}\frac{d\,{}^{i}_{j}\mathbf{E}}{dx_e}\right)\right] \tag{4.3.1}$$

where

$$\frac{dt^{*}}{dx_e}=\sum_{i=1}^{3}\sum_{j=1}^{N\omega}\frac{1}{c_2}\left({}^{i}_{j}\mathbf{E}^{*}-\frac{2c_1}{c_2}\,{}^{i}_{j}\mathbf{E}\right)^{T}\,{}^{i}_{j}\mathbf{W}\frac{d\,{}^{i}_{j}\mathbf{E}}{dx_e} \tag{4.3.2}$$

The derivatives of the real part, the imaginary part and the absolute value of the elastic moduli, i.e.,

$$\frac{d\,{}^{1}_{j}\mathbf{E}}{dx_e}=\mathrm{Re}\frac{d\,{}_{j}\mathbf{E}}{dx_e}, \tag{4.3.3}$$

$$\frac{d\,{}^{2}_{j}\mathbf{E}}{dx_e}=\mathrm{Im}\frac{d\,{}_{j}\mathbf{E}}{dx_e} \tag{4.3.4}$$

and

$$\frac{d\,{}_j^3E_k}{dx_e}=\frac{1}{{}_j^3E_k}\left({}_j^1E_k\frac{d\,{}_j^1E_k}{dx_e}+{}_j^2E_k\frac{d\,{}_j^2E_k}{dx_e}\right) \tag{4.3.5}$$

are easily obtained from

$$\frac{d\,{}_jE_{qr}^H}{d\rho_e}=\frac{\partial\,{}_jE_{qr}^H}{\partial\rho_e}=\frac{1}{A_e}\int_e\frac{1}{2}\left(\varepsilon_0^q-\varepsilon^q\right)^T\left(\mathbf{E}^A(\omega_j)-\mathbf{E}^B(\theta_e,\omega_j)\right)\left(\varepsilon_0^r-\varepsilon^r\right)dA \tag{4.3.6}$$

and

$$\frac{d\,{}_jE_{qr}^H}{d\theta_e}=\frac{\partial\,{}_jE_{qr}^H}{\partial\theta_e}=\frac{(1-\rho_e)}{A_e}\int_e\frac{1}{2}\left(\varepsilon_0^q-\varepsilon^q\right)^T\frac{\partial\mathbf{E}^B(\theta_e,\omega_j)}{\partial\theta_e}\left(\varepsilon_0^r-\varepsilon^r\right)dA \tag{4.3.7}$$

(ii) Stability Constraint

The derivative of the real part of the eigenvalue with respect to a design variable x_e is the same as the real part of the derivative of the eigenvalue, i.e.,

$$\frac{d(\mathrm{Re}\,\lambda)}{dx_e}=\mathrm{Re}\frac{d\lambda}{dx_e} \tag{4.3.8}$$

where the derivative of the eigenvalue is

$$\frac{d\lambda}{dx_e}=\left(\frac{dI_E}{dx_e}\lambda^2-\frac{dII_E}{dx_e}\lambda+\frac{dIII_E}{dx_e}\right)\Big/\left(3\lambda^2-2I_E\lambda+II_E\right) \tag{4.3.9}$$

I_E, II_E and III_E are the three invariants of $\mathrm{Re}\,{}_j\mathbf{E}^H$ and are given as

$$I_E=\mathrm{tr}\left(\mathrm{Re}\,{}_j\mathbf{E}^H\right) \tag{4.3.10}$$

$$II_E = \frac{1}{2}\left(\left(\operatorname{tr}\left(\operatorname{Re}\,{}_j\mathbf{E}^H\right)\right)^2 - \operatorname{tr}\left(\operatorname{Re}\,{}_j\mathbf{E}^H\right)^2\right) \tag{4.3.11}$$

$$III_E = \det\left(\operatorname{Re}\,{}_j\mathbf{E}^H\right) \tag{4.3.12}$$

The gradients of the three invariants are easily computed as $\dfrac{d\,{}_jE_{qr}^H}{dx_e}$ is already known from (4.3.6) and (4.3.7).

(iii) Volume Constraint

The gradient of the total volume fraction of phase A is trivially given by

$$\frac{d}{d\rho_e}\left(\frac{1}{A_\Sigma}\sum_{e=1}^{N} A_e\rho_e\right) = \frac{A_e}{A_\Sigma} \tag{4.3.13}$$

and

$$\frac{d}{d\theta_e}\left(\frac{1}{A_\Sigma}\sum_{e=1}^{N} A_e\rho_e\right) = 0 \tag{4.3.14}$$

4.4. Solution Strategy

To solve the optimization problem (4.2.14), an efficient strategy (in terms of fast convergence of the solutions) is found by trial and error. The strategy consists of the following three steps:

Step 1: Propose initial angle of rotation (θ_0) of material B.

There is no hard and fast rule for the initial assignment of θ_e; however, for faster and better convergence θ_e should be such that negative stiffness is available in all the directions along which softening is required. $\theta_e = 0$ and $\pi/2$ correspond to negative stiffness available in vertical (i.e. direction 2) and horizontal (i.e. direction 1) directions, respectively. If the shear modulus is desired to soften, then $\theta_e = \pm\pi/4$ may be used as this angle makes negative stiffness available in the diagonal direction of the element and softening in the diagonal direction leads to softening in shear. If softening is desirable in more than one entry of the elastic tensor, then $\theta_e = \pm\pi/4$ is, in general, found to give good results.

Step 2: Obtain $\boldsymbol{\rho}^*$, which is a solution of the following density optimization problem:

Find $\boldsymbol{\rho} = \{\rho_1, \rho_2, \ldots, \rho_N\}^T$ that

$$\begin{array}{lll}
\text{minimize} & \phi(\boldsymbol{\rho},\boldsymbol{\theta}_0) = \displaystyle\sum_{i=1}^{3}\sum_{j=1}^{N_\omega}\left[\frac{1}{2}\left(t^*\,{}_j^i\mathbf{E} - {}_j^i\mathbf{E}^*\right)^T {}_j^i\mathbf{W}\left(t^*\,{}_j^i\mathbf{E} - {}_j^i\mathbf{E}^*\right)\right] & \\
\text{subject to} & 0 \le \rho_e \le 1 & \text{for } e = 1, 2, \ldots, N \qquad (4.4.1) \\
 & -\operatorname{Re}\lambda \le \beta < 0 & \text{(stability constraint)} \\
 & v^l \le \dfrac{1}{A_\Sigma}\displaystyle\sum_{e=1}^{N} A_e\rho_e \le v^u & \text{(volume constraint)}
\end{array}$$

To facilitate a “black and white” solution, a morphology-based filter as given in Sigmund (2007) has been used. The morphology-based filter is an extension of the original density filter introduced by Bruns and Tortorelli (2001). An “open operator”, in particular, is used in the present work. As described in Sigmund (2007)), an open operator corresponds to erosion followed by dilation. In image processing, this operator corresponds to removing dimensional details smaller than a prescribed filter size. A Heaviside filter (basic version proposed in Guest et al. (2004)) is used as a dilation operator, whereas a modified Heaviside filter (proposed in Sigmund (2007)) is used as an erosion operator. It was observed that the open filter used in this work tremendously decreased (with iterations) the total volume fraction of the material corresponding to $\rho_e = 1$ (i.e. material A). To stabilize the volume fraction of material A, the volume constraint is found to be important. It was also observed that the optimization process works better and faster with the following constraint:

$$\frac{1}{N}\sum_{e=1}^{N} \rho_e (1 - \rho_e) \leq \delta$$

where δ is a prescribed number. This constraint has been used in solving the density problem (4.4.1). Note that while solving the density optimization problem, a parameter of the Heaviside function (viz. β in Sigmund (2007)) is doubled every 20th iteration as a scheme to gradually reduce number of gray elements in the design. The change in this parameter leads to a jump in the objective function value, as can be seen in the iteration history plots presented for the solved examples.

Step 3: Obtain $\boldsymbol{\theta}^*$, which is a solution of the following angle optimization problem:

Find $\boldsymbol{\theta} = \{\theta_1, \theta_2, \ldots, \theta_N\}^T$ that

$$\text{minimize} \qquad \phi(\boldsymbol{\rho}^*, \boldsymbol{\theta}) = \sum_{i=1}^{3} \sum_{j=1}^{N_\omega} \left[\frac{1}{2} \left(t^* \, {}^i_j\mathbf{E} - {}^i_j\mathbf{E}^* \right)^T {}^i_j\mathbf{W} \left(t^* \, {}^i_j\mathbf{E} - {}^i_j\mathbf{E}^* \right) \right]$$

$$\text{subject to} \qquad -\pi/2 \le \theta_e \le \pi/2 \qquad \text{for } e = 1, 2, \ldots, N \tag{4.4.2}$$

$$-\mathrm{Re}\,\lambda \le \beta < 0 \qquad \text{(stability constraint)}$$

4.5 Examples

In all the three examples given in this section, material phases A and B are fixed. The prescribed lower and upper bounds on the total volume fraction of A in the composite are 0.7 and 0.9 respectively. A and B are as used in the example in section 3.5. The elastic tensors for A and B are as follows:

$$C_A = \frac{(1 + i0.07)}{1 - 0.45^2} \begin{bmatrix} 1 & 0.45 & 0 \\ 0.45 & 1 & 0 \\ 0 & 0 & (1-0.45)/2 \end{bmatrix}$$

$$C_B = \begin{bmatrix} 1.71 & 0.57 & 0 \\ 0.57 & -\dfrac{1.0166(1 + i0.0002\omega)}{0.696 + i0.0002\omega} + 0.57 & 0 \\ 0 & 0 & 1.71 \end{bmatrix}$$

4.5.1 Optimization example 1

In this example, the goal is to design a composite that will exhibit softening in shear. The prescribed $||c_{1212}||$ are 0.73, 0.51 and 0.31 for the forcing frequencies 0, 100 and 2000 Hz respectively.

The base cell is square-shaped and is discretized into 30x30 elements. The initial guess for the angle of rotation of material B (in Step 1) is 90 degrees for all elements. The initial guess is arbitrary. After solving the density optimization problem in Step 2, an optimal geometry is obtained, which is shown in Fig. 4.3. The solution was assumed to be symmetric about both the horizontal and vertical centerlines of the base cell. In all the examples in this work, only a quarter (top-right) of the base cell is designed and the other three quarters are created as mirror images of the designed quarter. The dark areas in the designed base cell represent material A and the white areas represent B. A few grey elements in the cell represent a mixture of materials A and B. As in a typical material design problem, it is very difficult to completely eliminate the gray areas because gray elements are mathematically allowed in the optimal designs. The total volume fraction of material A in the composite is 0.764. The obtained $||c_{1212}||$ is 0.4167, 0.4133 and 0.4011, respectively, at the three frequencies. The target and the achieved $||c_{1212}||$ are plotted in Fig. 4.4, where the target values are shown as crosses while the achieved values are shown as circles. The iteration history (i.e. the objective function plotted versus iteration number) is shown in Fig. 4.5. The objective function value is almost constant throughout the iteration history as can be seen in the figure. This is as expected. The negative stiffness is currently not oriented along the element diagonals, whereas softening of shear modulus requires negative stiffness to be oriented along the diagonals.

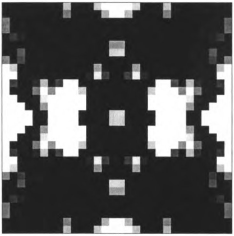

Figure 4.3. The composite designed in example 1 (initial angle 90 degrees)

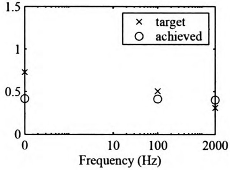

Figure 4.4. Plot of the target and achieved $||c_{1212}||$ for the density problem of example 1 (initial angle 90 degrees)

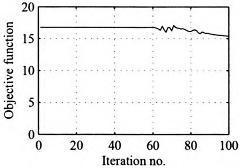

Figure 4.5. Iteration history for example 1 for the density problem of example 1 (initial angle 90 degrees)

The angle optimization problem is Step 3 is now solved in order to improve the objective function value. The resulting angles of rotation for material B in the elements are shown in Fig. 4.6, where every element is shown as a square and the line across the square represents the actual orientation of material B. For example, a horizontal line denotes 0 degree and a vertical line represents 90 or -90 degrees. The optimal angles of rotation range between 45 and 90 degrees in the top-right and bottom-left quarters of the base cell (i.e. between -45 and -90 degrees in the other two quarters). These angles approximately orient the negative stiffness along the diagonals of the base cell and help to achieve softening in shear. The solution is as expected. The resulting dynamic modulus ($||c_{1212}||$) is plotted and compared with the target value in Fig. 4.7. As can be seen in the figure, the dynamic modulus is the same as the target value and thus decreases with frequency. Figure 4.8 shows the iteration history. The objective function has, in general, improved with the number of iterations. The humps in the plot may be avoided by using a smaller step size in the optimization routine.

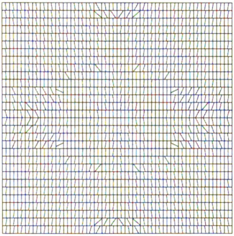

Figure 4.6. Orientation of material B for example 1 (initial angle 90 degrees)

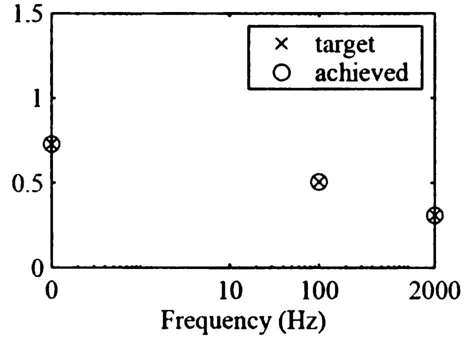

Figure 4.7. Plot of the target and achieved $||c_{1212}||$ for the angle problem of example 1 (initial angle 90 degrees)

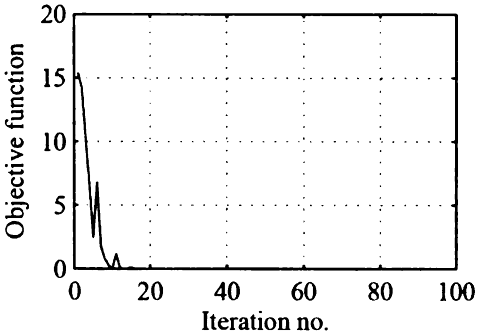

Figure 4.8. Iteration history for the density problem of example 1 (initial angle 90 degrees)

Example 1 with a different initial angle

The problem is now solved with a different initial angle of rotation for B. The angle is as shown in Fig. 4.9. The angle is 45 degrees for the upper-right and lower-left quarters of the base cell and -45 degrees elsewhere. The base cell obtained by solving the density problem (Step 2) is shown in Fig. 4.10. The volume fraction of material A in the cell is 0.794. The elastic modulus is plotted in Fig. 4.11. As can be seen in the figure, the achieved modulus is already the same as the target value and therefore angle optimization is not needed. The optimization problem was, thus, easier to solve with 45 degrees as initial guess. 45 degrees is a good guess as this angle will orient the negative stiffness along the diagonals and help shear modulus to soften. This may imply that with a good guess for the initial angle, the target properties may be achieved by solving the density problem only.

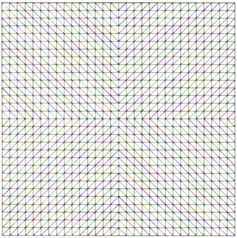

Figure 4.9. New initial angle for example 1

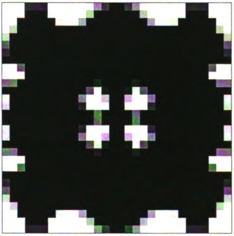

Figure 4.10. Optimal base cell for example 1 (initial angle 45 degrees)

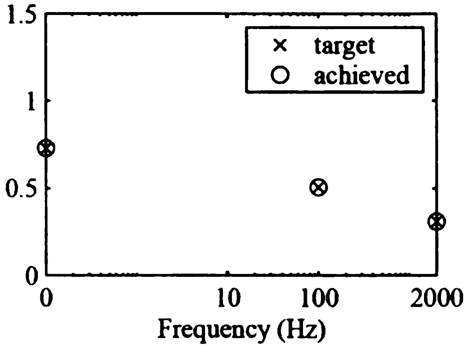

Figure 4.11. Plot of the target and achieved $||c_{1212}||$ for example 1 (initial angle 45 degrees)

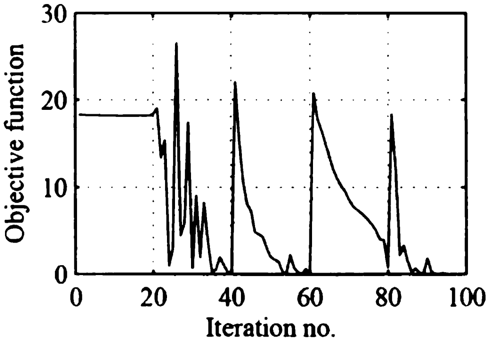

Figure 4.12. Iteration history for example 1 (initial angle 45 degrees)

The iteration history is shown in Fig. 4.12. As can be seen in the figure, the objective function undergoes a jump a few times. The jumps in the objective function value at iterations 20, 40, 60 and 80 are because of the doubling of a parameter of the Heaviside function (viz. β in Sigmund (2007)) as mentioned in section 4.4 (Step 2). The other jumps may be because the effective elastic tensor is very sensitive to the design variables (ρ) to the extent that a small change in the design variables tremendously changes the objective function value. This jump in the objective function value may be avoided by using a smaller step size in the optimization routine.

4.5.2 Optimization example 2

This example designs a material that softens in two directions – in the c_{1111} and c_{2222} entries of the elastic tensor. The desired $||c_{1111}||$ and $||c_{2222}||$ are equal and given to be 3.07, 2.59 and 0.99 at three prescribed forcing frequencies 0, 100 and 2000 Hz respectively. The initial guess for the angle of material B is 90 degrees for all elements.

The optimal base cell obtained by the density optimization (Step 2) is shown in Fig. 4.13. The volume fraction of material A is 0.774. $||c_{1111}||$ and $||c_{2222}||$ for the three frequencies {0,100,2000} Hz are {3.2368, 1.9447, 0.8793} and {1.4750, 1.4728, 1.4728} respectively. The dynamic moduli are plotted in Fig. 4.14. As can be seen in the figure, $||c_{1111}||$ is close to the target value (and therefore softens); however, $||c_{2222}||$ is considerably different from the target and is almost constant with respect to the frequency. 90 degree angle of rotation for material B corresponds to negative stiffness oriented along horizontal direction (i.e. direction 1), which helps the composite to achieve softening in the c_{1111} entry. $||c_{1111}||$ is constant here because it is not possible to soften c_{1111} by orienting negative stiffness only along direction 2. Figure 4.15 shows the iteration history.

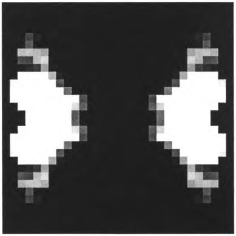

Figure 4.13. Geometry of the base cell designed in example 2 (initial angle 90 degrees)

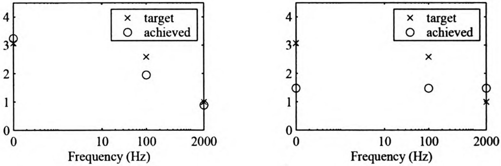

(a) $||c_{1111}||$ (b) $||c_{2222}||$

Figure 4.14. Plot of the target and achieved dynamic moduli for the density problem of example 2 (initial angle 90 degrees)

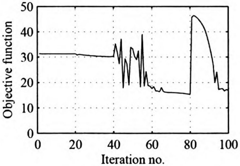

Figure 4.15. Iteration history for the density problem of example 2 (initial angle 90 degrees)

Angle optimization (Step 3) is now carried out. The resulting angle is shown in Fig. 4.16. It may be seen in the figure that the angles corresponding to the white areas of the base cell (shown in Fig. 4.13) are either 90 degrees or about 45 degrees. While a 90 degree angle helps the composite to soften in direction 1, a 45 degree angle helps softening in the both directions 1 and 2. The resulting $||c_{1111}||$ is 3.1098, 2.4162 and 0.9631, respectively, for the three forcing frequencies. The corresponding $||c_{2222}||$ values are 2.9720, 1.4681 and 1.2625. The target and achieved $||c_{1111}||$ are plotted versus the forcing frequency in Fig. 4.17. As can be seen in the figure, the absolute values of c_{1111} and c_{2222} decrease with frequency and thus the material designed here shows softening in both – horizontal and vertical directions. However, the achieved $||c_{2222}||$ is a little off the target value. With a different initial angle, the results could be improved as illustrated next. The iteration history is shown in Fig. 4.18, which indicates gradual improvement in the objective function value with iterations.

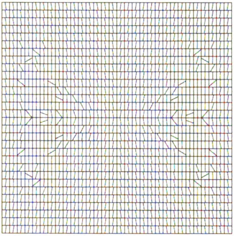

Figure 4.16. Optimal angle of orientation for material B for example 2 (initial angle 90 degrees)

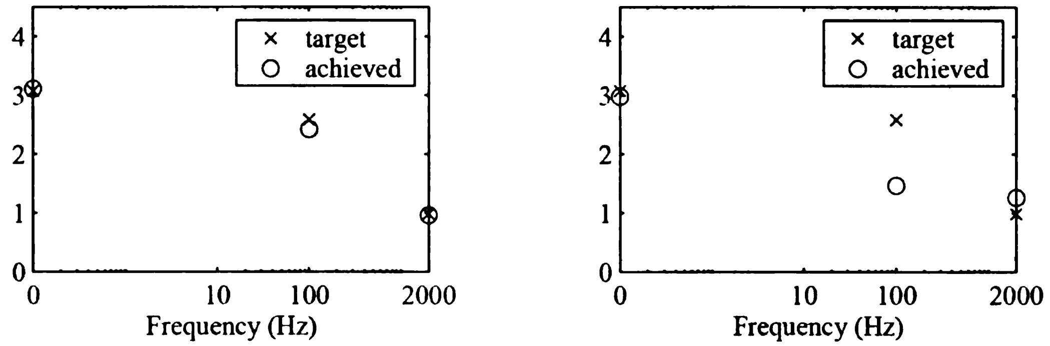

(a) $||c_{1111}||$ (b) $||c_{2222}||$

Figure 4.17. Plot of the target and achieved dynamic moduli for the angle problem of example 2 (initial angle 90 degrees)

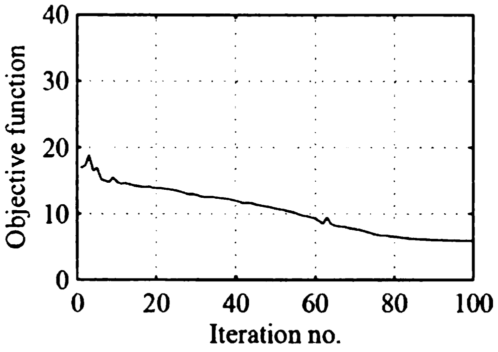

Figure 4.18. Iteration history for the angle problem of example 2 (initial angle 90 degrees)

Example 2 with a different initial angle

The initial angle is now changed to ±45 degrees as shown in Fig. 4.9 in the previous example. The solution of the density problem is shown in Fig. 4.19. The volume fraction of A is 0.7 (i.e. equal to the lower bound). The dynamic moduli are plotted in Fig. 4.20. The iteration history is given in Fig. 4.21.

Figure 4.19. Geometry of the base cell designed in example 2 (initial angle 45 degrees)

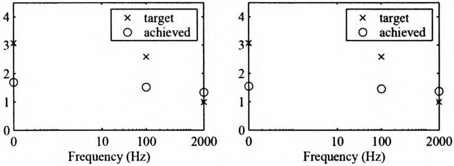

(a) $||c_{1111}||$ (b) $||c_{2222}||$

Figure 4.20. Plot of the target and achieved dynamic moduli for the density problem of example 2 (initial angle 45 degrees)

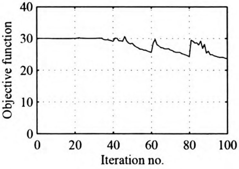

Figure 4.21. Iteration history for the density problem of example 2 (initial angle 45 degrees)

$\|c_{1111}\|$ is 1.6887, 1.5127 and 1.3313, respectively, for the three frequencies. The corresponding $\|c_{2222}\|$ is 1.5455, 1.4526 and 1.3641. $\|c_{1111}\|$ and $\|c_{2222}\|$ decrease very slightly with frequency.

The solution of the angle problem is shown in Fig. 4.22. The angles corresponding to the white areas of the base cell (Fig. 4.19) vary element to element; however, the angles are around 45 degrees. $\|c_{1111}\|$ is 3.1006, 2.4704 and 1.0324, whereas $\|c_{2222}\|$ is 3.0688, 2.5559 and 0.9919 respectively for the three frequencies. The dynamic moduli are plotted in Fig. 4.23, where it can be seen that the composite's dynamic moduli are the same as the target values. Figure 4.24 shows the iteration history.

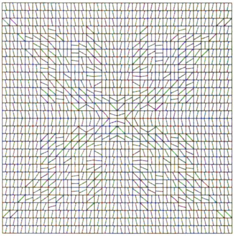

Figure 4.22. Optimal orientation of material B for example 2 (initial angle 45 degrees)

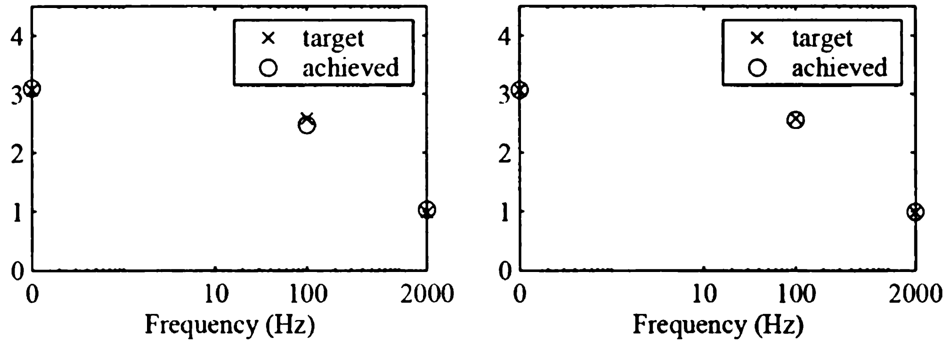

(a) $||c_{1111}||$ (b) $||c_{2222}||$

Figure 4.23. Plot of the target and achieved dynamic moduli for the angle problem of example 2 (initial angle 45 degrees)

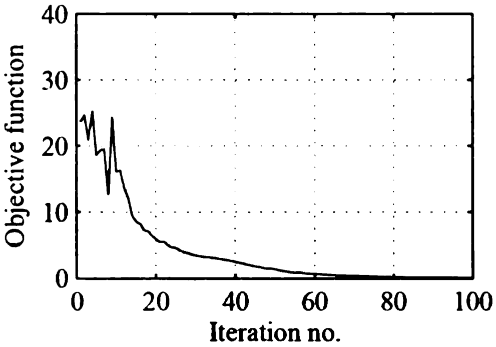

Figure 4.24. Iteration history for the angle problem of example 2 (initial angle 45 degrees)

4.5.3 Optimization example 3

In this example, the aim is to design a composite that is approximately isotropic. The absolute values of all entries of the elastic tensor are desired to decrease with frequency. The absolute values (in 6x1 vector form) are prescribed to be $\{3.07,3.07,0.85,1.38,0,0\}^T$, $\{2.59,2.59,0.71,1.16,0,0\}^T$ and $\{0.99,0.99,0.27,0.45,0,0\}^T$ for three frequencies 0, 100 and 2000 Hz respectively.

The initial angle for material B is 90 degrees. Figure 4.25 shows the solution of the density problem. The volume fraction of A is 0.804. The elastic moduli are $\{2.8005, 1.5368, 0.5069, 0.7142, 0, 0\}^T$, $\{1.8973, 1.5345, 0.5069, 0.6682, 0, 0\}^T$ and $\{0.7868, 1.5299, 0.5092, 0.6060, 0, 0\}^T$, respectively, for the given frequencies. $||c_{1111}||$ is able to soften with frequency because the 90 degree angle orients the negative stiffness along direction 1. $||c_{1122}||$ is also able to slightly decrease with frequency. The other two entries $||c_{2222}||$ and $||c_{1212}||$ are constant with respect to frequency as the negative stiffness oriented only along direction 1 cannot produce softening in direction 2 and along the diagonals of the base cell. The elastic moduli are plotted Fig. 4.26. $||c_{2222}||$ differs significantly from the target values. The iteration history is shown in Fig. 4.27.

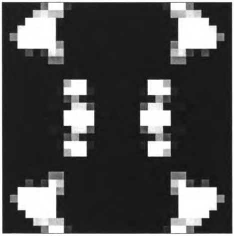

Figure 4.25. Geometry of the base cell designed in example 3 (initial angle 90 degrees)

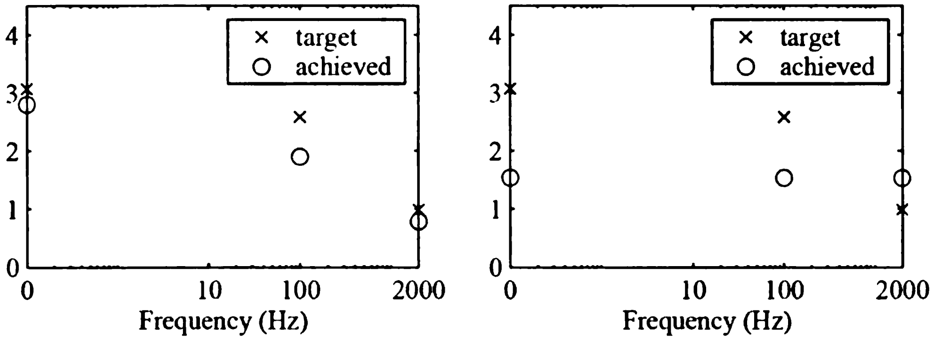

(a) $\|c_{1111}\|$ (b) $\|c_{2222}\|$

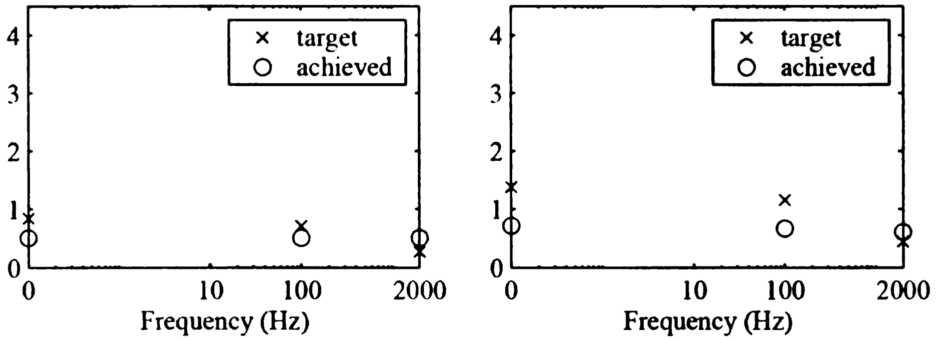

(c) $\|c_{1212}\|$ (d) $\|c_{1122}\|$

Figure 4.26. Plot of the target and achieved dynamic moduli for the density problem of example 3 (initial angle 90 degrees)

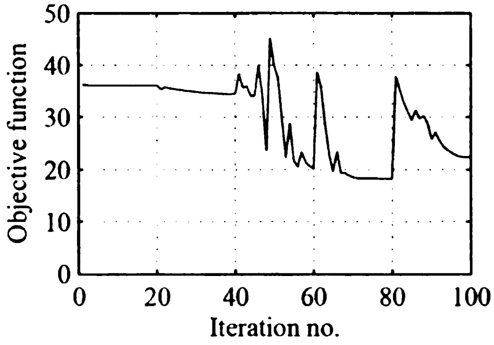

Figure 4.27. Iteration history for the density problem of example 3 (initial angle 90 degrees)

The results are improved further by solving the angle problem. The optimal angles are shown in Fig. 4.28. The elastic moduli are $\{3.0780, 2.3906, 0.5839, 1.2802, 0, 0\}^T$, $\{2.2849, 1.7438, 0.5321, 0.8471, 0, 0\}^T$ and $\{0.9934, 1.3567, 0.4106, 0.4612, 0, 0\}^T$, respectively, for the three frequencies. The elastic moduli and iteration history are shown in Figs. 4.29 and 4.30. Although all non-zero entries soften with frequency, all of them are a little off the target values. A different initial angle will now be used to check whether results can be improved.

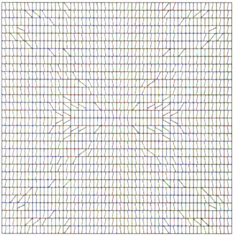

Figure 4.28. Optimal orientation of material B for example 3 (initial angle 90 degrees)

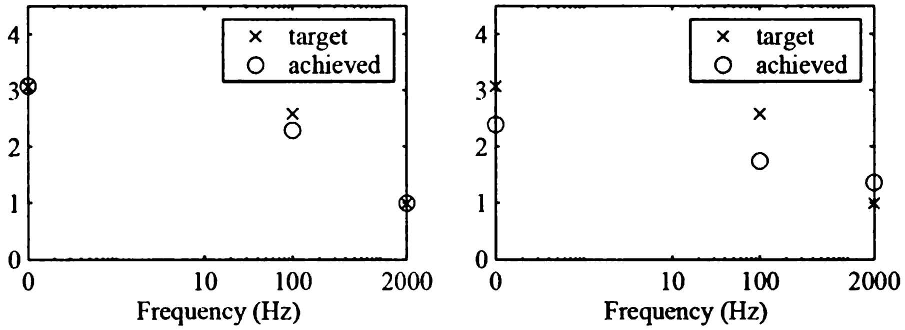

(a) $||c_{1111}||$ (b) $||c_{2222}||$

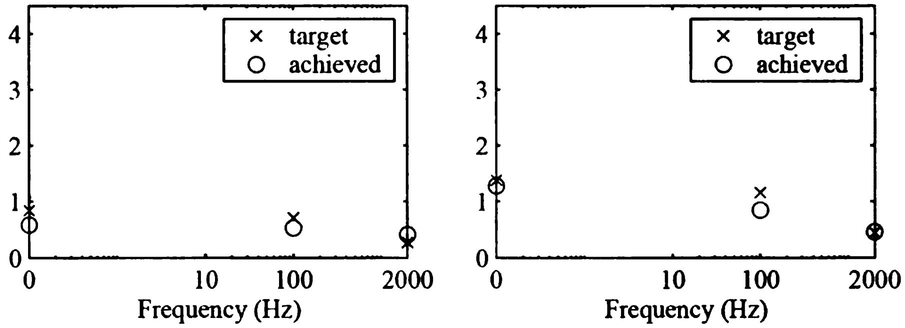

(c) $||c_{1212}||$ (d) $||c_{1122}||$

Figure 4.29. Plot of the target and achieved dynamic moduli for the angle problem of example 3 (initial angle 90 degrees)

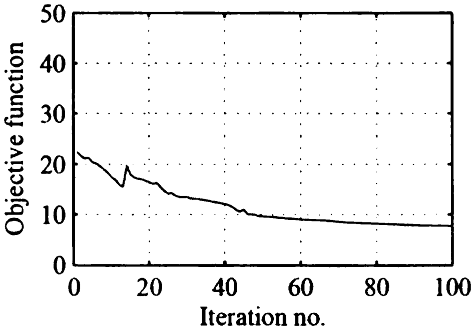

Figure 4.30. Iteration history for the angle problem of example 5 (initial angle 90 degrees)

Example 3 with different a initial angle

The initial angle for material B is now ±45 degrees (as shown in Fig. 4.9 in the first example). The geometry of the base cell obtained after solving the density problem is shown in Fig. 4.31. The total volume fraction of A in the designed composite is 0.709 (i.e. close to the lower bound, which is 0.7). For the three forcing frequencies, the elastic moduli are $\{1.8132, 1.7057, 0.5931, 0.6245, 0, 0\}^T$, $\{1.6670, 1.5837, 0.3793, 0.5557, 0, 0\}^T$ and $\{1.3735, 1.4097, 0.2464, 0.3008, 0, 0\}^T$. The elastic moduli and the iteration history are plotted in Figs. 4.32 and 4.33 respectively. As can be seen in Fig. 4.32, the elastic moduli are considerably different from the target values.

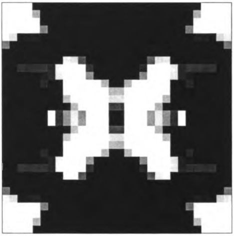

Figure 4.31. Geometry of the base cell designed in example 3 (initial angle 45 degrees)

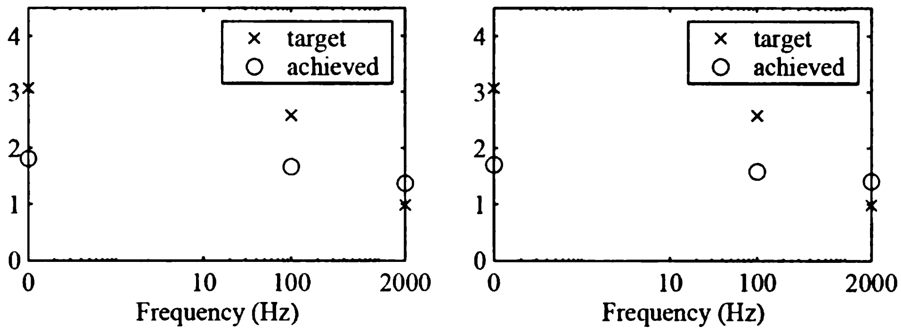

(a) $||c_{1111}||$ (b) $||c_{2222}||$

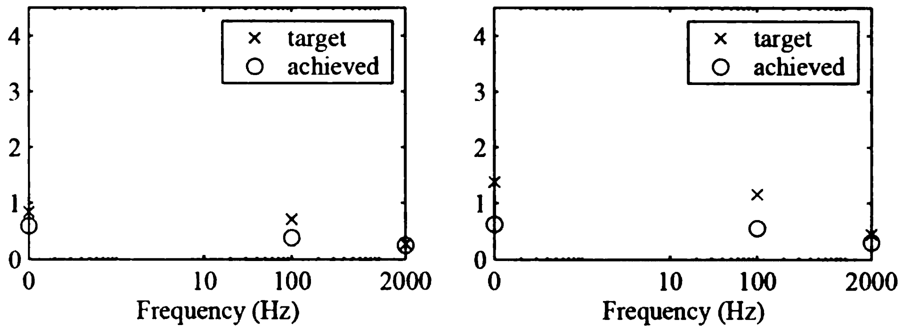

(c) $||c_{1212}||$ (d) $||c_{1122}||$

Figure 4.32. Plot of the target and achieved dynamic moduli for the density problem of example 3 (initial angle 45 degrees)

Figure 4.33. Iteration history for the density problem of example 6 (initial angle 45 degrees)

The optimal angle, i.e., the solution of the angle problem is shown in Fig. 4.34. Figure 4.35 shows the corresponding dynamic moduli. The dynamic moduli are approximately the same as the target values and therefore soften with frequency. The achieved values are $\{3.0654, 3.0856, 0.8579, 1.3966, 0, 0\}^T$, $\{2.5122, 2.4920, 0.6821, 1.1010, 0,0\}^T$ and $\{1.0405, 1.0349, 0.2856, 0.3382, 0, 0\}^T$ at the three frequencies. The iteration history is shown in Fig. 4.36.

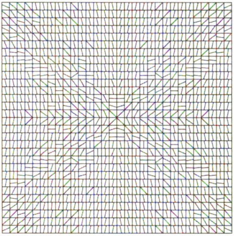

Figure 4.34. Optimal orientation of material B for example 3 (initial angle 45 degrees)

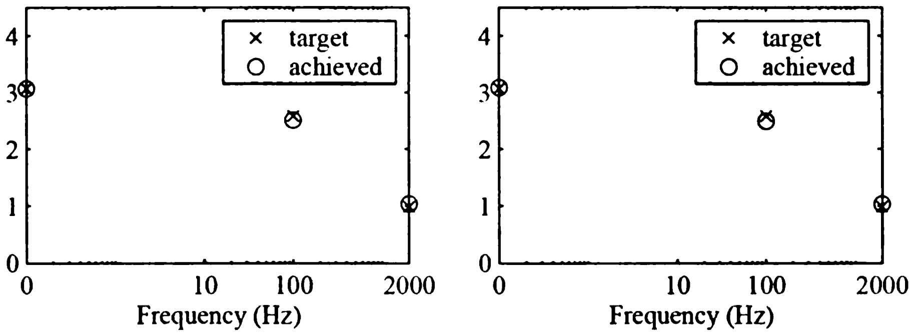

(a) $||c_{1111}||$ (b) $||c_{2222}||$

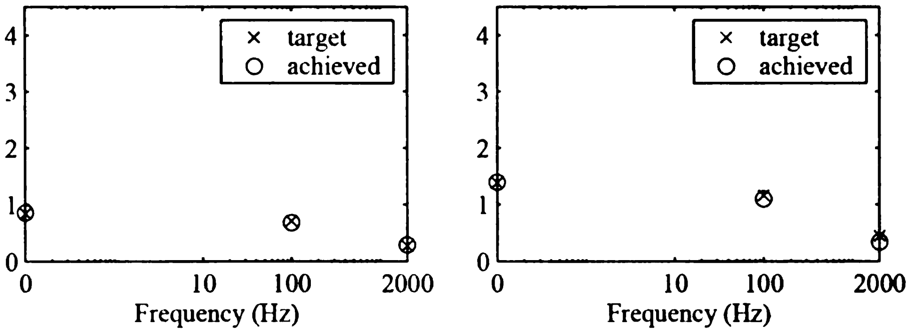

(c) $||c_{1212}||$ (d) $||c_{1122}||$

Figure 4.35. Plot of the target and achieved dynamic moduli for the angle problem of example 3 (initial angle 45 degrees)

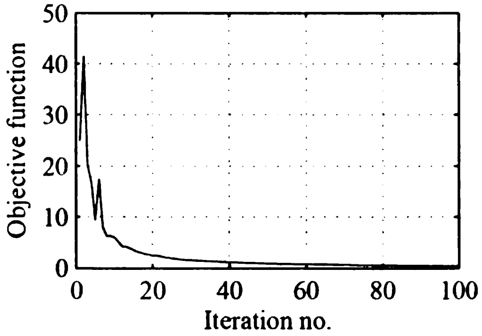

Figure 4.36. Iteration history for the angle problem of example 3 (initial angle 45 degrees)

4.6. Summary and Discussion

In this chapter, two-phase composites that show frequency-induced softening are designed. One phase, phase A, is a typical viscoelastic material. The other, phase B, is a negative-stiffness, lumped system. A typical topology optimization is used as a tool to design the composite. However, the present problem is considerably more complicated than a typical material design problem. In a typical material design problem, only the element densities (ρ) are design variables. In the present work, the angles of rotation (θ) of material B in the elements are also treated as design variables. As in a typical material design problem, the objective is to minimize the least square error between the prescribed and the actual elastic tensors and there is a constraint on the volume fraction of material A in the base cell. The elastic tensor is also constrained to be positive definite in order to ensure stability of the material and this constraint is not needed in a usual material design problem. As the effective properties of a composite having negative stiffness inclusions are very sensitive to the design variables (ρ_e and θ_e), the present problem is found to be very difficult to solve using a typical topology optimization method. In view of this, the design problem is proposed to be solved in two stages. In the first stage, initial angles of rotation of material B are guessed. The angles are kept constant while element densities are allowed to vary. In the second stage, the element densities obtained from the first stage are kept constant and the angles are allowed to vary. If the initial angles of rotation are judicially chosen, it is possible to obtain the desired properties in the first stage itself. In a complex problem, where the initial guess is difficult, the angles may be chosen as ±45 degrees (as in Fig. 4.9) as this angle is generally found to give good results. This is because this angle orients the negative stiffness along the diagonals of the base cell, which not only helps softening in shear but is also found to help softening in directions 1 and 2. In all the three examples, the initial angle of ±45 degrees resulted in the effective properties very close to the target values. The results obtained from the initial angle of 90 degrees are generally found to be a little off from the target values.

The presence of the negative stiffness material phase in the composite is found to lead to difficulties in obtaining purely black and white geometry of the base cell. For this reason, an advanced filtering method such morphology-based black and white filtering (using Heaviside functions) has been used in the present work. There are, however, still a few gray elements in the base cell designed. These gray areas may be eliminated by refining the discretization of the base cell and running the density optimization routine for more number of iterations. Refined mesh will also give mesh-independent, smooth geometry of the base cell. Refining mesh, however, decreases time efficiency.

CHAPTER 5

SYNTHESIS OF TILEABLE BISTABLE STRUCTURES

In the previous chapters, two-phase composites that exhibit frequency-induced softening have been designed. Once layout of the composite is known, the next step is to physically realize the composite material. The matrix phase may be a typical rubber-like material, which is easily available. The negative-stiffness inclusion phase, on the other hand, is not available and therefore needs to be physically realized first as a first step towards realizing the whole composite material. As introduced in chapter 2, bistable structures have potential to provide the composite with the required negative stiffness. The lumped lattices of material B_1 or B proposed here (as given in sections 2.6 and 2.7) have bistable structures as well as typical elastic/viscoelastic structures. One way to synthesize such a lumped lattice is to build the components separately and then assemble them together. The lumped system of material B_1 or B is proposed to be built in two steps – (i) build two-dimensional (tileable) bistable structures and (ii) interconnect the tileable bistable structures with blocks of typical elastic/viscoelastic materials such that the resulting structures is equivalent to the lumped system proposed in sections 2.6 or 2.7. An example of the resulting structure is shown in section 2.8. As the typical elastic or viscoelastic components of the lattice system are easily available, physical realization of the lumped system boils down to the physical realization of tileable bistable structures. Accordingly, this chapter concentrates on the synthesis of two-dimensional bistable structures. However, the problem of designing bistable structures will be treated as independent and general purpose. As such, this chapter may seem to be a little disconnected from the other chapters because of the independent treatment; however, this work is important for the physical realization of the negative-stiffness materials.

As pointed out earlier, the goal of this chapter is to design a two-dimensional, tileable bistable structure that can be used as a building block of the negative stiffness phase required to achieve frequency-induced softening. The 2D bistable structures are designed using a structural topology optimization technique, where the objective is to maximize the spatial difference in the two stable configurations of the bistable structures (recall that bistable structures have two stable configurations with no external loads). The geometry of the bistable structure is represented by a prescribed set of interconnected beams. The set is known as a ground structure. The aim of the optimization is to remove the unwanted beams from the ground structure so that the remaining interconnected beams functions as a bistable structure. The middle region and the end regions are allowed to have different cross-sectional areas (or materials). A thin cross section or a flexible material at either end (as compared to a thick or stiff material at the middle) of a few beams in the structure is a key to achieve bistability. Accordingly, cross-sectional areas of the end region of the beams are treated as design variables. As an alternative, the materials of the end regions are also treated as design variables. The optimization problem is solved using a stochastic optimization method, viz. a genetic algorithm (GA). A penalty function is devised and incorporated in the objective function in order to avoid an invalid structure as a solution. A typical bistable structure synthesized in this work is as shown in Fig. 5.18.

5.1 Introduction

A bistable compliant structure has two stable equilibrium configurations when unloaded. Once such structure reaches one of its stable configurations, it remains there unless it is provided with enough energy to "climb" out of an energy well that leads into the other stable configuration. This feature of bistable structures can be advantageous in designing a variety of mechanical devices, such as switching devices in MEMS, relays, valves, etc. The term bistable *periodic* structure is used to refer to an arrangement of interconnected bistable structures that tile a plane periodically. The load need not be periodic and the tiling need not be infinite. This chapter discusses a computational strategy to design bistable periodic structures using topology optimization. Understanding the behavior and developing a methodology for design of bistable, periodic *microstructures* is a first step towards design of bistable *materials*, a principal motivation of this work.

A typical example of a bistable compliant structure is a bistable compliant mechanism (e.g., see Jensen et al. (1999), Jensen et al (2001), Jensen and Howell (2003), Masters and Howell (2003), King and Campbell (2004)). Such mechanisms typically rely on strain energy storage to gain bistable behavior. They are made of flexible members, which produce motion and at the same time, store energy. Compliant mechanisms in general (e.g., see Howell (2001)) offer several advantages when used in design, specially in design of MEMS, and have been the subject of extensive research. Particularly relevant to this effort is previous work where a topology optimization strategy is used to synthesize compliant mechanisms, e.g., as discussed in Ananthasuresh and Kota (1995), Sigmund (1997) and Frecker et al. (1997).

A distinguishing feature of any bistable compliant structure is the shape of its strain energy curve. Figure 5.1 shows a qualitative description of the variation of strain energy with strain for a typical bistable compliant structure. The function is non-convex. The strain energy curve has three critical points - two minima (points C and G) and one maximum (point E). When the system is unloaded, and under small loads, the structure will operate in and around one of the two minima, corresponding to one stable configuration. Transition from one configuration to the next requires the addition of sufficient energy to jump over the small maximum and over into the neighborhood of the other minimum. An external load provides this activation energy in the form of external work and switches the structure from one stable configuration to the other. Once the new state is reached, again the structure will operate in and around this configuration, for small enough inputs. As indicated in Fig. 5.1, there are other characteristic points on the strain energy curve, which are described in detail in section 4.2. The shape of the strain energy curve around these points gives quantitative measures of the bistability. These points will be used to produce a measure of performance that can guide an eventual methodology for optimization of bistable periodic structures.

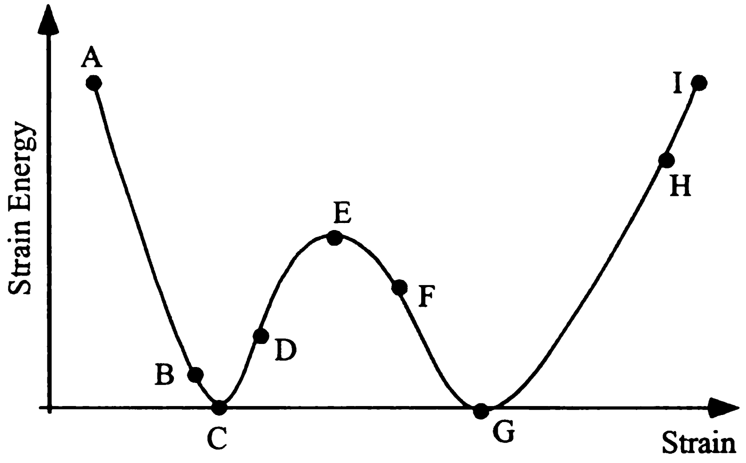

Figure 5.1. Strain energy versus strain in a typical bistable structure

The design of compliant mechanisms typically follows one of two principal approaches. The kinematics approach produces a structure composed of small flexible pivots and relatively rigid links. This approach results in lumped compliance, such as locally deforming flexural joints. The structural topology optimization approach is based on the methodology for topology optimization of structures introduced by Bendsøe and Kikuchi (1988) and uses either a continuum modeling based on plane elasticity (e.g., Sigmund (1997) and Bruns et al (2002)) or a ground structure approach that relies on slender members (beams and bars, e.g., Frecker et al (1997), Joo and Kota (2004)).

This chapter investigates the automatic topology synthesis of two-dimensional bistable compliant, periodic structures using a ground structure topology optimization approach. Section 5.2 introduces a concept for a bistable structure that can be repeated periodically to tile the plane. This concept is used simply to highlight basic features that one may expect to find in the layout of these structures. Section 5.3 describes the finite element model used for analysis of compliant bistable structures. A possible topology optimization problem formulated to synthesize a compliant bistable structure is described in section 5.4. Two examples in section 5.5 and one example in section 5.6 illustrate the methodology.

5.2 An Example of a Bistable Periodic Structure

This section introduces a design concept that can be repeated periodically to tile the plane and form a bistable periodic structure. This concept is used to highlight basic features of these structures that may be used later in deciding how to build a ground structure for topology optimization.

In Qiu et. al. (2004), the authors present a monolithic mechanically-bistable mechanism that uses no latches, no hinges and no residual stress. The typical implementation of this mechanism involves two curved, centrally-clamped parallel beams, labeled "double curved beams". Figure 5.2 shows a simplified "double curved beam" bistable mechanism, where each of the curved beams (shown as dashed lines) is approximated as two straight beams. This simple concept may be used to build a two-dimensional bistable structure, in this case, using four such bistable mechanisms, as shown in Fig. 5.3. In the figure, one of the four component bistable mechanisms is encircled by a dashed line and shown alone in Fig. 5.4. The original central clamp (the dark, vertical line in Fig. 5.2) is replaced by a stiff triangular structure in Figs. 5.3 and 5.4. This allows the incorporation of two input points, where loads are applied on each side of the structure. In addition, the beams are thickness modulated, i.e., the cross-sectional area of either beam is allowed to vary along its length to provide more control on the bistability characteristics of the structure. A simple way of implementing a thickness modulation considered here is to use beams of two different cross-sectional areas.

Bistability is achieved by designing the structure such that some of the members buckle or "snap". In the structures shown in Figs. 5.3 and 5.4, members which may snap are shown as light gray lines. Members shown as dark lines are stiffer, stiff enough to provide clamping support to the snapping beams. The configuration shown in Fig. 5.3 corresponds to the first equilibrium configuration of the structure. When loaded as shown by a load of sufficient magnitude, the structure moves into its second equilibrium configuration, shown in Fig. 5.5.

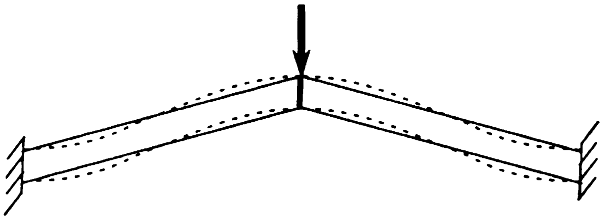

Figure 5.2. Simplified "double curved beam" bistable mechanism

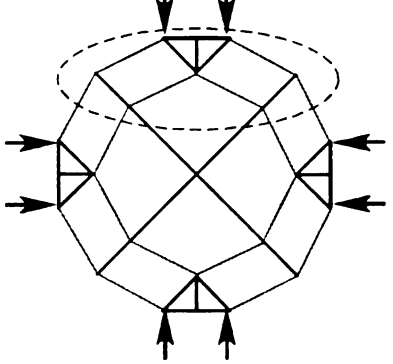

Figure 5.3. A bistable structure (first stable configuration) based on four "double curved beam" sub-structures.

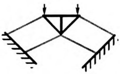

Figure 5.4. A sub-structure of Fig. 5.3 that is a bistable mechanism

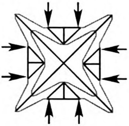

Figure 5.5. A bistable structure (second stable configuration) based on four "double curved beam" sub-structures

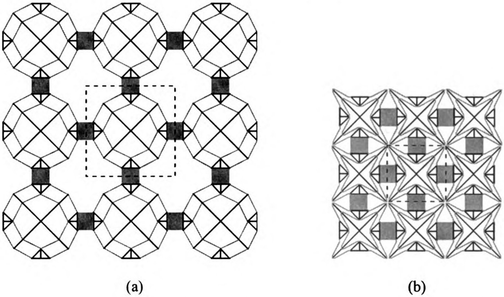

(a) (b)

Figure 5.6. A 3x3 periodic arrangement of bistable structures (a) first equilibrium configuration (b) second equilibrium configuration

The bistable structure shown in Fig. 5.3 can be repeated periodically to tile a plane, joining each unit together via rigid connectors (shown as solid rectangles). Two stable equilibrium configurations of such structure are shown in Fig. 5.6. The dashed box shows the fundamental cell of the periodic structure.

The solution proposed in Fig. 5.3 was generated by analogy, using the "double curved beam" structure as guide. A computational strategy is being sought that may allow to synthesize other such structures *and* meet some prescribed performance specification, e.g., match certain desirable features of a strain energy curve or a load deformation diagram. One such strategy based on topology optimization is discussed in the following sections.

5.3. The Analysis Model

The structure is analyzed using non-linear, corotational Timoshenko beam elements and a total Lagrangian formulation (a detailed formulation is given in Crisfield (1991), p219.) The analysis is quasi static and all inertial forces are ignored. At equilibrium,

$$\mathbf{g}(\mathbf{x}) = \mathbf{f}_{\text{int}}(\mathbf{x}) - \mathbf{f}_{ext}(t) = 0 \tag{5.3.1}$$

where

$$\mathbf{f}_{\text{int}}(\mathbf{x}) = \frac{\partial \Lambda}{\partial \mathbf{x}} \tag{5.3.2}$$

is the internal force, Λ is the total strain energy, $\mathbf{x}(t) \in \Re^n$ represents the configuration of the structure at time t under an external force $\mathbf{f}_{ext}(t)$ and n is the total number of degrees of freedom. A Newton-Raphson-like scheme is used to find a solution to (1). At the i-th iteration step the scheme produces

$$\mathbf{x}_{i+1}^{t} = \mathbf{x}_{i}^{t} - \left[\frac{\partial \mathbf{g}}{\partial \mathbf{x}}\right]_{\mathbf{x}=\mathbf{x}_{i}^{t}}^{-1} \mathbf{g}(\mathbf{x}_{i}^{t}) \qquad (5.3.3)$$

where $\mathbf{x}_{0}^{t+1} = \mathbf{x}^{t}$. In (5.3.3), $\partial \mathbf{g}/\partial \mathbf{x}$ is the tangent stiffness matrix. $\mathbf{x}^{t}$ represents the solution to the equilibrium equation (1) at time t .

Simulation results were validated using the commercial finite element package ABAQUS using the element 'b21', a beam element. As the model consists only of beam elements, joint rigidity may be overestimated, when compared to a full 2D elasticity model (e.g., one that uses quadrilateral finite elements). This drawback can be overcome by the modulation of the cross-sectional area, as discussed in the next section.

5.4. Optimization of the Topology

5.4.1 The ground structure and design variables

The formulation used here is similar to a classical ground structure approach in truss topology optimization (e.g., Dorn et al (1964) or Bendsøe et al (1994)). In a typical ground structure approach, design variables are cross-sectional areas A_{α} of each member (i.e. bar) in the ground structure, where $\alpha = 1, 2, \ldots, n_b$ and n_b is the total number of members in the ground structure. The ground structure contains enough members and possible connections to include, as a subset, a reasonable number of design alternatives. The moment of inertia of the beam I_α is assumed to be proportional to the square of the beam's cross-sectional area, i.e.,

$$I_\alpha = cA_\alpha^2 \qquad c>0 \tag{5.4.1}$$

A ground structure made up of beams of uniform cross section will not have enough flexibility to produce a bistable structure (Qiu et. al. (2004)). In order to provide joints with flexibility, a measure of compliance is achieved by "modulating" the cross section of elements along their axis, reducing the cross sectional area of elements near a flexible joint (alternatively, a soft rubber-like material may be used to model hinges, as illustrated in Section 5.5). In the present work, each member of the ground structure is divided into three regions, as shown in Fig. 4.1. The two end regions are identical in length (L_1) and cross-sectional area (A^1). The middle region has length L_2 and cross-sectional area A^2. In a ground structure, A^1 is an independent (design) variable; A^1 is allowed to take one of *three* possible values, corresponding to: member removed (A^1=0), member is a snap-beam ($A^1 = A^l$) or member is a support beam ($A^1 = A^u$), where $0 < A^l < A^u$ and A^l and A^u are prescribed values. A^2 is a dependent variable, set to 0 (member removed) whenever A^1=0 and set to A^u otherwise. This choice is motivated by the example bistable structure introduced in Section 5.2 which was constructed using only two types of beams: a more compliant one, which snaps and is the source of the bistability, and a stiffer one, which provides support to members of the first type.

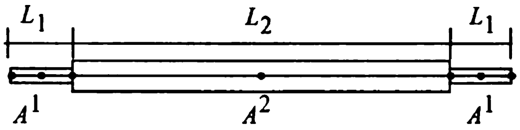

Figure 5.7. A member (bar) of the ground structure

Based on the previous discussion, the cross-sectional areas A_α of the end regions of each member α in the ground structure, $\alpha = 1, 2, ..., n_b$, are selected as design variables in this problem and let A_α take values in $\{0, A^l, A^u\}$.

5.4.2 The objective function

The objective function used here is built around characteristic points of the load displacement curve. A typical curve is shown in Fig. 5.8. Points D and F correspond to values where the load just reaches the critical value that causes snap-through. Under external loading, B and H are points where the structure settles just after the snap through. Starting from the first stable configuration (point C), when the bistable structure is loaded past the critical level for snap-through, the state of structure follows the path C-D-H-I, by-passing the segment D-E-F-G-H along which the internal force in the structure cannot equilibrate the external load. When the structure is unloaded after reaching I, it settles in the second stable configuration at G, after following the path I-H-G. Under similar loading in the reverse direction, the structure follows the path G-F-B-A, now by-passing the segment F-E-D-C-B.

An objective function is now proposed, which can be used to evaluate the quality of alternative designs. Here a very simple objective function is used, focusing primarily on the difference between the two stable configurations, roughly, a measure of the magnitude of the snap-through jump in a simple snap-through structure. When $\mathbf{x}^C$ and $\mathbf{x}^G$ are two stable configurations of a simple snap-through structure, this measure is

$$\phi = \| \mathbf{x}^C - \mathbf{x}^G \|^{1/2} \tag{5.4.2}$$

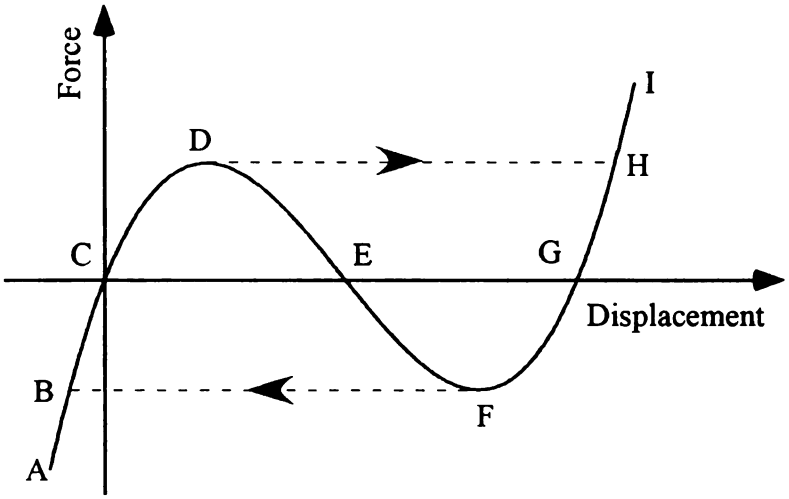

Figure 5.8. Typical force-displacement diagram for a bistable structure

In more complex structures, the *direction* of the snap-through may play a role and to account for this, the objective function is defined as

$$\phi = \sqrt{(\mathbf{x}^C - \mathbf{x}^G)^T \mathbf{W} (\mathbf{x}^C - \mathbf{x}^G)} \tag{5.4.3}$$

where **W** is a diagonal, square, semidefinite matrix. Finally, most subsets of the ground structure will not be bistable and in fact, the majority of such subsets will not even be properly formed structures (e.g., they may be disjoined or not properly supported). For any such structure, ϕ is set to zero. Thus, the goal achieved by maximizing ϕ is simply to find *any* one bistable structure contained in the ground structure. The function ϕ is the objective function to be maximized in the optimization problem, stated in the following section.

Loading A typical external loading is given by

$$\mathbf{f}_{ext}(t) = \tau(t)\mathbf{f}^{o} \tag{5.4.4}$$

where $\tau(t)$ is as shown in Fig. 5.9. $\mathbf{f}^{o}$ is a prescribed maximum external force and t is a pseudo time. The time discretization is chosen to suit the finite element analysis. The goal is to obtain a bistable structure with a critical load less than $\mathbf{f}^{o}$. A displacement driven problem (one where the displacement at the input port is prescribed) is solved to capture the segments D-E-F-G-H and F-E-D-C-B of the load-displacement curve (Fig. 5.8), which are by-passed in a load driven problem. In that case the displacement x_{in} at the input port(s) is prescribed by

$$x_{in}(t) = \tau(t)x_0 \tag{5.4.5}$$

where x_0 is a reference displacement amplitude. The force in the ordinate of the force-displacement curve corresponds to the corresponding reaction force.

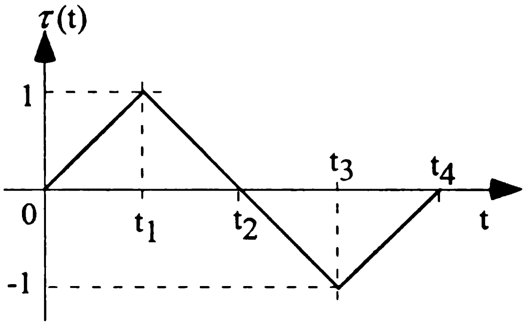

Figure 5.9. The external load factor as a function of time

5.4.3 The optimization problem

The optimization problem is formally stated as:

Find $\mathbf{A} = \{A_1, A_2, \ldots, A_{n_b}\} \in \{0, A^l, A^u\}^{nb}$ that

$$\text{maximize } \phi = \sqrt{(\mathbf{x}^C - \mathbf{x}^G)^T \mathbf{W} (\mathbf{x}^C - \mathbf{x}^G)}$$

subject to (5.4.6)

$$\sum_{\alpha=1}^{n_b} \chi(A_\alpha) \le n_{MAX}$$

where

$$\chi(A_\alpha) = \begin{cases} 0 & \text{for } A_\alpha = 0 \\ 1 & \text{for } A_\alpha > 0 \end{cases}$$

Data for this problem are:

A^l	cross-sectional area of the thin beams
A^u	cross-sectional area of the thick beams
n_{MAX}	the maximum number of members allowed

W prescribed weight factors used to emphasize a given snap-through direction

5.4.4 The solution scheme

Problem (5.4.6) is treated as a combinatorial optimization problem and solved using a genetic algorithm (GA). However, since many, if not most of the subsets of the ground structure are not bistable and may not even be well formed structures, a significant portion of the design space has objective function values $\phi=0$. In order to provide for a meaningful evaluation of the merit of such structures, the original objective in (5.4.6) is replaced by the *minimization* of the following merit function in the GA:

$$f=-(w\phi)^2+\psi \tag{5.4.7}$$

In (5.4.7)

$$\psi=\psi_1+\psi_2+\psi_3+\psi_4 \tag{5.4.8}$$

is a penalty function with entries ψ_1, ψ_2, ψ_3, and ψ_4 designed to provide all sub-sets of the ground structure with a meaningful merit function value (even sub-sets that are not well formed structures). The (constant) scaling factor w is scaled so that $w\phi\approx 1$, as are ψ_1, ψ_2, ψ_3, and ψ_4. These functions are defined as follows:

(1) ψ_1 penalizes structures that do not have any structural members at the prescribed loading ports (nodes). ψ_1 is defined as

$$\psi_1 = \frac{1}{\delta_{\max}} \sum_{j=1}^{nf} \delta_j \tag{5.4.9}$$

where δ_j is the distance between the structure and the j-th loading port and $\delta_{\max}$ is the maximum distance between two nodes in the structure.

(2) ψ_2 penalizes structures with too many bars. ψ_2 is defined as

$$\psi_2 = \begin{cases} \dfrac{(n_a - n_{MAX})}{(n_t - n_{MAX})} & \text{if} \quad n_a > n_{MAX} \\ 0 & \text{if} \quad n_a \le n_{MAX} \end{cases} \tag{5.4.10}$$

where

$$n_a = \sum_{\alpha=1}^{\mathrm{n_b}} \chi(A_\alpha) \tag{5.4.11}$$

is the actual number of members in the structure and $n_t > n_{MAX}$ is a prescribed number used to adjust the slope of the penalty and selected to keep the value of ψ_2 near 1 (e.g., $n_t = 2\, n_{MAX}$). A lower (or higher) n_t increases (or decreases) the relative weight of ψ_2 with respect to the other ψ_i s.

(3) ψ_3 penalizes disjoint structures. ψ_3 is defined as

$$\psi_3 = \frac{N_s}{N_t} \tag{5.4.12}$$

where N_s is the number of disjoint sub-structures and N_t is a prescribed scaling factor (e.g., N_t=2). To measure N_s the structure is represented as an undirected graph. N_s is the number of components of the graph.

(4) ψ_4 penalizes structures that are not properly supported i.e. structures that may undergo rigid-body motions. ψ_4 is defined as

$$\psi_4 = N_x + N_y + N_\theta \tag{5.4.13}$$

where N_x=0 if the structure's rigid-body motion in the x direction is constrained, N_x=1 otherwise, and similarly for N_y and N_θ. Only a straight forward evaluation is made, simple enough to rule out designs with little computation. For instance, N_x is set to 0 if a node connected to the structure is on an x- constrained boundary.

5.5. Examples

5.5.1 Example 1

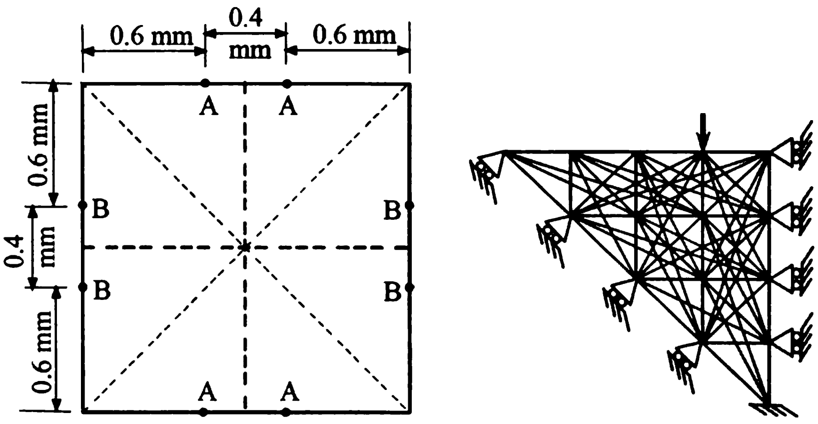

(a) (b)

Figure 5.10. Example 1. The package space (a) and corresponding ground structure (b) with dimensions and boundary conditions

In this example the goal is to design a two-dimensional bistable structure that will operate, loaded vertically at port A and horizontally at port B and fit within a 1.6mm x 1.6mm package space, as shown in Fig. 5.10. This space is partitioned into 8 triangles, whose boundaries are marked with dashed lines in the figure. The structure is assumed to be symmetric about these lines. The ground structure is laid on one of these triangles and the appropriate boundary conditions are applied to enforce symmetry (Fig. 5.10(b)). Loads $F=6\tau(t)$ in the range ±6 mN are applied at positions A and B. The function $\tau(t)$ is as in Fig. 5.9. All entries in the weight matrix **W** are zero except $W_{mm}=1$, where m is the degree-of-freedom associated with the load F. This means that snap-through in the direction of the external load is needed to be maximized.

The total number of bars in the ground structure (n_b) is 62. In accordance with Section 5.4.1, every member is discretized into three regions with lengths L_2=6L_1 and every region is further discretized into two finite elements (Fig. 5.7). A solution is allowed a maximum of n_{MAX}=8 bars, each using one of two cross section areas: A^l=10^{-4} mm^2 and A^u =10^{-3} mm^2. The Young's modulus and Poisson's ratio are 1380 MPa and 0.3, respectively.

The ground structure depicted in Fig. 5.10(b) admits, as one solution, the topology of the bistable structure introduced Section 5.2 (Fig. 5.3), the *reference* structure. That structure has an objective function ϕ=0.3674 (mm) (this value is used to scale the objective function f in (5.4.7) and defines w=1/0.3674=2.7218). The structure has the force displacement diagram shown in Fig. 5.11. The switching force (the force that causes snap-through) for this mechanism is approximately -3.5 mN in the forward direction and 1.8 mN in the backward direction.

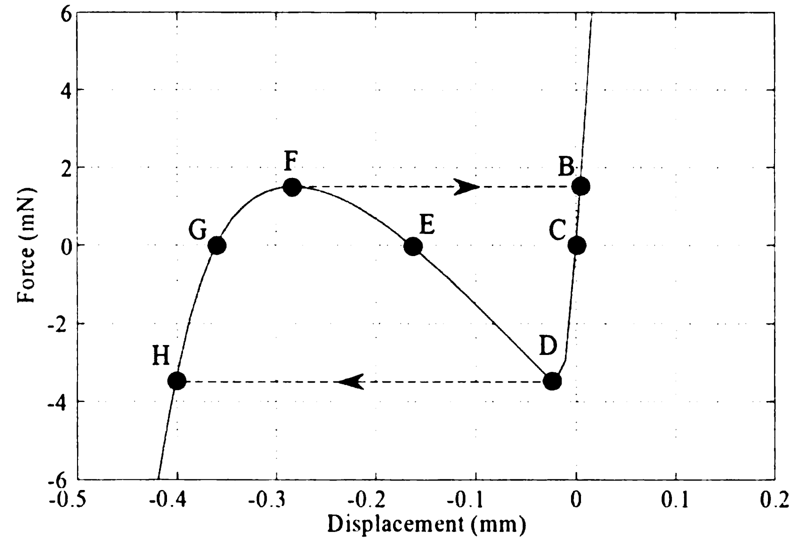

Figure 5.11. The force-displacement diagram for the reference structure (Fig. 5.3)

Now a GA is used to find other solutions. The GA starts with a population of 100 randomly generated designs, which are sorted based on their merit function (*f*) values. Following a standard GA procedure, every individual is assigned a scaled merit function value depending on its position. An elitist strategy with generation gap of 60% is used. The best 40% of the solutions in the population are carried forward to the next generation and the remaining 60% is produced through crossover among the parents, selected probabilistically from within the current generation. The probabilistic selection of parents for crossover is based on the standard "roulette wheel" mechanism, where the probability of selection of an individual for the crossover is directly proportional to its fitness value. The mutation rate used is 10%.

The process of fitness assignment, crossover, mutation etc. was repeated for 500 generations, which resulted in the solution shown in Fig. 5.12. The objective function value for this structure is ϕ=0.3688 (mm), with penalty function ψ=0, i.e., only slightly better than the structure in Fig. 5.3. The corresponding force displacement diagram (obtained with the prescribed input displacement) is shown in Fig. 5.13. The switching force is approximately -1.8 mN in one direction (forward) and 0.9 mN in the other (backward).

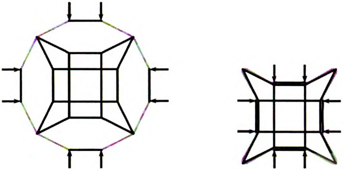

(a) (b)

Figure 5.12. Example 1. Bistable structure obtained by the GA (a) first stable configuration (b) second stable configuration

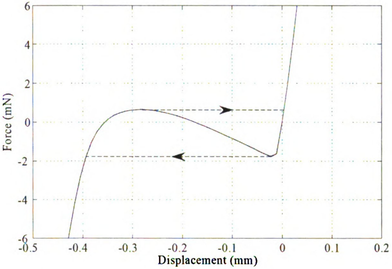

Figure 5.13. The force-displacement diagram for the structure in Fig. 5.12.

Another solution with essentially the same objective function value (and ψ=0) is shown in Fig. 5.14. In this structure, however, several members overlap. The present modeling does not account for interference or contact between members, as the structure switches from one configuration to the other. This is acknowledged as a drawback, unfortunately one that is difficult to overcome. This will be discussed further in the next section.

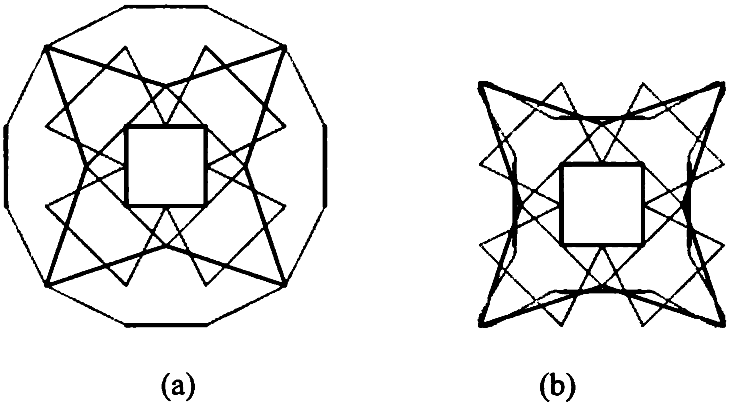

Figure 5.14. Example 1. Another bistable structure (a) first stable configuration (b) second stable configuration

Solutions in Figs. 5.12 and 5.14 show that the deformation in the hinges can be quite large, raising questions regarding the manufacturability of solutions modeled using these ideas. Some of these concerns may be alleviated by using a rubber-like material (polyurethane elastomer) at the hinges. The maximum allowable normal stress in this material is about 45 MPa, which corresponds to about 440% elongation at break. For instance, returning to the structure shown in Fig. 5.14, one can use the soft material in the two end sections of each hinged member (shown light gray in the figure) and keep the area constant at A^u over the length of the member. This would result in the load-displacement curve shown in Fig. 5.15. Note that using the rubber-like material does not change the size of the jump between stable configurations significantly (but it does change the magnitude of the actuating force required to switch configurations). The maximum stress in the elastomer is 25.5 MPa, within the allowable limit for the material. This suggests that using a combination of materials that includes softer materials near the hinges may result in concepts that could be manufactured more easily.

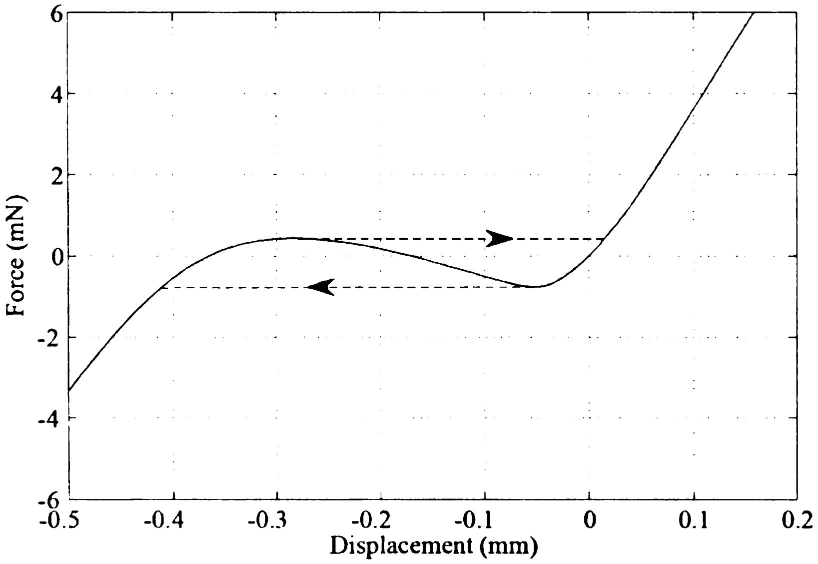

Figure 5.15. Force-displacement diagram for the bistable structure obtained by the GA

All the solutions shown here are obtained from the same run of the GA. Figure 5.16 shows the history of the best GA merit function (*f*) value for a generation. At generation 0, i.e. in the randomly generated population, the best merit function value is f=0.1250. At the end of 500th generation, the best merit function value is f=-1.008. The finite element analysis and optimization procedures were implemented on a MATLAB program running on a Pentium 4 machine with 2.8 GHz clock speed, 496 MB RAM and Windows XP operating system. 93 hours were spent in running the optimization program for 500 generations.

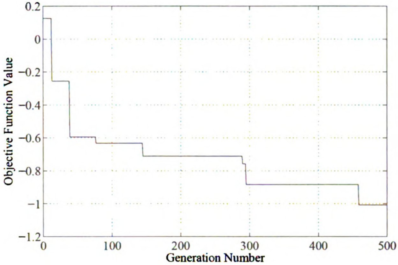

Figure 5.16. History of the best GA merit function value *f*

5.5.2 Example 2

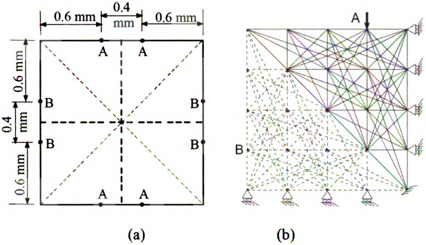

Figure 5.17. Example 2. The package space (a) and corresponding ground structure (b) with dimensions and boundary conditions

The package space in this example is the same as that in Example 1. The goal is to maximize the snap-through at ports B in the horizontal direction, when the structure is loaded (only) at ports A, in the vertical direction.

A load F in the range of ±4 mN is applied at each loading port. With the given loading, the structure is assumed to be symmetric about the horizontal and vertical centerlines, which are shown as thick dashed lines in Fig. 5.17(a). In addition, the structure is desired to be orthotropic. For this reason, the layout is assumed to be symmetric about the diagonals, shown as thin dashed lines in Fig. 5.17(a). Accordingly, the package space is partitioned into 8 equal triangles, whose boundaries are marked with dashed lines in the figure. The ground structure is laid on one of these triangles. The ground structure is the same as that in Example 1, as are other details of the discretization. It should be noted, however, that since the loading is symmetric only about the centerlines, one quarter of the structure is analyzed (Fig. 5.17(b)). Appropriate boundary conditions are applied to enforce symmetry, as shown in the figure.

In this example all entries in the weight matrix **W** are zero except W_{pp}=1, where p is the degree-of-freedom associated with the horizontal motion of the output port B. The GA parameters such as population size, mutation rate and generation gap have been kept same as that in Example 1. The GA was run for 500 generations, after which a solution is obtained with merit function value f= -0.10614, ϕ= 0.1197 (mm) and ψ=0. The solution is shown in Fig. 5.18(a). Fig. 5.18(b) shows the corresponding second stable configuration of the structure.

The external force at input port A is plotted versus the displacement at the output port B in Fig. 5.19 (obtained from a displacement-driven analysis). The maximum switching forces are approximately -1.9 mN in the forward direction and 0.5 mN in the backward direction. The maximum switching force in the backward direction is small compared to that in the forward direction. While the present model does not penalize this difference, control of the relative magnitudes of the switching forces can be accommodated in the GA formulation by simply adding an additional penalty term to the objective function.

In Fig. 5.19 it can be noticed that the displacement at the output port B does not change sign through the input cycle, i.e., as $\tau(t)$ (Fig. 5.9) goes through one full cycle. The force-displacement curve is nearly vertical in the neighborhood of the first stable configuration, suggesting that in this region the output port remains nearly stationary for a small range of inputs, a behavior reminiscent of a Poisson's ratio zero material. This is of course not true in a neighborhood of the second stable configuration, where a small external force applied at the input port makes the output port B move a finite distance.

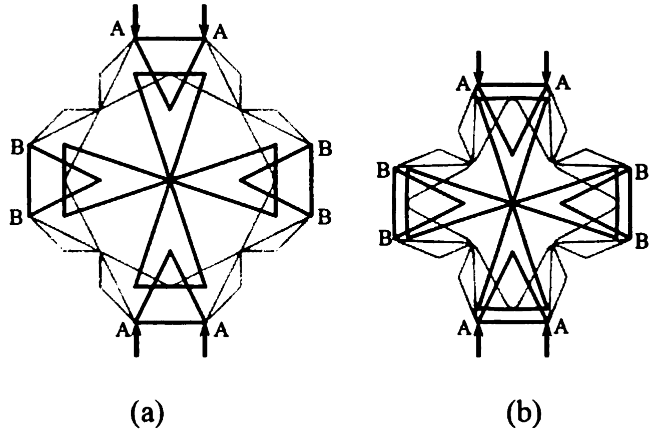

(a) (b)

Figure 5.18. Example 2. Bistable structure obtained by the GA (a) first stable configuration, (b) second stable configuration

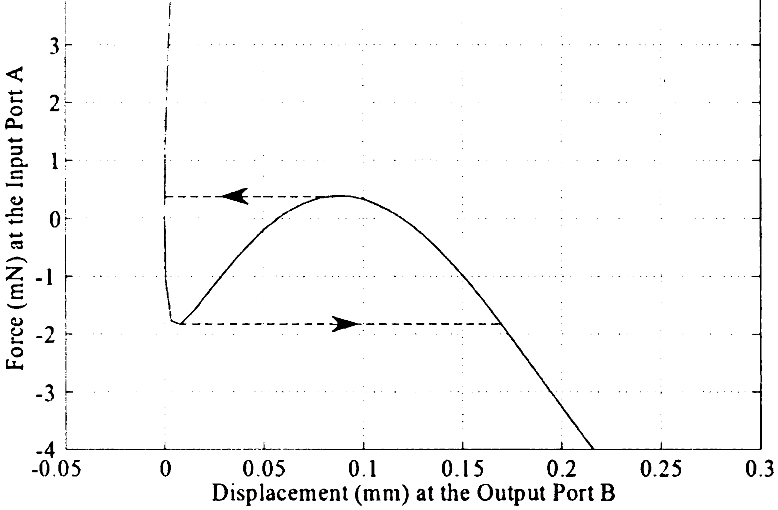

Figure 5.19. Example 2. Plot of the internal force at the input port A versus the displacement at the output port B.

Finally, again it can be observed in the solution proposed to Example 2 that several members overlap as the structure moves from one configuration to the other, signaling interference. In this problem, however, no solution was found where interference did not occur. One way to address this problem is to cast the problem in three-dimensions, allowing at least some members to have a small curvature out of the plane, to avoid interference. This can be appreciated in Fig. 5.20, which shows quarter sections of the solution in its two stable configurations. Here, as in all previous solutions, one can identify three main sub-structures. One sub-structure, formed by stiff members, remains fixed in space throughout the deformation and acts as support to the rest of the structure. A second sub-structure moves essentially as a rigid body and is also formed by stiff members. This sub-structure typically receives input from or transfers output to neighboring components. The third sub-structure connects the previous two and is formed by compliant members. This sub-structure is primarily responsible for the motion of the mechanism. In most cases interference is avoided if these three components are in different planes of the structure. This qualitative description provides hints on how to actually implement these solutions. Naturally, this is not sufficient in many applications, e.g., in very small scale designs where a layered solution is not realistic. In such cases a full implementation of a contact detection scheme that rejects solutions where interference is detected would be necessary.

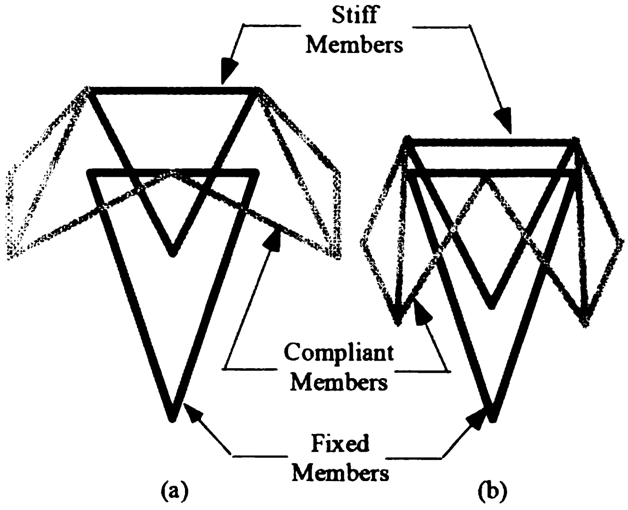

Figure 5.20. Detail of the solution of Example 2. (a) First stable configuration (b) Second stable configuration.

5.6. Rubber Model

As also discussed in Section 5.5.1, deformation in the hinges can be quite large, raising questions regarding the manufacturability of solutions modeled using two cross-sectional areas. Some of these concerns may be alleviated by using a rubber-like material (e.g., polyurethane elastomer) at the hinges. Using a combination of materials that includes softer materials near the hinges may result in concepts that could be manufactured more easily. Some works have been carried out in this direction and presented next.

As earlier, every bar in the ground structure is divided into two kinds of regions – shown as dark and light gray regions in Fig. 5.21. Material properties for the region shown in light gray are variable, taking three possible values, namely, values corresponding to 'no material', a 'soft' material and a 'hard' material. The region shown dark is made from either 'no material' or the 'hard' material.

Figure 5.21. Rubber model: A member (bar) of the ground structure

Here the soft material is a compliant, rubber-like material, e.g. natural rubber, silicone rubber or a polyurethane elastomer. The hard material is relatively stiff and approximately linear material, e.g. polypropylene.

Material properties are characterized by – (a) the normal stress (σ) vs. normal strain (ε) relationship and (b) the shear stress (τ) *vs.* shear strain (γ) relationship for the material. Figure 5.22 shows a representative plot of σ *vs.* ε in a soft material, viz. polyurethane elastomer. The τ *vs.* γrelationship for both hard and soft material is assumed to be linear.

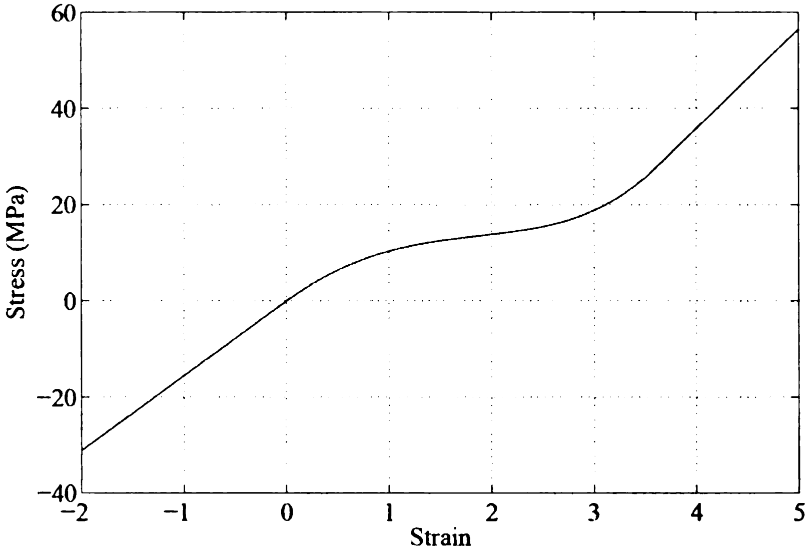

Figure 5.22. Prescribed normal stress as a function of normal strain in the soft material

The material and layout of the structure are controlled by two binary design variables for each bar α, labeled ρ_α and μ_α. Variable ρ_α controls the layout of the structure: $\rho_\alpha = 1$ means bar α is present, $\rho_\alpha = 0$ means bar α is removed. When a bar is present, its material is controlled by variable μ_α. $\mu_\alpha = 1$ indicates that the light gray regions of bar α are made of the soft material, i.e. α bar is hinged at both ends. $\mu_\alpha = 0$ means that bar α is made of the hard material. Thus, the normal stress in the light gray region of bar α may be written as

$$\sigma_\alpha^{gray}(\rho_\alpha, \mu_\alpha, \varepsilon) = \rho_\alpha \left(\mu_\alpha \sigma^1(\varepsilon) + (1 - \mu_\alpha)\sigma^2(\varepsilon) \right) \qquad (5.6.1)$$

where the superscripts (1) and (2) refer to properties of the soft and hard material, respectively. Similarly, the shear stress in the light gray region of bar α may be written as

$$\tau_{\alpha}^{gray}(\rho_{\alpha},\mu_{\alpha},\gamma)=\rho_{\alpha}\left(\mu_{\alpha}\tau^{1}(\gamma)+(1-\mu_{\alpha})\tau^{2}(\gamma)\right) \tag{5.6.2}$$

The normal stress in the dark region of bar α may be expressed as

$$\sigma_{\alpha}^{dark}(\rho_{\alpha},\varepsilon)=\rho_{\alpha}\sigma^{2}(\varepsilon) \tag{5.6.3}$$

while the shear stress in the dark region of bar α is

$$\tau_{\alpha}^{dark}(\rho_{\alpha},\gamma)=\rho_{\alpha}\tau^{2}(\gamma) \tag{5.6.4}$$

A scaled arc-length method (Al-Rasby (1991), Bruns et. Al. (2002)) has been used for the solution of the non-linear equations. Arc length method is suitable for analyzing structures undergoing instability (snap through or buckling). Such instability is typically undesirable structures (e.g. in Neves (1995)), whereas such instability is desirable for bistable structures.

5.6.1 New optimization problem

The new optimization problem is formally written as

Find $\boldsymbol{\rho} = \{\rho_1, \rho_2, ..., \rho_{n_b}\} \in \{0,1\}^{nb}$, $\boldsymbol{\mu} = \{\mu_1, \mu_2, ..., \mu_{n_b}\} \in \{0,1\}^{nb}$ that

$$\text{maximize } \phi(\boldsymbol{\rho}, \boldsymbol{\mu}) = (\mathbf{x}^C - \mathbf{x}^G)^T \mathbf{W} (\mathbf{x}^C - \mathbf{x}^G) \tag{5.6.5}$$

subject to

$$\sum_{\alpha=1}^{n_b} \rho_\alpha \le n_{MAX}$$

5.6.2 Example

The example in Section 5.5.1 is solved using the Rubber Model. The cross-sectional area is kept constant at $2\text{x}10^{-3}$ mm^2 over the length of every member. The hard material is polypropylene with Young's modulus 1380 MPa and Poisson's ratio 0.3. The soft material is assumed to be linear in shear with shear modulus 5.2 MPa. The σ-ε plot for the soft material is given in Fig. 5.22.

The solution obtained by the GA is shown along with its second stable configuration in Fig. 5.23. The objective function (ϕ) value for this structure is 0.3629 (mm), or merit function f is -0.9758 with penalty function ψ=0. The corresponding force displacement diagram is shown in Fig. 5.24. The critical force required for the snap through is approximately 5.5 mN in one direction (forward) and 3.0 mN in the other (backward).

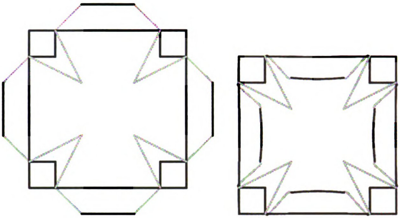

(a) (b)

Figure 5.23. Bistable structure obtained by the GA (a) first stable configuration (b) second stable configuration

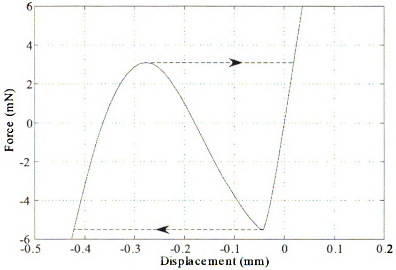

Figure 5.24. The force-displacement diagram for the structure in Fig. 5.23

It can be noticed that the structures shown in Figs. 5.12, 5.14 and 5.23 are the same type as they essentially only have the 3-beam segments on peripheral as bistable elements. In fact, essentially all solutions found work on a similar principle: they exploit the bistability of simple two- or three- bar segments placed strategically around a supporting frame. This fact can be exploited to develop different and perhaps more efficient design strategies. For example, with this insight one could devise a different algorithm, perhaps one in which the design space is represented not by means of a ground structure, but instead by a vocabulary that involves only two bar sub-structures and structures to support them (and a grammar that works on connecting each piece to each other and to the external loads). This new approach is studied in Prasad and Diaz (2005).

CONCLUSIONS AND FUTURE WORK

This work investigates methodologies to design a structure or material whose dynamic modulus would decrease with forcing frequency. The motivation to synthesize such structures or materials is their applicability in vibration isolation devices. The works of Wang and Lakes (2004a and 2004a), which used inclusions of an elastic negative-stiffness phase in the matrix of a viscoelastic metal to achieve extremal materials, were found be relevant and useful for the present work. In order to study the stability of the composite material, the authors analyzed an equivalent lumped system and found that the lumped system can also soften with frequency for some parameters (spring stiffness, damping coefficients in the lumped system); however, the structure was not stable for the parameters leading to the softening. Nevertheless, the works of Wang and Lakes (2004a and 2004b) gave inspiration to use negative stiffness inclusions. The question was how to get stable frequency-induced softening in a composite having a negative stiffness component and the present work addresses that question.

The contribution of this work starts with the idea that a composite material having a negative stiffness component can be used as a 'smart' vibration isolation device. Chapter 2 presents a model of a material that exhibits frequency-induced softening. The model is 2D and based on a periodic mixture of two material phases: A (matrix phase) and B (inclusion phase). In contrast to Wang and Lakes (2004a and 2004b) where phases A and B are viscoelastic and elastic respectively, the two phases here are elastic and viscoelastic respectively. Later desirable results were obtained even when both the two phases are viscoelastic. The present work thus contributes in finding alternatives to the phases used by Lakes and his coworkers.

The two-phase composite material was approximated as a one dimensional mechanical model in accordance with Fujino et al. (1964) and Marinov (1978). The one-dimensional lumped model was analyzed for frequency-induced softening and stability. The analysis determined parameters for stable softening and forms a part of the contribution of this work. The parameters of the 1D mechanical model that showed stable softening were extended back to construct the corresponding 2D composite model. The stability of the 2D composite model was further reviewed as the stability criteria for the 1D mechanical model may not be sufficient to ensure stability of the 2D composite. It was found that the negative stiffness phase itself needed to be made stable as an inclusion before the stability of the whole composite is investigated. Studies revealed that the simultaneous softening and stability are achievable if phase B itself is a small scale mixture of two constituents, one elastic (B_2) and the other one with negative stiffness (B_1). The idea of stabilizing the negative stiffness phase by the rank-1 layering of the two constituents is a contribution of this work. It should be noted, however, that while the stability of the mixture was verified against *certain* modes of instability, one cannot say for sure that the material is stable with regard to all possible modes of instability. Further analysis may determine that additional conditions may be required. A full answer can be obtained only through experimentation.

To realize the negative stiffness material B_1, a lumped system is proposed to be made of negative stiffness springs, typical positive-stiffness springs and dampers. A layered mixture of this lumped system (phase B_1) and a typical elastic material (phase B_2) may be used as the inclusion phase B; however, physical realization of such inclusion phase may be difficult. As an alternative to the layered phase B, therefore, a lumped system is built for phase B which is stable as an inclusion. The design of lumped systems (B_1 and B) and their analysis to determine the average elastic properties and estimate stability are part of the contribution of this work.

Chapter 3 presented examples of the composites that exhibit frequency induced softening. Transmissibility analysis for the composites was carried out. The vibration isolation performance for these composites (A-B mixture) was found to be better than that of the matrix material (A) alone.

Phase B is not isotropic and therefore mixing phases A and B may result in a material that is not isotropic either. In practice one may be interested only in isotropic materials and therefore the micro-geometry of the mixture of A and B must be designed so that the mixture is isotropic. This has been done in chapter 4 by casting the problem as an inverse homogenization problem (as discussed e.g. in Sigmund (1995)). This methodology has been used to tailor the material tensor to desired specifications, by re-adjusting the shape of the inclusion of B inside A. The designed materials closely match the target elastic properties. The methodology developed in that chapter differs from a typical material design problem and may be considered as a major contribution. Using positive definiteness of the elastic tensor as a constraint to maintain stability is a novel idea emerged from the present work. The extension of the objective function in Diaz and Benard (2003) to suit viscoelastic materials is also new.

Once the layout of the composite material is available, the next step is to actually build the composite. The first task in that direction would be to build the inclusion phase B. In chapter 2, the negative stiffness (in phase B) is proposed to be realized by using bistable structures. The realization of phase B is proposed in two steps – (i) build a two-dimensional (tileable) bistable structure and (ii) interconnect the 2D bistable structures using viscoelastic blocks. While chapter 5 addresses the first step, the second step is left as a future work. The model of tileable bistable structure developed in chapter 5 is quite simple. It ignores important constraints, such as interference, contact between members and stress constraints. The simplifications introduced were necessary to reduce the computational burden associated with the analysis and, in particular, with the use of genetic algorithms. However, in spite of its simplicity, the approach results in a useful tool to explore concepts in design of bistable, periodic structures. The main contributions in this chapter include the idea of making a tileable bistable structure, the idea of achieving bistability by making beams flexible at the ends (using thinner area or softer material) and formulation of the whole optimization problem (including the design of the objective function as well as the constraints to avoid the invalid structures). Further studies for this part of work should include a better objective function, capable of providing sensitivity information even for the monostable designs; the computation of analytical sensitivity information, consistent with more efficient, gradient based optimization algorithms; stress and interference constraints; and more refined analysis models (e.g., two-dimensional elasticity instead of beam models) that may reflect the true behavior of compliant structures more accurately.

To sum up all the chapters, it can be said that the concept presented in this work is attractive and may provide indications on what avenues to pursue in the future. A direction that seems perhaps more attractive involves the realization of the negative stiffness inclusion by means of a bistable structure inside the composite. This could be accomplished perhaps by pre-stressing one of the constituents of the composite to a post-buckled state. Regardless, the current state of the work is only theoretical; relevant experimental work should be pursued in future before one can suggest what the most potentially rewarding direction to pursue should be in order to actually realize a material with the desired properties.

REFERENCE

Al-Rasby, S.N., 1991, "Solution Techniques in Nonlinear Structural Analysis," Computers and Structures, Vol. 40, No. 4, pp. 985-993.

Ananthasuresh, G.K. and Kota, S., 1995, "Designing Compliant Mechanisms," Mechanical Engineering, Vol. 117, No. 11, pp. 93-96.

Bendsøe, M., Ben Tal, A. and Zowe, J., 1994, "Optimization methods for truss geometry and topology design," Structural Optimization, Vol. 7, pp. 141-159.

Bendsøe, M.P. and Kikuchi, N., 1988, "Generating optimal topologies in structural design using a homogenization method," Computer Methods in Applied Mechanics and Engineering 1988, Vol. 71, pp. 197-224.

Bendsøe, M.P. and Sigmund, O., 2003, "Topology Optimization: Theory, Methods and Applications," Springer, New York.

Bensoussan, A., Lions, J.L., and Papanicolau, G., 1978, "Asymptotic Analysis for Periodic Structures," North-Holland, Amsterdam.

Bruns, T. E., Sigmund, O. and Tortorelli, D. A., 2002, "Numerical methods for the topology optimization of structures that exhibit snap-through," International Journal for Numerical Methods in Engineering, Vol. 55, pp. 1215-1237.

Bruns, T.E. and Tortorelli, D.A., 2001, "Topology optimization of nonlinear elastic structures and compliant mechanisms," Computer Methods in Applied Mechanics and Engineering, Vol. 190(26-27), pp. 3443–3459.

Cherkaev, A.V. and Gibiansky, L.V., 1993, "Coupled estimates for the bulk and shear moduli of a two-dimensional isotropic elastic composite," Journal of the Mechanics and Physics of Solids, Vol. 41 (5), pp. 937-980.

Crisfield, M.A., 1991, Non-linear Finite Element Analysis of Solids and Structures, Vol. 1, Wiley, Chichester.

Diaz, A. R. and Benard, A., 2003, "Designing materials with prescribed elastic properties using polygonal cells," International Journal for Numerical Methods in Engineering, Vol. 57 (3), pp. 301-314.

Dorn, W. C., Gomory, R.E. and Greenberg, H.J., 1964, "Automatic design of optimal structures," Journal de Mècanique, Vol. 3, pp. 25-52.

Flugge, W., 1967, "Viscoelasticity," Blaisdell Publishing Company, Waltham.

Frecker, M. I., Ananthasuresh, G. K., Nishiwaki, S., Kikuchi, N. and Kota, S., 1997, "Topological synthesis of compliant mechanisms using multi-criteria optimization," Journal of Mechanical Design, Vol. 119 (2), pp. 238-245.

Fujino, K., Ogawa, Y., and Kawai, H., 1964, "Generalized model representation relating the degree of mixing to the rheological behavior of a mechanical mixture of two polymer components," Journal of Applied Polymer Science, Vol. 8(5) , pp. 2147 – 2161.

Guest, J., Prevost, J. and Belytschko, T., 2004, "Achieving minimum length scale in topology optimization using nodal design variables and projection functions," International Journal for Numerical Methods in Engineering, Vol. 61(2), pp. 238–254.

Gibiansky, L.V. and Milton, G.W., 1993, "On the effective viscoelastic moduli of two-phase media. I. Rigorous bounds on the complex bulk modulus," Proc. R. Soc. London A, Vol. 440, pp. 163–188.

Gibiansky, L.V., Milton, G.W. and Berryman, J.G., 1999, "On the effective viscoelastic moduli of two-phase media. III. Rigorous bounds on the complex shear modulus in two dimensions," Proc. R. Soc. London A, Vol. 455, pp. 2117–2149.

Guedes, J.M. and Kikuchi, N., 1990, "Preprocessing and postprocessing for materials based on the homogenization method with adaptive finite element methods," Computer Methods in Applied Mechanics and Engineering, Vol. 83, pp. 143–198.

Haddad, Y.M., 1995, "Viscoelasticity of engineering materials," Chapman & Hall, London.

Hassani, B. and Hinton, E., 1999, Homogenization and Structural Topology Optimization, Springer-Verlag London.

Hashin, Z. and Shtrikman, S., 1963, "A variational approach to the theory of the elastic behaviour of multiphase materials," Journal of the Mechanics and Physics of Solids, Vol. 11, pp. 127-140.

Herrera, I. and Gurtin, M.E., 1965, "A correspondence principle for viscoelastic wave propagation," Quarterly of applied mathematics, Vol. 22(4), pp. 360-364.

Howell, L.L., 2001, Compliant Mechanisms, John Wiley and Sons, New York, NY.

Jaglinski, T. and Lakes, R. S., 2004, "Anelastic instability in composites with negative stiffness inclusions", Philosophical Magazine Letters, 84, (12) 803 - 810, Dec. (2004).

Jaglinski, T., Kochmann, D., Stone, D. and Lakes, R.S., 2007, "Composite Materials with Viscoelastic Stiffness Greater Than Diamond," Science, Vol. 315, pp. 620-622.

Jensen, B. D., Parkinson, M. B., Kurabayashi, K., Howell, L. L. and Baker, M. S., 2001, "Design optimization of a fully-compliant bistable micro-mechanism," in Proceedings of the ASME International Mechanical Engineering Congress and Exposition, IMECE2001/MEMS-23852, New York.

Jensen, B.D. and Howell, L.L., 2003, "Identification of Compliant Pseudo-Rigid-Body Four-Link Mechanism Configurations Resulting in Bistable Behavior," Journal of Mechanical Design, Vol. 125, pp. 701-708.

Jensen, B.D., Howell, L.L. and Salmon, L.G., 1999, "Design of Two-Link, In-Plane, Bistable Compliant Micro-Mechanisms," ASME Journal of Mechanical Design, Vol. 121, pp. 416-423.

Joo, J.Y. and Kota, S., 2004, "Topological synthesis of compliant mechanisms using nonlinear beam elements," Mechanics Based Design of Structures and Machines, Vol. 32 (1), pp. 17-38.

King, C. and Campbell, M.I., 2004, "On the Design Synthesis of Multistable Equilibrium Systems," in Proceedings of the International Design Engineering and Technical Conference, Salt Lake City, Utah.

Lakes, R. S. and Drugan, W. J., 2002, "Dramatically stiffer elastic composite materials due to a negative stiffness phase?", J. Mechanics and Physics of Solids, 50, 979-1009.

Lakes, R. S., Lee, T., Bersie, A., and Wang, Y. C., 2001, "Extreme damping in composite materials with negative stiffness inclusions", Nature, 410, 565-567, 29 March (2001).

Li, J. and Weng, G.J., 1997, "A homogenization theory for the overall creep of isotropic viscoplastic composites," Acta Mechanica, Vol. 125, pp. 141-153.

Marinov, P., 1978, "Two-phase mixture - viscoelasticity and general equivalent mechanical model," Polymer Engineering and Science, Vol. 18 (4) , pp. 335 – 338.

Masters, N.D. and Howell, L.L., 2003, "A Self-Retracting Fully-Compliant Bistable Micromechanism," Journal of Microelectromechanical Systems, Transactions of IEEE/ASME, Vol. 12, pp. 273-280.

Milton, G.W. and Berryman, J.G., 1997, "On the effective viscoelastic moduli of two-phase media. II. Rigorous bounds on the complex shear modulus in three dimensions," Proc. R. Soc. London A, Vol. 453, pp. 1849–1880.

Neves, M.M., Rodrigues, H. and Guedes, J.M., 1995, "Generalized topology design of structures with a buckling load criterion,", Structural and Multidisciplinary Optimization, Vol. 10(2), pp. 71-78.

Prasad, J., and Diaz, A.R., 2005, "Layout of Tileable Multistable Structures Using Topology Optimization," in Proceedings of TopoptSYMP2005, IUTAM symposium, Rungstedgaard, Copenhagen, Denmark, October 26 – 29, 2005.

Qiu, J., Lang, J. and Slocum, A.H., 2004, "A Curved-Beam Bistable Mechanism," Journal of Microelectromechanical Systems, Vol. 13 (2), pp. 137-146.

Sigmund O., 1994, "Materials with prescribed constitutive parameters: an inverse homogenization problem," International Journal of Solids and Structures, Vol. 31(17), pp. 2313–2339.

Sigmund, O., 1995, "Tailoring materials with prescribed elastic properties," Mechanics of Materials, Vol. 20, pp.351-368.

Sigmund, O., 1997, "On the Design of Compliant Mechanisms Using Topology Optimization", Mechanics of Structures and Machines, Vol. 25, pp. 493-524.

Sigmund, O., 2000, "A new class of extremal composites. Journal of Mechanics and Physics of Solids," Vol. 48, pp.397–428.

Sigmund, O., 2001, "A 99 line topology optimization code written in MATLAB," Structural and Multidisciplinary Optimization, Vol. 21(2), pp. 120-127.

Sigmund, O., 2007, "Morphology-based black and white filters for topology optimization," Structural and Multidisciplinary Optimization, Vol. 33, pp. 401-424.

Svanberg, K., 1987, "The method of moving asymptotes," International Journal for Numerical Methods in Engineering, Vol. 24, pp. 359 –373.

Tcherniak, D. and Thomsen, J.J., 1998, "Slow Effects of Fast Harmonic Excitation for Elastic Structures," Nonlinear Dynamics 17: 227–246.

Wang, Y. C. and Lakes, R. S., 2004a, "Extreme stiffness systems due to negative stiffness elements", American J. of Physics, 72, Jan. (2004).

Wang, Y. C. and Lakes, R. S., 2004b, "Negative stiffness induced extreme viscoelastic mechanical properties: stability and dynamics", Philosophical Magazine, 35, 3785-3801, Dec. (2004).

Wang, Y. C. and Lakes, R. S., 2005a, "Stability of negative stiffness viscoelastic systems", Quarterly of Applied Math., Vol.63, pp.34-55, March (2005).

Wang, Y.C. and Lakes, R. S., 2005b, "Composites with inclusions of negative bulk modulus: extreme damping and negative Poisson's ratio," Journal of Composite Materials, Vol. 39 (18), pp. 1645- 1657.

Yi, Y.-M., Park, S.-H. and Youn, S.-K., 1998, "Asymptotic homogenization of viscoelastic composites with periodic microstructures," International Journal of Solids and Structures, Vol. 35 (17), pp. 2039-2055.

Yi, Y.-M., Park, S.-H. and Youn, S.-K., 2000, "Design of microstructures of viscoelastic composites for optimal damping characteristics," International Journal of Solids and Structures, Vol. 37, pp. 4791-4810.

Yu, Y., Naganathan, N.G. and Dukkipati, R.V., 2000, "Review of automotive vehicle engine mounting systems," International Journal of Vehicle Design, Vol. 24 (4), pp. 299-319.